NTNU

Norwegian University of
Science and Technology

The capacity of creeping shale to form an annular barrier

Are Olav Eriksen Brendsdal

Petroleum Geoscience and Engineering
Submission date: August 2017
Supervisor: Andreas Bauer, IGP
Co-supervisor: Kun Su, Total SA

Norwegian University of Science and Technology
Department of Geoscience and Petroleum

Norwegian University of Science and Technology

Master Thesis

The Capacity of Creeping Shale to form an Annular Barrier

Are Olav Eriksen Brendsdal

Abstract

This report was written in Pau, France, as part of an internship in Total E&P Drilling & Wells Division, Geomechanics Entity, under supervision of Kun Su. Shale displacing inwards in the wellbore is a well-recognized phenomenon, but not so well understood. For certain shales under certain conditions the degree of deformation can be enough to impinge the casing, and eventually completely close the annular gap between the formation and casing wall. For such cases shale can potentially replace cement as external barrier if it is correctly verified through logs and pressure testing. This can form a cost-efficient and convenient solution in for example P&A operations. Calculations show that shale has to undergo plastic deformation in order to displace sufficiently, and in most cases time dependent plastic (viscoplastic) deformation is required (often called creep). Plasticity and creep in shales and other clay rich rocks is a fluid driven interparticle process depending on several rock parameters and borehole conditions. This thesis investigates some of the geomechanical aspects of the displacement process, and through a literature review and field cases, discusses how the creeping capacity of shales is linked to different characteristic and conditions. Experiments show that creep is more profound in weak unconsolidated formations, porosity is usually an excellent indicator for degree of compaction. Typically, high amounts of clay minerals (in particular smectite) and small amounts of typical cementing materials like quartz and carbonate appears to enhance creep. It is found that creep generally increases at higher temperature and higher deviatoric stress, and that rocks like shale display a significant amount of anisotropic creep behavior related to bedding planes and load direction. Typical creeping formations can have low in-situ deviatoric stresses as they have deformed and stabilized for millions of years, these low deviatoric stresses could potentially indicate a formations threshold for creep. Some petrophysical log measurements can to some degree be linked to the creeping capacity of a formation. High porosity, low sonic velocities and density readings are potential indications to look for, if combined with high pore pressure it could potentially lead to a creeping formation. Two different shale formations in the North Sea in wells drilled by Total E&P has been analyzed. The shale in the Hordaland group shows high creeping capacity and potential use as barrier, this matches well with trends observed from literature and available industry experience. For a deeper shale, numerical simulations, a creep test, mineralogy and analytical solutions and more show that despite some traditionally good conditions for creep (high temperature and pore pressure) this shale is not likely to creep sufficiently to form a barrier.

Sammendrag

Denne rapporten ble skrevet i Pau, Frankrike, som en del av et internship i Total E&P, Avdeling: Boring & Brønn, Enhet: Geomekanikk, under veiledning av Kun Su. Skifer som gradvis deformerer seg innover i brønnhullet er et kjent men ikke fullt ut forstått fenomen. I noen tilfeller, med riktige brønnforhold og skifersegenskaper så kan deformasjonen være tilstrekkelig til at skiferen kommer i kontakt med foringsrøret, og etterhvert fullstendig lukker ringrommet. I slike tilfeller kan skiferen potensielt erstatte sement som en ekstern barriere, gitt at den blir testet på en adekvat måte ved hjelp av logger og trykktesting. Dette kan utgjøre en beleilig og kostnadseffektiv løsning i for eksempel P&A operasjoner. Beregninger viser at skifer må gjennomgå plastisk deformasjon for å deformeres tilstrekkelig, og i de fleste tilfeller er viskoplastisk deformasjon nødvendig (ofte kalt kryp). Plastisitet og kryp i skifer og andre leirrike steiner er en væskedrevet interpartikulær prosess som avhenger av mange steinparametere og borehullsforhold. Denne oppgaven undersøker noen av de geomekaniske aspektene i deformasjonsprosessen. Ved hjelp av en litteraturstudie og analyse av tilgjengelige industrierfaringer, blir det diskutert hvordan krypkapasiteten til skifer avhenger av forskjellige materialegenskaper og borehullsforhold. Flere forsøk viser at kryp er mer utbredt i svake ukompakterte formasjoner, porøsitet er vanligvis en utmerket indikasjon på grad av kompaksjon. Typisk, gir høyt innhold av leirmineraler (spesielt smektitt) og lavt innhold av typiske sementeringsmineraler som kvarts og karbonat, gode krypegenskaper. Kryp øker generelt ved høyere temperatur og deviatorisk stress. Skifer viser en betydelig mengde anisotropisk krypdeformasjon relatert til retningen på lagdeling i forhold til trykkfordeling. Typiske formasjoner som kryper har små formasjonstrykkforskjeller ettersom de har deformert seg i millioner av år til de er i en stabil tilstand, disse trykkforskjellene kan potensielt representere terskelen for at kryp skal reaktiveres. Noen petrofysiske logmålinger kan til en viss grad bli linket til krypkapasiteten til en formasjon. Høy porøsitet, lave soniske hastigheter og tetthetsmålinger er ting å se etter, kombinert med høyt poretrykk kan dette indikere formasjoner som vil krype. To forskjellige formasjoner i Nordsjøen fra brønner boret av Total E&P har blitt analysert. Skiferen i Hordalandsgruppen viser høy krypkapasitet og bra potensial som barriere, dette samsvarer med trender observert fra litteratur og tilgjengelig industrierfaring. For en dypere skifer viser numeriske og analytiske beregninger, komposisjon og en kryptest, at til tross for borehullsforhold som normalt sett er gunstige (høy temperatur og høyt poretrykk) vil sannsynligvis ikke denne formasjonen krype tilstrekkelig til å danne en barriere.

Acknowledgement

This report marks the end of a five-year long master degree in petroleum engineering at the Norwegian University of Science and Technology (NTNU) in Trondheim. The final report was written in Pau, France, in combination with an internship in Total E&P Drilling & Wells Division, Geomechanics Entity, under supervision of Kun Su.

First of all I would like to express my gratitude towards my two supervisors Kun Su and Andreas Bauer for their guidance and support throughout the thesis. I would also like to thank Duc Thai for his help on the numerical modelling in Elfen. Furthermore, I appreciate and want to say thank you to Mats Skaug, Sy Tuan Nguyen and the Geomechanics team in Total E&P Pau, for openly sharing their knowledge.

Special thanks go to Total E&P which has provided me with the topic, relevant data, supervision and an office.

Table of Contents

Abstract iii

Sammendrag iv

Acknowledgement v

Table of Contents vi

List of Figures x

List of Tables xvii

1. Introduction 1

1.1 Background 1

1.2 Approach 2

Introduction to P&A 3

1.3 NORSOK D-010 3

1.3.1 Material Requirements 3

1.3.2 Number of Barriers 3

1.3.3 NORSOK's Acceptance Criteria for Creeping Formations 5

Introduction to the Geomechanical Problem 6

1.4 Plastic Deformation 7

Introduction to Plasticity Modelling 9

1.4.1 The Transition from Elastic to Plastic Strain 9

1.4.2 Flow Rules – How the Strain and Stress Distribution Develops 11

1.4.3 Deformation Effects on Rock Parameters 14

An Elastoplastic Hollow Cylinder Model with Pore Pressure Profile 15

1.5 Derivation of Stress Distribution 15

1.5.1 Stress Distribution 17

1.5.2 Radius of the Plastic Zone 19

1.5.3 Strain in the Elastic Zone 20

1.5.4 Strain in the Plastic Zone 21

1.6 Discussion of Derived Solution 23

1.6.1 Comparison with (Chen, et al., 1999) and (Zhang, et al., 2012) 23

1.6.2 Deviations from (Chen, et al., 1999) and (Zhang, et al., 2012) 26

1.6.3 Pore Pressure Evaluation 30
1.6.4 Residual Strength and Flow Rule (Angle of Dilatancy) 35
1.6.5 Stress Distribution 36
1.6.6 Plastic vs Elastic Deformation Contribution 37
1.6.7 Important Sources of Error 38
1.7 Concluding Comments 39
Literature Review on Creep Tests for Shale and Clay 41
1.8 What is Creep 41
1.9 Creep Tests 42
1.10 Callovo-Oxfordian Argillite and Opalinus Clay from Mont Terri 42
1.10.1 Experimental Study of the Hydro-Mechanical Behavior of the Callovo-Oxfordian Argillite (Zhang & Rothfuchs, 2004) 43
1.10.2 Experimental Study of the Thermo-Hydro-Mechanical Behavior of Indurated Clays (Zhang, et al., 2007) 46
1.10.3 Anisotropy Effects on Dilatancy, Strength and Creep 53
1.11 Boom Clay Experiments 53
1.11.1 Time-dependent behavior of rocks: Laboratory tests on hollow cylinder (Rousset, et al., 1989) 54
1.11.2 Medium resolution X-Ray computed tomography of hollow cylindrical samples of Boom Clay (You, et al., 2010) 56
1.11.3 Time-dependent behavior of deep clays (Giruad & Rousset, 1996) 57
1.11.4 Creep behavior of boom clay (Yu, et al., 2015) 59
1.12 Brief summary of preliminary results from SINTEF Research project: “Shale as a Permanent Barrier after Well Abandonment” (SINTEF Petroleum Research, 2016) 62
1.13 Discussion: Some General Creep Correlations 66
Industry Experience and Field Cases 68
1.14 Total Field Case, Can Creep be Linked with LWD? 68
1.14.1 Field Case Details 68
1.14.2 Case 1: Well A 69
1.14.3 Case 2: Well B 75
1.15 Experience from P&A at Brent (Shell) 81
1.16 Discussion: Field Experiences and LWD Trends 84

P&A Assessment for Well C.2 87
1.17 General Case Details 87
1.18 Corner Knoll and Draupne Assessment 89
1.19 Heather Shale Composition 89
1.19.1 Comparable Materials 92
1.20 Discussion of Heather Shale Creep Test 92
1.21 Discussion on Heather Shale's Creeping Ability 97
1.22 Mathematical Predictions 98
1.22.1 Conventional Creep Modelling 98
1.22.2 Kun Su's Norton Power Law Model 99
1.22.3 Barker's and Liu's Solutions for Wellbore Closure 101
1.23 Elastoplastic Model Results 103
1.24 Numerical Modeling of Annular Space Closuring 106
1.25 Calibration 107
1.26 Results 108
1.27 Discussion of results 112
1.28 Reservoir production effects 114
1.29 Conclusion on Heather P&A job 115
Conclusion 116
Nomenclature 117
Bibliography 118
Appendix A: Clay structure and swelling i
Clay i
Swelling Clay ii
Crystalline Swelling iii
Osmotic Swelling v
Osmotic Pressure v
Smectite vi

List of Figures

Figure 2.1: Illustration of two reservoirs within the same pressure regime (Norwegian Petroleum Safety Authority, 2013) 4
Figure 2.2: A well barrier element has to be sealed both vertically and horizontally (Norwegian Petroleum Safety Authority, 2013) 5
Figure 2.3: Acceptance Criteria for use of creeping formations in P&A (Norwegian Petroleum Safety Authority, 2013) 6
Figure 3.1: (a) Simplified figure showing the horizontal forces in play. $\boldsymbol{pw}$ is the well pressure and is created by the weight of the drilling fluid and $\boldsymbol{\sigma h}$ is the external pressure created by the formation. (b) Borehole geometry for the example 8
Figure 4.1: Stress strain curve showing elastic-brittle-plastic and elastic-perfectly-plastic behavior 11
Figure 4.2: Mohr-Coulomb criterion and the direction of its gradient plotted in stress space 13
Figure 4.3: Stress vs strain (deformation) in a uniaxial compression test (Fjaer, et al., 2008) 14
Figure 5.1: Section of the hollow cylinder model (Fjaer, et al., 2008) 16
Figure 5.2: Cross sectional view of the hollow cylinder model 17
Figure 5.3: Borehole deformation vs borehole pressure (Zhang, et al., 2012), the colored dotted lines represent two cases of the solution derived. 25
Figure 5.4: Left figure: Dimensionless radial displacement $\boldsymbol{uRw, in}$ % vs. dimensionless radius $\boldsymbol{rRw}$, for the two different ways of modelling axial stress, see right figure (all other values are identical). In the graph to the left red and blue represents the plastic zone while green and cyan represents the elastic zone. 27
Figure 5.5: Left figure: Dimensionless radial displacement $\boldsymbol{uRw, in}$ % vs. dimensionless radius $\boldsymbol{rRw}$, for the two different ways of modelling axial stress, see right figure (all other values are identical). In the graph to the left red and blue represents the plastic zone while green and cyan represents the elastic zone. 28
Figure 5.6: Dimensionless radial displacement $\boldsymbol{uRw, in}$ % vs. dimensionless radius $\boldsymbol{rRw}$, showing the effect of implementing the RDM model. Right graph shows the entire radius of the sample, left graph shows only plastic zone. These results are for axial stress modelled as in (Chen, et al., 1999) and (Zhang, et al., 2012). 29
Figure 5.7: Dimensionless radial displacement $\boldsymbol{uRw, in}$ % vs. dimensionless radius $\boldsymbol{rRw}$, showing the effect of implementing the RDM model. Right graph shows the entire radius of the

sample, left graph shows only plastic zone. These results are for axial stress as originally modelled in the derived solution. 29
Figure 5.8: Dimensionless change in pore pressure as a function of dimensionless radius and dimensionless time (the numbers above the black curves) (Detournay & Cheng, 1988), compared to equation 5.7 with different radius of disturbance as shown in the legend to the right. 31
Figure 5.9: Left: Pore pressure profiles in MPa vs. ($\boldsymbol{rRw}$). Right: corresponding dimensionless radial displacement $\boldsymbol{uRw, in}$ % vs. dimensionless radius $\boldsymbol{rRw}$. Blue curve on left graph corresponds to blue (and cyan) curve on right graph and so forth. The different colors in the right figure shows the plastic (red, blue, black) and elastic (green, cyan, grey) zones. 32
Figure 5.10: Left: Pore pressure profiles in MPa vs. ($\boldsymbol{rRw}$). Right: corresponding dimensionless radial displacement $\boldsymbol{uRw, in}$ % vs. dimensionless radius $\boldsymbol{rRw}$. Blue curve on left graph corresponds to blue (and cyan) curve on right graph and so forth. The different colors in the right figure shows the plastic (red, blue, black) and elastic (green, cyan, grey) zones. 33
Figure 5.11: Left: Pore pressure profiles in (MPa vs. ($\boldsymbol{rRw}$)). Right: corresponding dimensionless radial displacement $\boldsymbol{uRw, in}$ % vs. dimensionless radius $\boldsymbol{rRw}$. Blue curve on left graph corresponds to blue (and cyan) curve on right graph and so forth. The different colors in the right figure shows the plastic (red, blue, black) and elastic (green, cyan, grey) zones. .34
Figure 5.12: Dimensionless radial displacement $\boldsymbol{uRw, in}$ % vs. dimensionless radius $\boldsymbol{rRw}$ for residual cohesion of 100% (red and green) , 75% (blue and cyan) and 50% (black and grey) of the elastic cohesion 35
Figure 5.13: Dimensionless radial displacement $\boldsymbol{uRw, in}$ % vs. dimensionless radius $\boldsymbol{rRw}$ for dilatancy angles of 0° (red), 50% of $\boldsymbol{\phi}$ (blue) and 100% of $\boldsymbol{\phi}$ (black, associated flow rule)...36
Figure 5.14: The effect of a plastic cohesion on stresses. Left graph $\boldsymbol{cp = c}$, right graph $\boldsymbol{cp = 0.5c}$, rest of the inputs are given in Table 5.1 37
Figure 5.15: Dimensionless radial displacement $\boldsymbol{uRw, in}$ % vs. dimensionless radius$\boldsymbol{rRw}$. Left graph $\boldsymbol{cp = c}$, right graph $\boldsymbol{cp = 0.5c}$, rest of the inputs are given in Table 5.1 38
Figure 6.1: The three different creep stages illustrated on a strain vs time plot (Hosford, 2005) 42
Figure 6.2: Typical result from multistage triaxial compression test, where $\boldsymbol{\sigma 1 - Y}$ is yield stress, $\boldsymbol{\sigma 1 - D}$ onset of dilatancy, $\boldsymbol{\sigma 1 - F}$ peak failure and $\boldsymbol{\sigma 1 - R}$ residual strength. (Zhang & Rothfuchs, 2004) 44
Figure 6.3: Strain rates for samples taken from different depths (Zhang & Rothfuchs, 2004) 45

Figure 6.4: Scaling effects for elastic and creep deformation/strain (Zhang & Rothfuchs, 2004) 45
Figure 6.5: Graph showing the quasi-steady creep rate vs the stress applied (Zhang & Rothfuchs, 2004).....46
Figure 6.6: Petrophysical properties of the investigated rocks (Zhang, et al., 2007) 47
Figure 6.7: Axially fixed, laterally unconstrained Collovo-Oxfordian Argillite sample exposed to changes in air humidity and observed stress responses (swelling pressure) (Zhang, et al., 2007). 48
Figure 6.8: Constant axially loaded, laterally unconstrained Opalinus Clay sample exposed to changes in air humidity and observed strain responses (swelling and shrinking) (Zhang, et al., 2007). 48
Figure 6.9: Triaxial compaction test with varying saturation, showing pore water effects on strain/deformation on an Opalinus Clay sample (Zhang, et al., 2007). 49
Figure 6.10: Thermal expansion test results (a) temperature steps and water release vs time (b) total strain vs time (c) strain rates vs time (Zhang, et al., 2007).....50
Figure 6.11: Temperature effects on creep for Callove-Oxfordian Argillite samples for different loads (Zhang, et al., 2007). 51
Figure 6.12: Triaxial strength tests with different temperatures (Zhang, et al., 2007). 52
Figure 6.13: The reduction of gas permeability as a function of time. This effect demonstrates the self-healing abilities of the Callovo-Oxfordian argillaceous samples (Zhang, et al., 2007). 53
Figure 6.14: Deformation behavior of samples loaded parallel (P) or normal 54
Figure 6.15: Sample dimensions and definitions of different parameters (Rousset, et al., 1989) 55
Figure 6.16: The graphs show the internal volumetric strain vs internal pressure and on the left graph time is also included. (Rousset, et al., 1989). 56
Figure 6.17: CT-slices of the Boom Clay sample before and after the mechanical unloading. It is clearly visible that the radial strain parallel to the bedding planes is significantly larger in the vicinity of the internal hole (You, et al., 2010).....57
Figure 6.18: Displacement vs radius for different angles to the bedding planes (You, et al., 2010) 57
Figure 6.19:Results from the triaxial creep test showing strain as a function of time for the three stages (Giruad & Rousset, 1996) 58

Figure 6.20: Test procedures for the creep phase, note that compressive stresses are defined as positive (Yu, et al., 2015).....59
Figure 6.21: Comparison of strain with respects to time and deviatoric stress level. (a) Sample TCP1 (b) Sample TCP1 vs. Sample TCP3 (Yu, et al., 2015). 60
Figure 6.22: The failed samples. TCP1 left and TCP3 right (Yu, et al., 2015). 61
Figure 6.23: Measurements of in situ wellbore diameter reduction with different diameter rings (Yu, et al., 2015). 62
Figure 6.24: test materials at ongoing research at SINTEF (taken from steering committee presentation 7, Trondheim 24.11.2016 (SINTEF Petroleum Research, 2016)).....63
Figure 6.25: The effect of rapid decrease in "borehole" pressure on the Field Material 388 (SINTEF Petroleum Research, 2016). 64
Figure 6.26: Top surface of sample where after test. Borehole was closed (before debris was removed) and the plastic region was extended to the sample boundary (taken from SINTEF REF 2015_8_27 ML388 (SINTEF Petroleum Research, 2016)).....64
Figure 6.27: Post-test μCT scan of the the Field material 388 showing that the annulus is sealed, but with a region around the casing with higher porosity. Green areas represent holes/defects, while blue represents casing (SINTEF Petroleum Research, 2016). 65
Figure 6.28: post μCT scan image of Pierre shale showing a significant volume of high porosity around the casing. Green areas represent holes/defects, while blue represents casing. (SINTEF Petroleum Research, 2016) 65
Figure 7.1: Wellbore geometry and fluid parameters 69
Figure 7.2: Comparison of the acoustic impedance and CBL amplitude for different times. The change in the acoustic signatures clearly show the difference in solid content outside the casing for different times. Graph made from (Skaug, 2016). 72
Figure 7.3: Graphs showing the difference in average acoustic impedance and CBL amplitude for the different logs. For comparison reasons measured depth, true vertical depth, inclination, lithology and bond quality are also included. The threshold for good bonding is set according to (Williams, et al., 2009) and the graph made from Totals JIP presentation (Skaug, 2016)...73
Figure 7.4: LWD data and CBL+IS measurements plotted with TVD correlation for case 1..74
Figure 7.5: Mineralogy vs TVD with key sections extrapolated to the CBL+IS and bond quality measurements for case 1. Graph made from (Skaug, 2016). 75
Figure 7.6: Comparison of the acoustic impedance and CBL amplitude for different times. The change in the acoustic signatures clearly show the difference in solid content outside the casing for different times. Graph made from (Skaug, 2016).. 78

Figure 7.7: Mineralogy vs TVD with key sections extrapolated to the CBL+IS and bond quality measurements for case 2. Graph made from (Skaug, 2016). 79
Figure 7.8: LWD data and CBL+IS measurements plotted with TVD correlation for case 2..80
Figure 7.9: P&A statistics for the Brent field as of August 2015 (Hogg & Davison, 2015) 81
Figure 7.10: The different stratigraphic/geological layers in the overburden of the Brent field (Hogg & Davison, 2015).....82
Figure 7.11: Density, Sonic and GR measurements for a selected convenient interval in the Brent overburden (Hogg & Davison, 2015) 83
Figure 7.12: Illustration of the slow formation and smectite correlation (Hogg & Davison, 2015) 84
Figure 8.1:General details about the well completion 87
Figure 8.2:Stress regime for different times taking into account the effects from reservoir production 88
Figure 8.3: Borehole, screen geometry and drilling fluid details (based on lithology log") 88
Figure 8.4: Shale formation in the interval between 9 7/8" casing shoe and top of reservoir (based upon lithology log) 89
Figure 8.5: Composition of clay fraction in Heather 90
Figure 8.6: Composition based on average values from cuttings for the relevant depth.....91
Figure 8.7: Statoil on mineralogy (Carlsen, 2017) 91
Figure 8.8: Comparisons of creep rates for the some investigated shales. Creep rate on Hordaland shale is based on conservative estimates from the closing of the annular gap in well A. Creep rate in Heather is based on the creep test discussed in section 8.4.....92
Figure 8.9: Load steps and procedure in creep test.....93
Figure 8.10: Evolution of axial and lateral strains with time during the phase of deviatoric creep 93
Figure 8.11: Load steps for the creep test 94
Figure 8.12: Rate of deformation shown for different times 95
Figure 8.13: Core sample before (left) and after (right) the test. The sample is cracked before being tested. 96
Figure 8.14: Axial and lateral strains versus deviatoric stress during the creep phase and final triaxial compression phase 96
Figure 8.15: Creep rate of different shales under a deviatoric stress of 2-5 MPa, as given by (Su, 2013), the Heather and Hordaland shales are included for comparison reasons. Note that the

creep rate of the Hordaland shale is a conservative estimation based on the time it took before good bonding was observed in Well A. 100
Figure 8.16: Creep rates for different materials under different deviatoric loadings. The power-law model for creep is also included for different degrees of porosity (10-20%). Keep the temperature difference for the different creep rates in mind. 101
Figure 8.17: Barker's and Liu's solution for the inputs given to the right. The radius input displayed in the table to the right is actually the diameter, but this does not affect the result which is given in $\boldsymbol{RRw0}$. 102
Figure 8.18 Barker's and Liu's solution for the inputs given to the right. The radius input displayed in the table to the right is actually the diameter, but this does not affect the result which is given in $\boldsymbol{RRw0}$. 103
Figure 8.19: Displacement ($\boldsymbol{\Delta RwRw}$ in %) and stresses (MPa) for case 1 104
Figure 8.20: Displacement ($\boldsymbol{\Delta RwRw}$ in %) and stresses (MPa) for case 2 105
Figure 8.21: Displacement ($\boldsymbol{\Delta RwRw}$ in %) and stresses (MPa) for case 3 105
Figure 8.22: Displacement ($\boldsymbol{\Delta RwRw}$ in %) and stresses (MPa) for case 4 106
Figure 8.23: Quasi-steady creep rates vs deviatoric stresses for Heather shale sample and equation 8.11 for different temperatures (with parameters given in Table 8.2) 108
Figure 8.24: Von Mises effective stress (Pa) (as given by equation 8.13) after 110 days. The direction of the minimum ($\boldsymbol{\sigma h}$) and maximum ($\boldsymbol{\sigma H}$) horizontal formation stresses are also included. 109
Figure 8.25: deformation in meters as a function of time (1 time unit equals 10 days). 110
Figure 8.26: Total shear strain rate (contribution of elastic and plastic fraction) as a function of time (m/m*10day) 111
Figure 8.27: Von Mises Effective stress in Pascal (as given by equation 8.13) versus time ..111
Figure 8.28: Shear stress (Pa) as a function of time 112
Figure 8.29: Stress changes as a result of reservoir production 114
Figure 0.1: "Infinite" numbers of tetrahedra are linked together in a hexagonal base network, and forms a tetrahedral layer (Chen, 2016) i
Figure 0.2: The octahedra are combined so that the corner of each octahedron in an octahedral layer is shared by three octahedra (Chen, 2016) i
Figure 0.3: Unit layer composition of Kaolinite (1:1 clay) and Bentonite (2:1 clay) (Chen, 2016) ii

Figure 0.4: The effect of increasing pore pressure displayed in a shear stress ($\boldsymbol{\tau}$) vs principal stress ($\boldsymbol{\sigma'}$). The line above the circles is the failure envelope (Fjaer, et al., 2008) iii
Figure 0.5: Expanding lattice of a smectite clay (montmorillonite) (Chen, 2016) iv
Figure 0.6: Expanding lattice with Sodium ($\boldsymbol{Na+}$) as cation (Strand, 2001) iv
Figure 0.7: Expanding lattice with Calcium ($\boldsymbol{Ca2+}$) as cation (Strand, 2001) v
Figure 0.8: Illustration of osmotic pressure, where a shows the initial condition and b shows when equilibrium is reached (Fakcharoenphol, et al., 2014) vi

List of Tables

Table 5.1: Inputs 24
Table 8.1: Input values.....103
Table 8.2: Material properties used in the simulation.....107

1. Introduction

1.1 Background

At the end of 2016 there were 80 fields in production on the Norwegian continental shelf (NCS), many of which are ageing and production on decline (Norwegianpetroleum.no, 2017). The consequence is an incoming wave of wells that have to be permanently plugged and abandoned (PP&A), either for enhanced production purposes (re-use of primary wellbore in order to drill to new geological targets) or field shutdown.

The recent drop in oil price struck hard for the petroleum industry in Norway and in these challenging times where it has become harder to make money it is more important than ever to save money. Traditional plug and abandonment (P&A) operations requires rig time and are therefore very costly, which creates a big motivation for the industry to improve these methods. In recognition of the imminent plug and abandonment issue the Norwegian Oil Industry Association formed the Plug and Abandonment Forum (PAF) in 2009, in order to "develop robust and cost reducing solutions for the upcoming P&A issue on the NCS" (Straume, 2013). PAF later demonstrated how it would take 15 rigs working only on P&A 40 years to complete the task using traditional methods (Straume, 2014).

Total E&P is the second biggest oil company on the NCS with interests in nearly 100 production licenses (Total, 2016) and the potential cost reduction related to improving P&A operations is large. Traditional bond logs performed in the North Sea has shown good annular seal far above the theoretical cement top. Clear correlations between these sections and shales known to displace radially inwards in the wellbore has shown that shales and other clay rich rocks sometimes re-establish the natural barrier outside the casing. These shale sections, if adequately tested, could qualify as external barriers and replace costly and failure prone P&A operations. Shale constitutes over 75% of formations drilled through and is behind more than 90% of all wellbore stability problems (Talabane, et al., 1993). Understanding the displacement mechanisms of shale formations will therefore not only reduce wellbore stability problems, but one may also discover how to potentially benefit from these traditionally unwanted effects.

1.2 Approach

The main goal of this thesis/internship is investigating the capacity shales have for forming such barriers around the casing. In addition, an assessment will be formed on whether a shale formation above the Martin Linge field can be a suitable candidate for forming an annular barrier in an upcoming P&A job. In order to perform this investigation and assessment, the following tasks will be carried out:

- Research regulations and guidelines on the NCS for using a shale as barrier in P&A
- Researching some of the key geomechanical aspects for the borehole closure problem
- Discuss and analyze an analytical approach for modelling borehole closure, research the applicability for the relevant borehole conditions and hollow cylinder lab tests
- Perform a literature review on creep tests for different types of shales in order to establish the correlation between material properties and creep
- Study available industry experience and identify reoccurring patterns
- Analyze cement bond log data in different wells, find intervals where the annular gap has closed significantly due to creeping shale and link the well closure to the different well data
- Interpret a creep test on the relevant formation, identify creeping capacity and material parameters for models predicting the wellbore closure
- Perform some analytical and numerical predictions for the borehole closure in the P&A case

Introduction to P&A

There comes a time for every well when it goes from being an asset to a liability and consequently will be plugged and abandoned. The P&A operation shall leave as little traces as possible and minimize the chance of leakage by taking into account all contingencies in the foreseeable future. In practice, the chance of leakage shall be just as low, or lower than it was before the geological area was altered by human activity. This section gives a brief description of relevant some P&A regulations and guidelines on the NCS.

1.3 NORSOK D-010

The NORSOK D-010 is a standard that defines guidelines and requirements related to well integrity in drilling and well activities (one of these being P&A) on the NCS. It is developed by the Norwegian Petroleum Safety Authority in collaboration with "broad participation of interested parties in the Norwegian petroleum industry" (Norwegian Petroleum Safety Authority, 2013).

1.3.1 Material Requirements

A well barrier is an envelope consisting of one or several well barrier elements (WBE), preventing formation fluids from unintentionally migrating from one formation to another, or to the surface. NORSOK D-010 was revised from 2004 to 2011 adding the possibility of using other materials than cement as WBE's. The requirements a well barrier material must fulfill are a bit vague, perhaps in order to encourage innovative solutions - such as shale. According to NORSOK every well barrier shall have the following characteristics (Norwegian Petroleum Safety Authority, 2013):

- provide long term integrity (eternal perspective)
- impermeable
- non-shrinking
- able to withstand mechanical loads/impact
- resistant to chemicals/substances (H2S, CO2 and hydrocarbons)
- ensure bonding to steel
- not harmful to steel tubulars integrity

1.3.2 Number of Barriers

PP&A operations can vary a bit depending on what conditions are encountered when drilling the well. If no permeable formation with overpressure, or hydrocarbon reservoir are encountered, one well barrier will be sufficient. However, once an over-pressured permeable

formation or a hydrocarbon reservoir is encountered, a minimum of two well barriers are required (Statoil, 2016). In practice, the double barrier requirement means that if the primary well barrier (barrier closest to source of inflow) fails, the secondary barrier shall be able to withstand all the resulting loads. Furthermore, a cross flow well barrier may also be necessary to prevent unacceptable flow between formations, for example two hydrocarbon reservoirs in different pressure regimes. It is worth noting that multiple reservoirs within the same pressure regime can be considered as one reservoir, see Figure 0.1. A well barrier can also be shared, meaning that a cross flow well barrier also will act as the primary well barrier for the deepest reservoir.

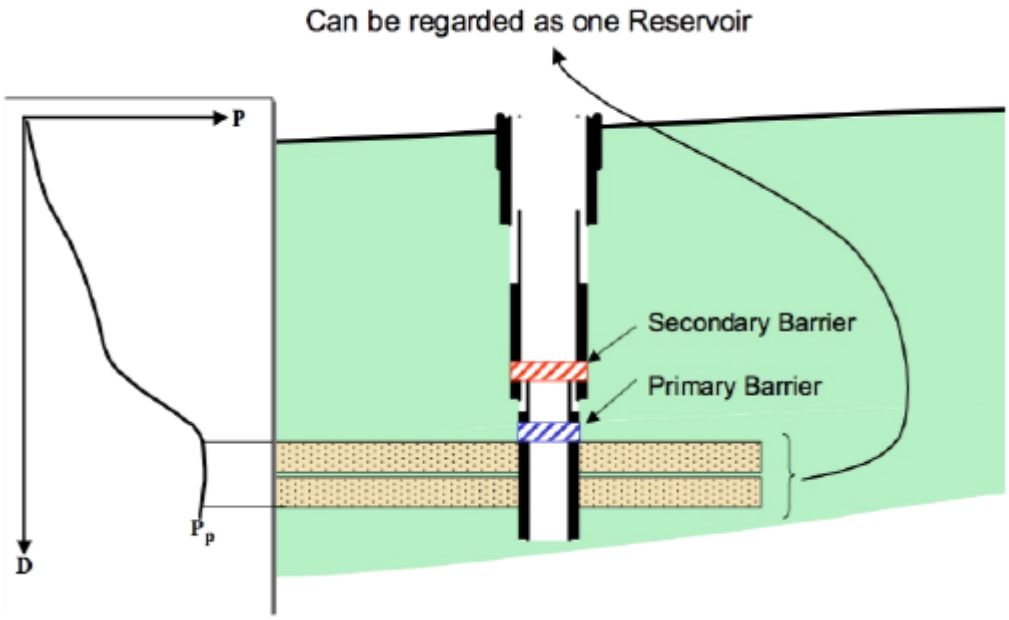

Figure 0.1: Illustration of two reservoirs within the same pressure regime (Norwegian Petroleum Safety Authority, 2013)

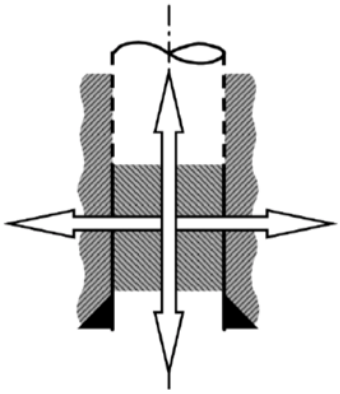

Figure 0.2: A well barrier element has to be sealed both vertically and horizontally (Norwegian Petroleum Safety Authority, 2013)

1.3.3 NORSOK's Acceptance Criteria for Creeping Formations

Every well barrier must cover the entire cross-sectional area of the wellbore and seal both vertically and horizontally, see Figure 0.2. In addition, the well barrier must be placed at a depth where the adjacent formation is impermeable and the formation integrity exceeds the maximum pressure that can be generated from below. The acceptance criteria from NORSOK D-010 for the use of creeping formations in P&A is summarized below in Figure 0.3:

Features	Acceptance criteria
A. Description	The element consists of creeping formation (formation that plastically has been extruded into the wellbore) located in the annulus between the casing/liner and the bore hole wall.
B. Function	The purpose of the element is to provide a continuous, permanent and impermeable hydraulic seal along the casing annulus to prevent flow of formation fluids and to resist pressures from above and below.
C. Design, construction and selection	1. The element shall be capable of providing an eternal hydraulic pressure seal. 2. The minimum cumulative formation interval shall be 50 m MD. 3. The minimum formation stress at the base of the element shall be sufficient to withstand the maximum pressure that could be applied. 4. The element shall be able to withstand maximum differential pressure.
D. Initial test and verification	1. Position and length of the element shall be verified by bond logs: a) Two (2) independent logging measurements/tools shall be applied. Logging measurements shall provide azimuthal data. b) Logging data shall be interpreted and verified by qualified personnel and documented. c) The log response criteria shall be established prior to the logging operation. d) The minimum contact length shall be 50m MD with 360 degrees of qualified bonding. 2. The pressure integrity shall be verified by application of a pressure differential across the interval. 3. Formation integrity shall be verified by a LOT at the base of the interval. The results should be in accordance with the expected formation stress from the field model (see table 15.51 In-situ formation). 4. If the element has been qualified by logging, pressure and formation integrity testing, logging is considered sufficient for subsequent wells. The formation interval shall be laterally continuous. Pressure testing is required if the log response is not conclusive or there is uncertainty regarding geological similarity.
E. Use	The element is primarily used in a permanently abandoned well.
F. Monitoring	None
G. Common well barrier	None

Figure 0.3: Acceptance Criteria for use of creeping formations in P&A (Norwegian Petroleum Safety Authority, 2013)

Introduction to the Geomechanical Problem

There exist several potential displacement mechanisms which can make a clay-rich rock deform radially inwards into the borehole. Elastic deformation as described by conventional linear elasticity theory is generally too small (as will be shown later). However elasto-plastic deformation may be enough for certain cases. Creep, which can be regarded as time dependent

plastic deformation is believed to be enough in many cases and is viewed upon as the main phenomenon leading to formation barriers (Williams, et al., 2009). In addition it is well known that some clay minerals has the ability to swell when in contact water and given certain chemical conditions, this swelling can potentially facilitate the displacement mechanisms. A section concerning swelling clays and its potential effects on creep is given in section 0.

1.4 Plastic Deformation

The creeping ability of shale and other weak rocks tends to reduce the deviatoric stresses in the formation over geological time, (sometimes) to the extent that the present-day stress state can be considered quasi-isotropic. In other words, the difference between the overburden gradient (stress from weight of overburden) and the horizontal stress gradients are small, and this difference can be thought of as a threshold for the formation for creeping (Su, 2013). Consider a formation with isotropic horizontal stress, if a vertical well is drilled it will create a disturbance in the stress field as the stresses in the borehole are now represented by the well pressure rather than the formation stresses, see Figure 0.1 (a). This disturbance might be enough to reactivate the creeping of the formation, which in practice can be interpreted as the weight of the overburden squeezing the shale inwards in the borehole, progressively shrinking the borehole until it either stabilizes or fails in a brittle manner. During drilling this is usually an unwanted phenomenon as it can lead to tight hole problems such as for example stuck pipe and/or difficulties with setting the casing. Consequently, the forces created by the drilling mud should be sufficient to prevent or at least keep the rate and degree of hole closure within the tolerance margin. Preventative measures, for example having a larger margin between the borehole wall and the casing and/or using non-aqueous based mud (NABM), are thus often considered. Following a similar example as discussed in (Fjaer, et al., 2016): assuming a circular hole in an isotropic, linearly elastic formation, it can be shown that the radial displacement *u* at a distance *r* from the borehole center due to drillout can be written as (Fjaer, et al., 2008):

$$u(r) = \frac{\sigma_h - p_w}{2G_{fr}} \frac{R_w^2}{r} \qquad \textbf{0.1}$$

Where σ_h is the far field horizontal stress, p_w is the well pressure, R_w is the borehole radius and G_{fr} is the shear modulus of the rock frame (also known as dry shear modulus). For a typical casing with outer diameter (OD) of 10 ¾“ the standard borehole size is typically 12 1/4 “ or 14 3/4“. If a formation is suspected to have creeping abilities the more conservative option is the natural choice, giving geometry as shown in Figure 0.1 (b).

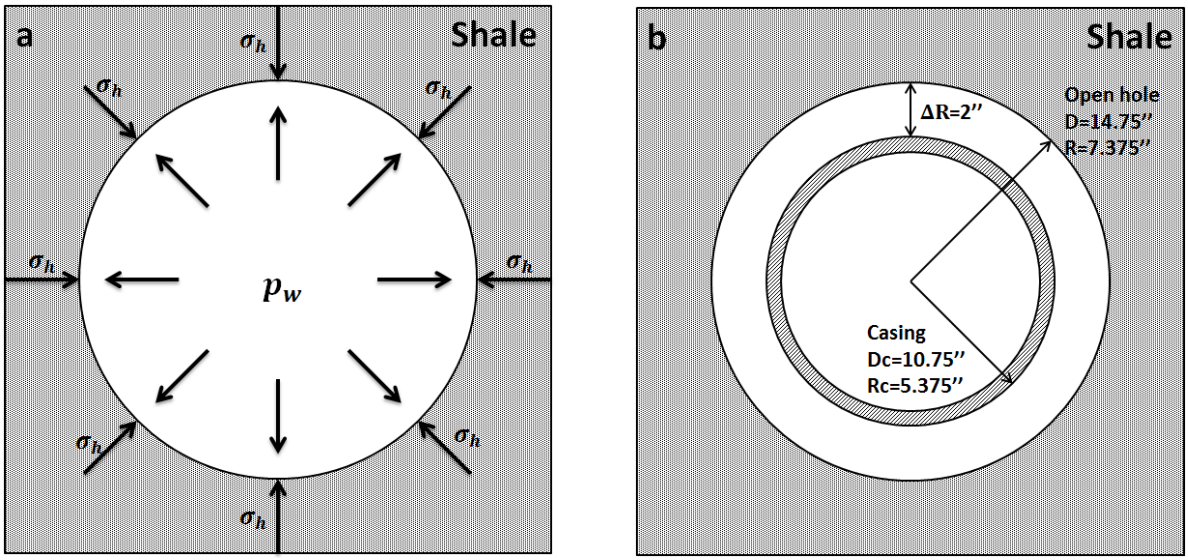

Figure 0.1: (a) Simplified figure showing the horizontal forces in play. p_w is the well pressure and is created by the weight of the drilling fluid and σ_h is the external pressure created by the formation. (b) Borehole geometry for the example

By inserting the borehole radius R_w into equation 0.1 and rearranging, the amount of deformation required can be expressed in terms of strain:

$$\epsilon_r = \frac{\Delta R}{R_w} = \frac{\sigma_h - p_w}{2G_{fr}} \qquad 0.2$$

Where ϵ_r is the strain in radial direction and ΔR is the change in borehole radius and is equal to $u(R_w)$. For a casing with $10^{3/4"}$ OD and boreholes of $12^{1/4"}$ and $14^{3/4"}$ the amount of strain the formation at the borehole wall must undergo to close the annular gap is 12.24% and 27.12% respectively. Assuming a depth of 2000 meter and a gradient difference of 0.5 SG (specific gravity) between the well pressure gradient and the horizontal stress gradient (unusually high) gives a pressure difference ($\sigma_h - p_w$) of around 9.8 MPa. In order to close the gap between the formation and the casing completely by elastic deformation only, the shear modulus G_{fr} would have to be 40.05MPa and 18.08MPa for the 12 1/4“ and 14 3/4“ casings respectively. Such values for the shear modulus are extremely low for anything but very shallow formations, typically the shear modulus for shales around 2000m depth are in at least one order of magnitude larger. Suggesting that in realistic scenarios elastic deformation alone is not enough to create an annular barrier, it is therefore adequate to assume that plastic deformation is required. Since many shales in general are so-called plastic materials they are often good candidates for forming barriers.

Introduction to Plasticity Modelling

Part of this thesis derives and uses an elastoplastic hollow cylinder model in an attempt to predict the convergence of the borehole wall in a shale formation (see section 0). This section will therefore elaborate some general theory about plasticity in rocks which will be used later in the derivation of the elastoplastic hollow cylinder model. The following section is mainly based upon the discussions "Beyond the yield point" from (Fjaer, et al., 2008) and "Inelastic behavior" from (Jaeger, et al., 2008).

To solve more complex problems than just uniaxial compression tests, one need mathematical functions for modeling/approximating the stress versus strain behavior. Conventional elasticity theory typically approximates stress and strain as a linear relationship governed by Hooke's law (equation 0.23). However as illustrated in the example above the main strain contribution in a barrier forming process must be plastic. Below follows some concepts of plasticity modelling with special emphasis on the Mohr-Coulomb criterion, which is convenient both for the typical wellbore stresses and mathematical simplicity.

1.4.1 The Transition from Elastic to Plastic Strain

Plasticity is used to model ductile failure (does not suit for modeling more brittle rocks/materials) and the yield point is what marks the onset of plastic deformation. The yield point is calculated from a yield criterion, commonly based on the same equations used to predict rock failure. Failure of a rock is often understood as when the rock fractures and loses its ability to carry load comparable to the load before failure occurred. This is so-called brittle failure, and is normal behavior for materials such as for example glass and sandstone. However for some materials (namely clay rich rocks) one often observes that the stress strain graph in a rock test behaves in an inelastic way, while the material maintains the load bearing capacity. The yield point is the point on a stress-strain graph where the relationship ceases to be linear and either a hardening (increase in load bearing capacity) or softening (decrease in load bearing capacity) process occurs.

Prior to yielding all deformation in a rock is considered elastic and a key characteristic for elastic deformation is that it is reversible, meaning that if the stresses return to original state so will the strains/deformation. However, once the yield criterion is fulfilled some fraction of the deformation will be plastic and this deformation will remain if stresses are reversed back to original state. Provided that the strains are small enough one can assume that the total strain

increment as a result of a stress increment is the sum of an elastic part and a plastic part, expressed mathematically as (Fjaer, et al., 2008) (Jaeger, et al., 2008):

$$d\epsilon_{ij} = d\epsilon_{ij}^{e} + d\epsilon_{ij}^{p} \quad \textbf{0.1}$$

Where $d\epsilon_{ij}$ represents the total strain increment and $d\epsilon_{ij}^{e}$ and $d\epsilon_{ij}^{p}$ represents the elastic and plastic parts of the strain increment respectively. The elastic part of the strain is related to the stresses by Hooke's law, but in order to model the total strain the plastic part must also be related to stresses in some way.

One simple model is the (linearly) elastic-perfectly-plastic model, where the strain is purely elastic and governed by conventional elasticity theory until the yield criterion is fulfilled and marks the onset of plastic strain. The stress strain relationship for this model is shown in Figure 0.1. Note that one of the consequences of assuming perfect plasticity is that the amount of plastic strain is not unique for a given stress state (an assumption which matches nicely with creep). Another, slightly more realistic approach is the (linearly) elastic-brittle-plastic model which takes into account that as the rock yields and forms a plastic zone containing micro fractures and other damages, the rock parameters related to strength, will be altered (weakened) in this damaged zone, see Figure 0.1. It is worth noting that despite the name elastic-brittle-plastic the behavior beyond the yield point is not considered brittle failure as the yielded material still has a certain capacity to carry a load (often called residual strength). Brittle failure as per definition used in this thesis is when the material yields and more or less completely loses its ability to carry load.

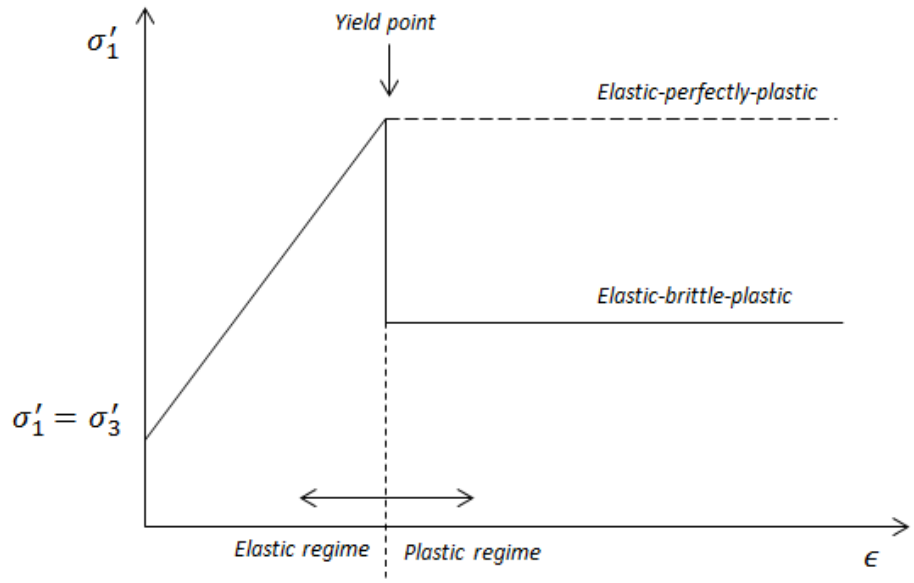

Figure 0.1: Stress strain curve showing elastic-brittle-plastic and elastic-perfectly-plastic behavior

The yield criterion is often chosen on the same basis as a failure criterion and there exists several criteria with varying degrees of complexity and precision. Furthermore it depends on what failure mode the stress state results in e.g. shear failure, tensile failure or compressive failure. Some yield criterions worth mentioning in rock mechanics include Mohr-Coulomb, Tresca, Von Mises, Hoek brown and unified strength theory. Typical borehole conditions are large shear stresses at low confinement, thus plastic deformation as a result of shear failure/yield is most interesting (Fjaer, et al., 2016). The Mohr-Coulomb criterion is widely used for shear failure in rock mechanics and is independent of the intermediate stress and thus is convenient for keeping models fairly simple and will be used to illustrate some concepts in plasticity modelling later in the discussion.

1.4.2 Flow Rules – How the Strain and Stress Distribution Develops

Flow rules are used to model how the strain distributes in a rock for a given stress state. When plotted in principal stress space the yield criteria form surfaces, stress states inside these surfaces results in elastic deformation (often governed by Hooke's law, see equation 0.23). For a perfectly plastic material the assumption is that the yield surface is constant, in other words it is not affected by deformation of the material, this means that the area outside the yield surface represents inaccessible stress states. Once material has yielded and stress state is on the yield surface a further change will either lead the stress state back inside the elastic region or to another point on the yield surface. If the stresses are strictly increasing the material will respond by deforming in such a way that the stress state always remains on the yield surface. In order

to characterize the condition that increased load after a rock has yielded leads to additional plastic strain, a scalar parameter λ is introduced:

$$\frac{df}{d\lambda} = 0 \tag{0.2}$$

Where f is the yield criterion function. Equation 0.2 provides a constraint for the principal stresses during plastic deformation and guarantees that the stress state remains on the yield surface. Note that λ can and generally will vary both with time and space and is not a material constant. Von Mises made the assumption that the plastic flow can be modeled by the following equation:

$$d\epsilon_{ij}^{p} = d\lambda \frac{\partial g}{\partial \sigma_{ij}'} \tag{0.3}$$

Where $d\epsilon_{ij}^{p}$ is the plastic strain increment, g is the plastic potential (a function in stress space) and σ_{ij}' is the stress. According to (Drucker, 1950) and classical plasticity theory, the plastic strain increment is normal to the yield surface and thus the plastic potential function g is equal to the yield criterion. In other words once the yield criterion is defined so is the plastic flow rule. Flow rules based on this assumption are called an associated flow rules, as they are directly associated with the yield criterion. While this is convenient mathematically the results are not always matched by real rocks.

This is well illustrated by taking a closer look on the Mohr-Coulomb criterion:

$$\sigma_1' - \frac{1+\sin(\phi)}{1-\sin(\phi)}\sigma_3' - \frac{2c \cdot \cos(\phi)}{1-\sin(\phi)} = 0 \tag{0.4}$$

Here σ_1' represents the largest effective principal stress, σ_3' the smallest effective principal stress, ϕ the friction angle (rock parameter) and c the cohesion (rock parameter). A common way to write the Mohr-Coulomb criterion is:

$$\sigma_1' - \tan(\gamma)\,\sigma_3' - C_0 = 0 \tag{0.5}$$

Where C_0 often is called the uniaxial compressive strength (UCS) (when $\sigma_3' = 0$) and the angle γ is shown in Figure 0.2 and mathematically related to the friction angle as:

$$\tan(\gamma) = \frac{1+\sin(\phi)}{1-\sin(\phi)} \tag{0.6}$$

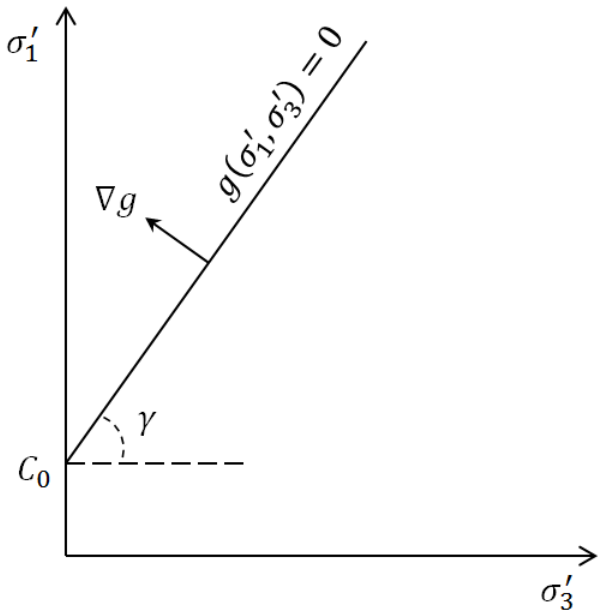

Figure 0.2: Mohr-Coulomb criterion and the direction of its gradient plotted in stress space

In Figure 0.2 g is the plastic potential and for this case equal to the yield criterion, and ∇g is the gradient of the yield criterion. The associated flow rule states that the plastic strain increment is normal to the yield criterion, in the case the of the Mohr-Coulomb criterion it becomes:

$$\nabla g = \left(\frac{\partial g}{\partial \sigma_1'}, \frac{\partial g}{\partial \sigma_2'}, \frac{\partial g}{\partial \sigma_3'}\right) = (1, 0, -\tan(\gamma)) \quad \textbf{0.7}$$

Thus the plastic strain components becomes:

$$d\epsilon_1^p = d\lambda, \qquad d\epsilon_2^p = 0, \qquad d\epsilon_3^p = -d\lambda \tan(\gamma) \quad \textbf{0.8}$$

And the total plastic strain:

$$d\epsilon_v^p = d\epsilon_1^p + d\epsilon_2^p + d\epsilon_3^p = d\lambda(1 - \tan(\gamma)) = d\epsilon_1^p \left(1 - \frac{1 + \sin(\phi)}{1 - \sin(\phi)}\right) \quad \textbf{0.9}$$

The allowable range for the friction angle ϕ is 0-90°, typically concentrated around 30° (Fjaer, et al., 2008), which means that $d\epsilon_1^p$ and $d\epsilon_v^p$ will have different signs, thus if a rock is compressed in the direction of the maximum principal stress ($d\epsilon_1^p > 0$) then the plastic volumetric strain will in fact be increasing ($d\epsilon_v^p < 0$). This phenomenon of volume increase is termed dilatancy and while it is observed in many rocks it is usually not to the degree as predicted by equation 0.9, (Fjaer, et al., 2008).

Therefore one often chooses to relax the assumption that the plastic strain is normal to the yield surface, in order to control dilatancy (read: expansion) without having to alter the yield

criterion. Typically, this is done by introducing a new angle ψ called dilatancy angle in place of the friction angle, for the case of Mohr-Coulomb the plastic potential function g will then thake the form:

$$g(\sigma_1', \sigma_3') = \sigma_1' - \frac{1 + sin(\psi)}{1 - sin(\psi)}\sigma_3' - \frac{2c \cdot cos(\psi)}{1 - sin(\psi)} = 0 \qquad \textbf{0.10}$$

By modifying the dilatancy angle one can control the volume change until it matches experimental observations. Since the plastic potential is no longer the same function as the yield criterion this type of flow rule is called non-associated flow rule.

1.4.3 Deformation Effects on Rock Parameters

Realistically a real stress strain graph will look something more like Figure 0.3. Simply put, one can say that as a ductile/plastic material yields and undergoes irreversible strain the rock deforms and thus also changes its properties. Strain hardening refers to when the strength of the rock increases in other words when a larger amount of stress is required to keep deforming/straining the rock whereas strain softening reduces the required stress for deformation. The behaviors can both be seen below in Figure 0.3 in the ductile region, the material displays the strain hardening effect from the yield point (yield stress) until it reached the UCS after which it undergoes a softening process and eventually enters brittle failure mode. Note that this is a generic stress strain graph and that real graphs can be very different.

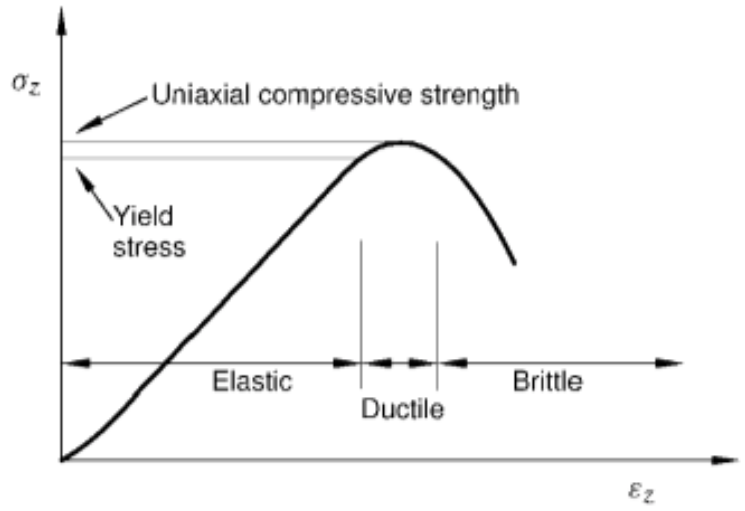

Figure 0.3: Stress vs strain (deformation) in a uniaxial compression test (Fjaer, et al., 2008)

An Elastoplastic Hollow Cylinder Model with Pore Pressure Profile

There exists several analytical and semi analytical solutions with varying degree of complexity for the deformations in a hollow cylinder subjected to boundary pressures, see for example (Chen, et al., 1999) (Fjaer, et al., 2008) (Zhang, et al., 2012) (Liu, et al., 2011). The following model is inspired by and follows much of the same procedures as in (Chen, et al., 1999), but also allows residual strength parameters as well as a non-constant pore pressure profile.

The following unpublished model is developed by Kun Su in the software Maple (2016.1). It is worth mentioning that Maple is very sensitive to the inputs used and will for many cases crash without finding a solution for the differential equation (equation 0.37), despite the same equation consistently being solved by for example Wolfram Alpha (WolframAlpha, 2017). In order to get a good understanding of the geomechanical problem, and perform a proper analysis of the model, a derivation of the semi-analytical solution is performed by the author. This derivation also opens up the possibility of easily incorporating the model to other software. Afterwards a comparison with a hollow cylinder lab experiment is conducted in addition to an analysis of how it is affected by different conditions and small changes to the model are suggested. In the end, its applicability for borehole problems will be discussed and it will be used for the relevant P&A case.

1.5 Derivation of Stress Distribution

Consider an infinitely long hollow cylinder made of homogenous and isotropic material with inner radius R_w and outer radius R_o. The cylinder is loaded with an axial stress σ_v, an internal pressure p_w and an external pressure σ_{ro}, see Figure 0.1. The internal and external pressures are for all times normal to the surfaces and thus independent of θ and z. By adopting a cylindrical coordinate system with the z-axis in the center of the hollow cylinder the coordinate axes will also represent the principal stress directions. With the assumptions made it is then clear that the only deformation will take place in the radial direction and the conditions for plane strain and axisymmetry are assumed appropriate.

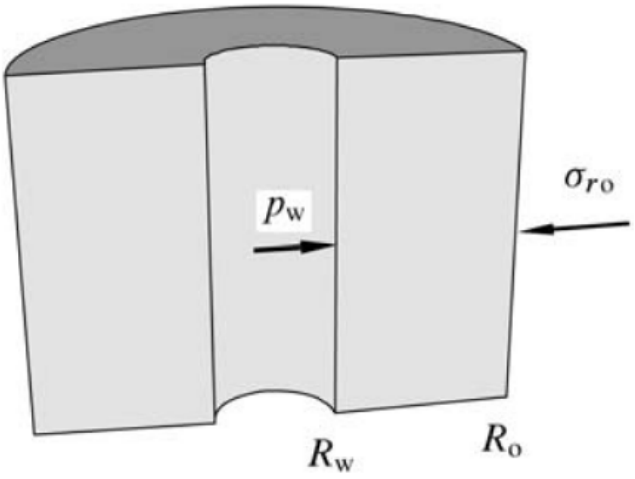

Figure 0.1: Section of the hollow cylinder model (Fjaer, et al., 2008)

The material is linearly elastic up until yield which is governed by the Mohr Coulomb criterion:

$$\sigma_1' - m\sigma_3' - C_0 = 0 \tag{0.1}$$

Where C_0, m and σ' are given as:

$$m = \frac{1 + \sin(\phi)}{1 - \sin(\phi)} \tag{0.2}$$

$$C_0 = \frac{2c \cdot \cos(\phi)}{1 - \sin(\phi)} \tag{0.3}$$

$$\sigma' = \sigma - \alpha p_f \tag{0.4}$$

Like in section 0, σ_1' is the largest effective principal stress, σ_3' is the smallest effective principal stress, ϕ is the friction angle, c is the cohesion, α is biots constant (often assumed to be 1) and p_f is the pore pressure.

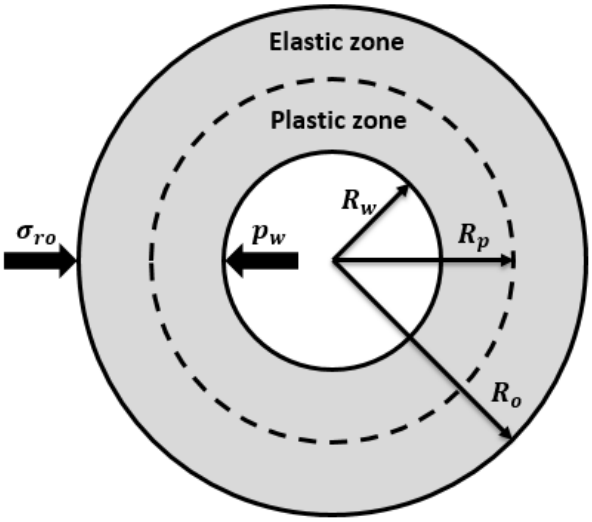

Figure 0.2: Cross sectional view of the hollow cylinder model

1.5.1 Stress Distribution

When the material yields a circular plastic zone develops as depicted in Figure 0.2, where R_p represents the distance from the center of the cylinder to the interface between the elastic and plastic zone. After the material has yielded it is realistic to assume that the strength of the material in the plastic zone is altered, this is done by introducing an altered cohesion parameter c_p, changing the UCS in the plastic zone as follows:

$$C_0^p = \frac{2c_p \cdot \cos(\phi)}{1 - \sin(\phi)} \quad \textbf{0.5}$$

Post yield the stress state is determined by the yield criterion with the altered strength parameter C_0^p:

$$\sigma_1' - m\sigma_3' - C_0^p = 0 \quad \textbf{0.6}$$

It is worth noting that there are different ways of modelling the reduced strength in the plastic zone. One solution is to change the Young's modulus as shown by (Zhang, et al., 2012), other options include changing several rock parameters in the yielded zone. However the complexity of the mathematical formulation and the stability of the software used increases rapidly for every new element introduced, thus in order to keep it fairly simple in this derivation only the cohesion parameter will be altered.

Unlike (Zhang, et al., 2012) and (Chen, et al., 1999), this solution attempts to model the hollow cylinder problem with a non-constant pore pressure. The pore pressure variation is assumed to be given by stationary radial flow with constant pressure p_o at some outer radius R_o, the pore pressure p_f for a radius r then takes the form (Fjaer, et al., 2008):

$$p_f = p_o + \frac{p_o - p_i}{ln\left(\frac{R_o}{R_w}\right)} ln\left(\frac{r}{R_o}\right) \quad \textbf{0.7}$$

Where p_i is the pore pressure at the inner wall with radius R_w. By ignoring body forces, the equations of equilibrium can then be simplified to a single equation (Fjaer, et al., 2008):

$$\frac{d\sigma_r}{dr} + \frac{\sigma_r - \sigma_\theta}{r} = 0 \quad \textbf{0.8}$$

Assuming that $\sigma_1' = \sigma_\theta'$, $\sigma_2' = \sigma_z'$ and $\sigma_3' = \sigma_r'$ (as is often the case for borehole problems) and substituting equation 0.4 into equation 0.8 then yields:

$$\frac{d\sigma_r'}{dr} + \frac{\alpha A}{r} + \frac{\sigma_r' - \sigma_\theta'}{r} = 0 \quad \textbf{0.9}$$

Where:

$$A = \frac{p_o - p_i}{ln\left(\frac{R_o}{R_w}\right)} \quad \textbf{0.10}$$

Inserting equation 0.1 into equation 0.9 gives the following equation for the plastic zone:

$$\frac{d\sigma_{rp}'}{dr} + \frac{\sigma_{rp}'(1-m)}{r} + \frac{\alpha A}{r} - \frac{C_0^p}{r} = 0 \quad \textbf{0.11}$$

Solving this equation for σ_r' using the boundary condition that the effective radial stress at the borehole wall is equal to the effective well pressure/mud pressure: $\sigma_{rp}'(r = R_w) = p_w' = p_w - p_i$, gives the effective radial stress in the plastic zone σ_{rp}' as:

$$\sigma_{rp}' = \frac{\alpha A - C_0^p}{m-1} - \left[\frac{r^{(m-1)}\left(\frac{\alpha A - C_0^p}{m-1} - p_w'\right)}{R_w^{(m-1)}}\right] \quad \textbf{0.12}$$

Substituting 0.12 into 0.1 one finds the effective tangential stress in the plastic zone $\sigma_{\theta p}'$ to be:

$$\sigma_{\theta p}' = m\left[\frac{\alpha A - C_0^p}{m-1} - \left[\frac{r^{(m-1)}\left(\frac{\alpha A - C_0^p}{m-1} - p_w'\right)}{R_w^{(m-1)}}\right]\right] + C_0^p \quad \textbf{0.13}$$

The total plastic stresses can easily be found by using equation 0.4. The elastic stresses in a hollow cylinder with pore pressure profile as in equation 0.7 was solved by (Risnes, et al., 1982), by considering the inner radius of the elastic zone as R_p instead of R_w the equations for

tangential stress σ_θ and radial stress σ_r in the elastic zone as a function of radius r can be written as:

$$\sigma_r = \sigma_{ro} + \left(\sigma_{ro} - \sigma_{rp}^{R_p}\right)\frac{R_p^2}{R_o^2 - R_p^2}\left[1 - \left(\frac{R_o}{r}\right)^2\right] - (p_o - p_{fp})\eta\left[\frac{R_p^2}{R_o^2 - R_p^2}\left[1 - \left(\frac{R_o}{r}\right)^2\right] + \frac{\ln(R_o/r)}{\ln(R_o/R_p)}\right] \quad \textbf{0.14}$$

$$\sigma_\theta = \sigma_{ro} + \left(\sigma_{ro} - \sigma_{rp}^{R_p}\right)\frac{R_p^2}{R_o^2 - R_p^2}\left[1 + \left(\frac{R_o}{r}\right)^2\right] - (p_o - p_{fp})\eta\left[\frac{R_p^2}{R_o^2 - R_p^2}\left[1 + \left(\frac{R_o}{r}\right)^2\right] + \frac{\ln(R_o/r) - 1}{\ln(R_o/R_p)}\right] \quad \textbf{0.15}$$

Where $\sigma_{rp}^{R_p}$ is the radial stress at the elastic-plastic interface and is found by inserting the radius of the plastic zone R_p into equation 0.12 and adding the pore pressure:

$$\sigma_{rp}^{R_p} = \frac{\alpha A - C_0^p}{m-1} - \left[\frac{R_p^{(m-1)}\left(\frac{\alpha A - C_0^p}{m-1} - p_w'\right)}{R_w^{(m-1)}}\right] + \alpha p_{fp} \quad \textbf{0.16}$$

p_{fp} is the pore pressure at the plastic-elastic interface, found by inserting the radius of the plastic zone R_p in to equation 0.7:

$$p_{fp} = p_o + A\ln\left(\frac{R_p}{R_o}\right) \quad \textbf{0.17}$$

And η:

$$\eta = \frac{1 - 2v_{fr}}{2(1 - v_{fr})}\alpha \quad \textbf{0.18}$$

Here v_{fr} is the Poisson ratio of the material. Once again the effective stresses in the elastic zone can be found by using equation 0.4.

1.5.2 Radius of the Plastic Zone

At the interface between the plastic and elastic zone there must be continuity in the radial stress (there is also continuity in the tangential stress for cases where $C_0 = C_0^p$):

$$\sigma_{rp} = \sigma_r \quad \textbf{0.19}$$

By inserting equation 0.14 and 0.12 (with added pore pressure from 0.7 as seen in 0.4) into equation 0.19 a non-linear equation is generated. (However for numerical programming reasons

it was found more convenient solve the following version of the equation instead.) Since the yield criteria (equation 0.1 and 0.6) must be satisfied at the elastic-plastic interface equation 0.19 can be rewritten as (assuming same friction angle ϕ in both plastic and elastic zone):

$$\sigma'_{\theta p} - C_0^p = \sigma'_\theta - C_0\,, \quad for\ r = R_p \tag{0.20}$$

Writing the expression out gives:

$$m\left[\frac{\alpha A - C_0^p}{m-1} - \left[\frac{R_p^{(m-1)}\left(\frac{\alpha A - C_0^p}{m-1} - p'_w\right)}{R_w^{(m-1)}}\right]\right] \tag{0.21}$$

$$= \sigma_{ro} + \left(\sigma_{ro} - \sigma_{rp}^{R_p}\right)\frac{R_p^2}{R_o^2 - R_p^2}\left[1 - \left(\frac{R_o}{R_p}\right)^2\right]$$

$$- \left(p_o - p_{fp}\right)\eta\left[\frac{R_p^2}{R_o^2 - R_p^2}\left[1 - \left(\frac{R_o}{R_p}\right)^2\right] + \frac{\ln\left(R_o/R_p\right)}{\ln\left(R_o/R_p\right)}\right] - \alpha p_{fp}$$

$$- C_0$$

This non-linear equation is then solved numerically to find the radius of the plastic zone R_p. (Several solutions exists so make sure the condition $R_w \leq Rp < R_o$ is fulfilled, visual inspection by the equation is recommended).

1.5.3 Strain in the Elastic Zone

(Some discussion about how to model the axial stress is shown later, but in this derivation it is assumed to be given by Hooke's law and the plain strain condition)

The radial and tangential strains in cylinder coordinates can be expressed as (Fjaer, et al., 2008):

$$\begin{Bmatrix}\epsilon_r \\ \epsilon_\theta\end{Bmatrix} = \begin{Bmatrix}\frac{du}{dr} \\ \frac{u}{r}\end{Bmatrix} \tag{0.22}$$

Prior to yielding the stresses are related to strain by Hooke's law:

$$\begin{Bmatrix}\epsilon_\theta \\ \epsilon_z \\ \epsilon_r\end{Bmatrix} = \frac{1}{E}\begin{bmatrix}1 & -\upsilon_{fr} & -\upsilon_{fr} \\ -\upsilon_{fr} & 1 & -\upsilon_{fr} \\ -\upsilon_{fr} & -\upsilon_{fr} & 1\end{bmatrix}\begin{Bmatrix}\Delta\sigma'_\theta \\ \Delta\sigma'_z \\ \Delta\sigma'_r\end{Bmatrix} \tag{0.23}$$

Where E is Young's modulus, $\epsilon_\theta, \epsilon_z, \epsilon_r$ are the principal strains and $\Delta\sigma'_\theta, \Delta\sigma'_z, \Delta\sigma'_r$ are the changes in the effective principal stresses. Combining the equations 0.14 and 0.15 with 0.23

(plane strain assumption gives $\epsilon_2 = \epsilon_z = 0$) a solution for radial displacement in the elastic zone u_e is obtained:

$$u_e = \frac{r}{E}\left[\Delta\sigma'_\theta - v_{fr}\left[\Delta\sigma'_r + v_{fr}(\Delta\sigma'_r + \Delta\sigma'_\theta)\right]\right] \quad \textbf{0.24}$$

Where $\Delta\sigma'_\theta$ and $\Delta\sigma'_r$ are the changes in effective tangential and radial stresses. By inserting equation 0.7, 0.14 and 0.15 the equation for elastic radial displacement u_e as a function of radius r, can then be expressed by material $\left(E, v_{fr}, \alpha,\ C_0, C_0^p\ and\ \phi\right)$ and boundary properties $\left(R_o, R_w, R_p\ and\ \sigma_{ro}, p_w, \sigma_{rp}^{R_p}\ and\ \ p_o, p_p, p_o\right)$. The expression is quite long and also depending on the initial stress state. This derivation will consider the special case of $\sigma'_{\theta_{initial}} = \sigma'_{r_{initial}} = p_{w_{initial}} = \sigma'_{ro_{initial}} = \sigma'_h$, (for more flexible use σ'_h, can be set to 0, and two calculations can be made in order to simulate the final displacement) which is representative of a formation before it is drilled, the expression for elastic radial displacement u_e can then be written as:

$$u_e = \left[\left[A(k_1 r^2 + k_2) ln\left(\frac{R_p}{R_o}\right) + k_3 r^2 + k_4\right] ln\left(\frac{R_o}{R_p}\right) - \left(\eta A ln\left(\frac{R_p}{R_o}\right)\left[\left(v - \frac{1}{2}\right) ln\left(\frac{R_o}{r}\right) - \frac{1}{2}v + \frac{1}{2}\right]\right) r^2\right]\frac{k_5}{r} \quad \textbf{0.25}$$

Where k_1, k_2, k_3, k_4, k_5 are constants:

$$k_1 = \left(v - \frac{1}{2}\right)\left[\alpha - \left(\frac{R_p^2}{R_o^2 - R_p^2}\right)\eta\right] \quad \textbf{0.26}$$

$$k_2 = \frac{1}{2}\left(\frac{R_p^2}{R_o^2 - R_p^2}\right) R_o^2 \eta \quad \textbf{0.27}$$

$$k_3 = \left(v - \frac{1}{2}\right)\left[\left(\sigma_{rp}^{R_p} - \sigma_{ro}\right)\left(\frac{R_p^2}{R_o^2 - R_p^2}\right) + \alpha p_o + \sigma'_h - \sigma_{ro}\right] \quad \textbf{0.28}$$

$$k_4 = \frac{1}{2}\left(\frac{R_p^2}{R_o^2 - R_p^2}\right) R_o^2 \left(\sigma_{ro} - \sigma_{rp}^{R_p}\right) \quad \textbf{0.29}$$

$$k_5 = \frac{2(v+1)}{E ln\left(\frac{R_o}{R_p}\right)} \quad \textbf{0.30}$$

1.5.4 Strain in the Plastic Zone

The elastic strains in the plastic zone are found by inserting equation 0.12 and 0.13 into equation 0.23. Combined with the relationship in equation 0.22 the elastic contribution to the radial displacement in the plastic zone becomes:

$$u_p^e = (k_6 - k_7 r^{m-1}) k_8 r \tag{0.31}$$

Where k_6, k_7 and k_8 are constants:

$$k_6 = R_w^{(m-1)} \Big[\Big[2(1-m)\sigma_h' + \alpha A(m+1) - 2C_0^p \Big] v + (m-1)\sigma_h' - \alpha A m + C_0^p \Big] \tag{0.32}$$

$$k_7 = [(v-1)m + v]\big[\alpha A - C_0^p + p_w'(1-m)\big] \tag{0.33}$$

$$k_8 = -\frac{v+1}{(m-1)ER_w^{(m-1)}} \tag{0.34}$$

Using the same procedure as in section 1.4.2 the non-associated plastic potential function equation 0.10 is chosen and the plastic strain relationship can then be established as:

$$d\epsilon_\theta^p = d\lambda, \;\; d\epsilon_z^p = 0, \;\; d\epsilon_r^p = -d\lambda \tan(\gamma) = -d\epsilon_\theta^p \left(\frac{1+\sin(\psi)}{1-\sin(\psi)} \right) = -d\epsilon_\theta^p n \tag{0.35}$$

Rearranging the strain relationship in equation 0.22 gives:

$$\epsilon_r = \epsilon_\theta + r\frac{d\epsilon_\theta}{dr} \tag{0.36}$$

By adapting small strain theory (assuming it is applicable in this case), combining equation 0.1 with 0.36 and using the relationship from 0.35 form the following first-order linear ordinary differential equation:

$$\epsilon_\theta^p (1+n) + r\frac{d\epsilon_\theta^p}{dr} = \epsilon_r^e - \epsilon_\theta^e - r\frac{d\epsilon_\theta^e}{dr} \tag{0.37}$$

Where ϵ_r^e and ϵ_θ^e are the elastic strain components in the plastic zone. Equation 0.37 can be rewritten by using equation 0.22 0.23 and 0.31 to:

$$\frac{u_p^p}{r}(1+n) + r\frac{d}{dr}\left(\frac{u_p^p}{r}\right) = (k_9 r^{m-1} + k_{10}) k_{11} \tag{0.38}$$

Where:

$$k_9 = (v-1)(1+m)(\alpha A - C_0^p + p_w'(1-m)) \tag{0.39}$$

$$k_{10} = \alpha A R_w^{(m-1)} \tag{0.40}$$

$$k_{11} = -\frac{v+1}{ER_w^{(m-1)}} \tag{0.41}$$

The boundary condition is that there must be continuity in displacement at the elastic plastic interface, thus at the elastic plastic interface ($r = R_p$), the radial displacement assuming plastic behavior must be equal to the radial displacement assuming elastic behavior. This can be expressed as follows:

$$u^p_{p\_R_p} = u_{e\_R_p} - u^e_{p\_R_p} \tag{0.42}$$

Where $u^p_{p\_R_p}$ and $u^e_{p\_R_p}$ respectively represents the plastic and elastic contribution to radial displacement assuming plastic behavior, and $u_{e\_R_p}$ represents the radial displacement assuming elastic behavior. The plastic contribution to radial displacement in the plastic zone is then:

$$u^p_p = \frac{k_{11}k_9 r^m}{m+n} + \frac{k_{11}k_{10}r}{n+1} - \frac{r^{-n}\left(\frac{k_{11}k_9 R_p^m}{n+m} + \frac{k_{11}k_{10}R_p}{n+1} - u^p_{p\_R_p}\right)}{R_p^{-n}} \tag{0.43}$$

Which makes the total radial displacement in the plastic zone:

$$u_p = u^e_p + u^p_p = (k_6 - k_7 r^{m-1})k_8 r + \frac{k_{11}k_9 r^m}{m+n} + \frac{k_{11}k_{10}r}{n+1} - \frac{r^{-n}\left(\frac{k_{11}k_9 R_p^m}{n+m} + \frac{k_{11}k_{10}R_p}{n+1} - u^p_{p\_R_p}\right)}{R_p^{-n}} \tag{0.44}$$

By choosing $r = R_w$ the convergence of the borehole wall can be calculated. Keep in mind that this is the solution for a borehole with initial conditions where the internal and external pressures are equal. For initial conditions with varying internal and external pressures the same procedure may be followed, but the displacement equations will take a different form.

1.6 Discussion of Derived Solution

The following simulations and results are carried out in the software Maple 2016.1. The author notes that for certain inputs the software appears sensitive, i.e. will not solve all required equations, despite of these equations consistently being solved by for example WolframAlpha (WolframAlpha, 2017). This instability can be fixed by using the solution derived in above.

1.6.1 Comparison with (Chen, et al., 1999) and (Zhang, et al., 2012)

To verify the solution it is compared to a collapse test carried out on a synthetic shale sample under undrained conditions (Chen, et al., 2000). This test has been used to verify similar solutions (Chen, et al., 1999) (Zhang, et al., 2012) and according to them the pore pressure can

be considered constant (5 MPa) throughout all the sample, and is also assumed constant for all the test. The external pressure was kept at $\sigma_{ro} = 68$ MPa throughout the entire test while the internal pressure p_w was 68 MPa initially, and then later decreased by a rate of 0.3 MPa/min down to 6 MPa. The geometry and material properties of the synthetic shale sample are shown in Table 0.1 (Chen, et al., 2000) (Chen, et al., 1999) (Zhang, et al., 2012):

Table 0.1: Inputs

$R_w\ [mm]$	$R_o[mm]$	$p_w[MPa]$	$\sigma_{ro}[MPa]$	$p_i[MPa]$	$p_o[Mpa]$	$E[GPa]$
12.8	39.6	68-6	68	5	5	20.38
ν	c	ϕ [°]	ψ [°]	α		
0.32	6.3	36.2	0	1		

Since the initial internal and external pressure applied to the hollow cylinder sample are identic the expression derived above can be considered valid for this case. To facilitate the comparison to the collapse test, results from the two other similar solutions mentioned (Chen, et al., 1999) (Zhang, et al., 2012) are also included in Figure 0.3 below.

Note that the results plotted from the derived solutions are calculated under the assumption that borehole deformation is the total deformation from both sides of the borehole, and is thus twice the value computed by equation 0.44.

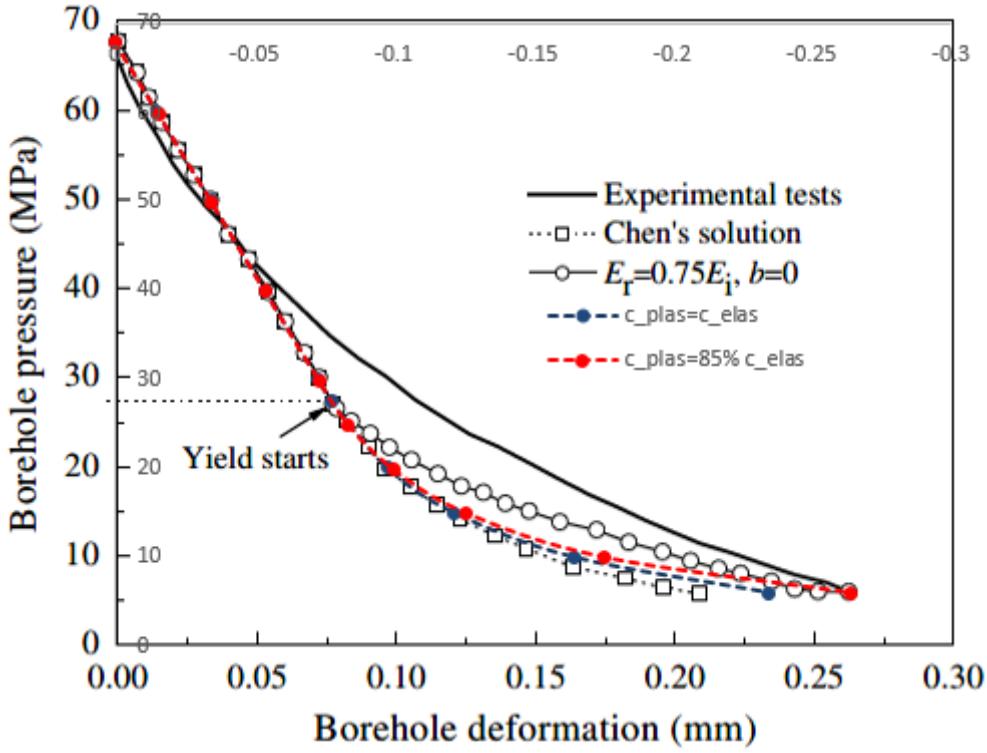

Figure 0.3: Borehole deformation vs borehole pressure (Zhang, et al., 2012), the colored dotted lines represent two cases of the solution derived.

It is found that a plastic cohesion c_p with 85% the value of the elastic cohesion c gives approximately the same final borehole deformation as the test results (see red curve, c_plas=85%c_elas). This alteration of plastic cohesion does not result in very big effects shortly after yield when the radius of the plastic zone is relatively small, but the difference increases as internal pressure decreases and the radius of the plastic zone grows. It can be observed a difference in the displacement results in the plastic regime between the derived solution and Chen's, the difference is also significant when plastic cohesion is equal to elastic cohesion (see blue curve, c_plas=c_elas). The exact reasons for this is not known, but it is most likely just inaccuracy with the graph used for comparison taken from (Zhang, et al., 2012) or different initial conditions, as matching results are found when compared to the graph in (Chen, et al., 1999), and when Chen's solution is used to calculate the deformation with same initial conditions. While the derived solution gives a more accurate approximation than Chen's solution, the solution with radius dependent Young's modulus in the plastic zone by (Zhang, et al., 2012) appears to give an even better approximation of the deformation in this case.

The advantage of the new solution is however the possibility to include a non-constant pore pressure profile and can thus be suspected to more accurately model drained conditions, given that boundary values for the pore pressure are known or can be approximated. Such boundary

values for this test is not reported and are according to the authors expected to not deviate much from the initial values.

Unfortunately it was not found an adequate test under drained conditions to compare with.

1.6.2 Deviations from (Chen, et al., 1999) and (Zhang, et al., 2012)

Without speculating too much about the exact reasons for the deviations from the results reported in (Zhang, et al., 2012), some observations made are discussed below:

Axial Stress

With a constant pore pressure profile and same cohesion in the elastic and plastic zone the radial and tangential stresses in the above derivation reduce to same as in Chen's. The same can be said for Zhang's solution, except more material parameters can be altered in the plastic zone (not only cohesion). However the axial stress differs, in the above derivation the axial stress is given by the plane strain assumption combined with Hooke's law, while in the other solutions it is given as the average of the tangential and radial stress. In order to investigate the effect of the two different ways of modelling the axial stress, the alternative method is also implemented in maple and compared with the original one. (Implementing this in Maple is not complicated, but the changes to the derivation of the semi-analytical expression for radial displacement shown above will not be included here. Also note that unless mentioned otherwise the axial stress in the following results is given as in the derivation above.)

The radial displacement for the two different axial stresses is shown below in Figure 0.4, the inputs are shown in Table 0.1. It is seen that the change in radial displacement is smaller for higher axial stress (as can be expected from Hooke's law) and that the difference between the two methods of modelling axial stress is increasing with the distance from the inner radius, although it is not a very significant change in this case.

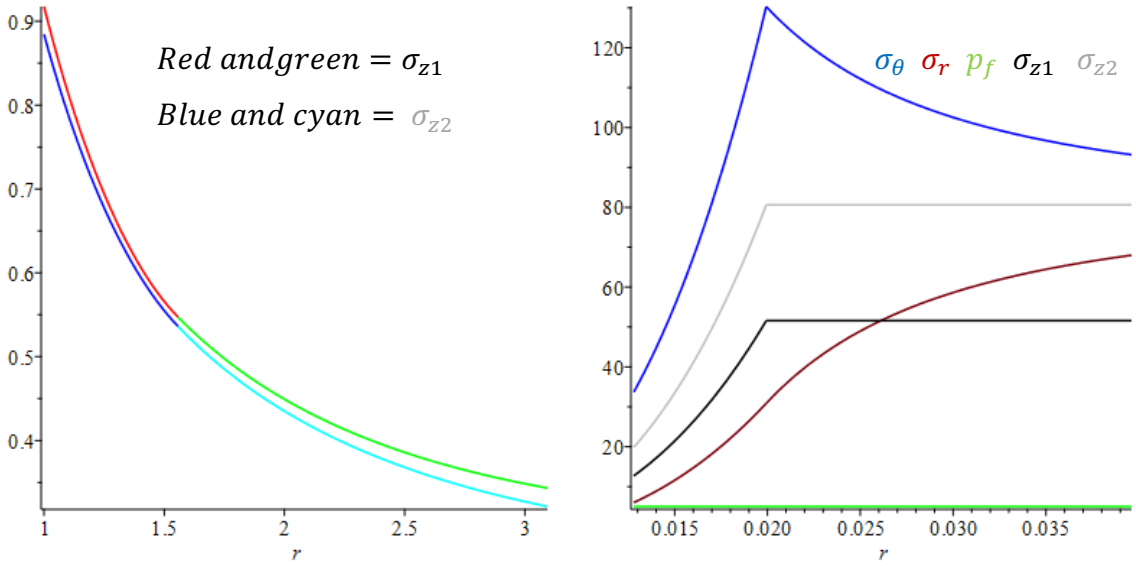

Figure 0.4: Left figure: Dimensionless radial displacement (u/R_w, in %) vs. dimensionless radius (r/R_w), for the two different ways of modelling axial stress, see right figure (all other values are identical). In the graph to the left red and blue represents the plastic zone while green and cyan represents the elastic zone.

However, one important thing to consider is that for the current model the radial stress will not always remain the minimum principal stress for all rock parameters, see for example Figure 0.4 and Figure 0.5. As the stresses in the plastic zone and elastic-plastic interface are governed by the Mohr-Coulomb criterion which is a function of the maximum and minimum principal stresses (assumed to be the radial and tangential stresses for all cases in this model) the model is not theoretically consistent for all input values. The difference in axial and radial stress mainly depends upon Poisson's ratio, as can be seen from relationship between axial and radial stress in the plastic zone:

$$\sigma_z' = v\left[\sigma_r'(1+m) + C_0^p\right] \qquad \textbf{0.45}$$

For rocks with high Poisson's ratio (typical for shale and other weak rocks) the axial stress will often be greater than the radial stress, but for rocks with lower Poisson's ratio it might be smaller. This is illustrated below in Figure 0.5 which is the exact same case as Figure 0.4, but with a poisons ratio of 0.15 instead of 0.32.

The difference in radial displacement between the two different axial stress models are consistently found to be relatively small. Nevertheless, one should consider changing it in order to avoid stress state that disagrees with the assumptions made. According to (Fjaer, et al., 2008) more sophisticated models indicate that the axial stress within the plastic region consists of two zones; the inner plastic zone where the axial stress is equal to the tangential stress and in the outer plastic zone where all the three principal stresses can be different.

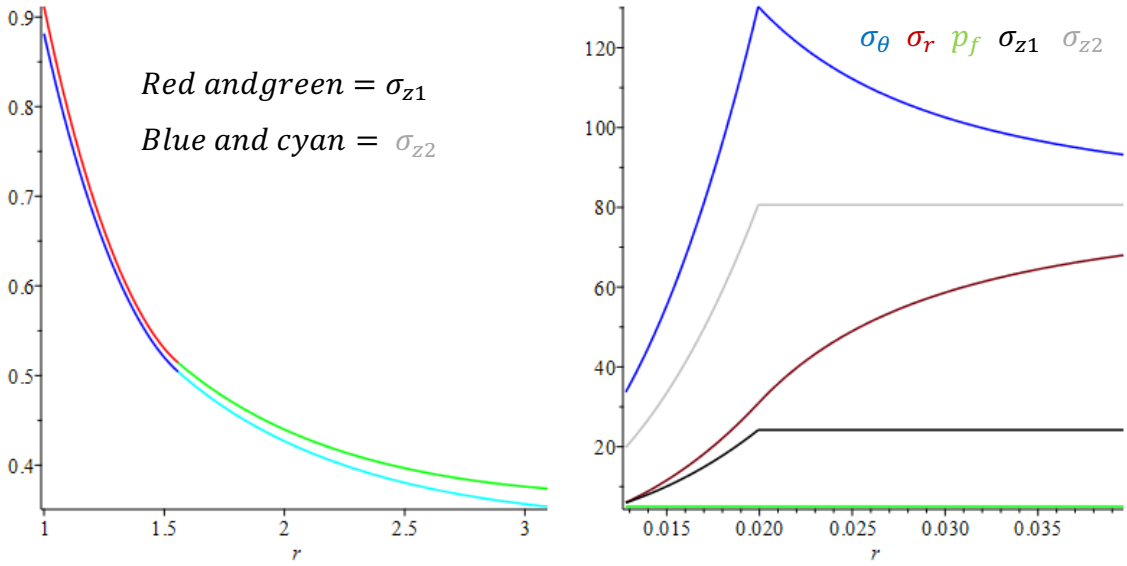

Figure 0.5: Left figure: Dimensionless radial displacement (u/R_w, in %) vs. dimensionless radius (r/R_w), for the two different ways of modelling axial stress, see right figure (all other values are identical). In the graph to the left red and blue represents the plastic zone while green and cyan represents the elastic zone.

Radius Dependent Young's Modulus (RDM)

The radius dependent Young's modulus used in (Zhang, et al., 2012) is given as:

$$E_p(r) = E_{R_w}\left(\frac{r}{R_w}\right)^{\left(\frac{log(E/E_{R_w})}{log(R_p/R_w)}\right)} \quad \textbf{0.46}$$

Where E_p is the Young's modulus in the plastic zone and E_{R_w} is the Young's modulus at $r = R_w$. By implementing this into the model, one can likely better describe the damage variability of a rocks mass in the plastic zone. When $E_{R_w} = E$ the solution reduces to the one derived above (except axial stress). The results of three different E_{R_w} values, for the two different axial stress assumptions are shown below in Figure 0.6 and Figure 0.7 (rest of inputs as given by Table 0.1). As seen, it only changes the displacement in the plastic zone, and only small changes in the radial displacement (>5%) is observed for the different cases.

(Note that after implementing the same axial stress and RDM as in (Zhang, et al., 2012) the obtained results and the ones shown on the graph in Figure 0.3 still differ. Further, the author was not able to recreate results visually displayed in the graph from (Zhang, et al., 2012) (see Figure 0.3) by using the formulas provided in the paper. It was found that the radial displacement decreased for $E_{R_w} < E$, which is a curious result, perhaps linked to initial conditions used, typing errors or figure inaccuracies)

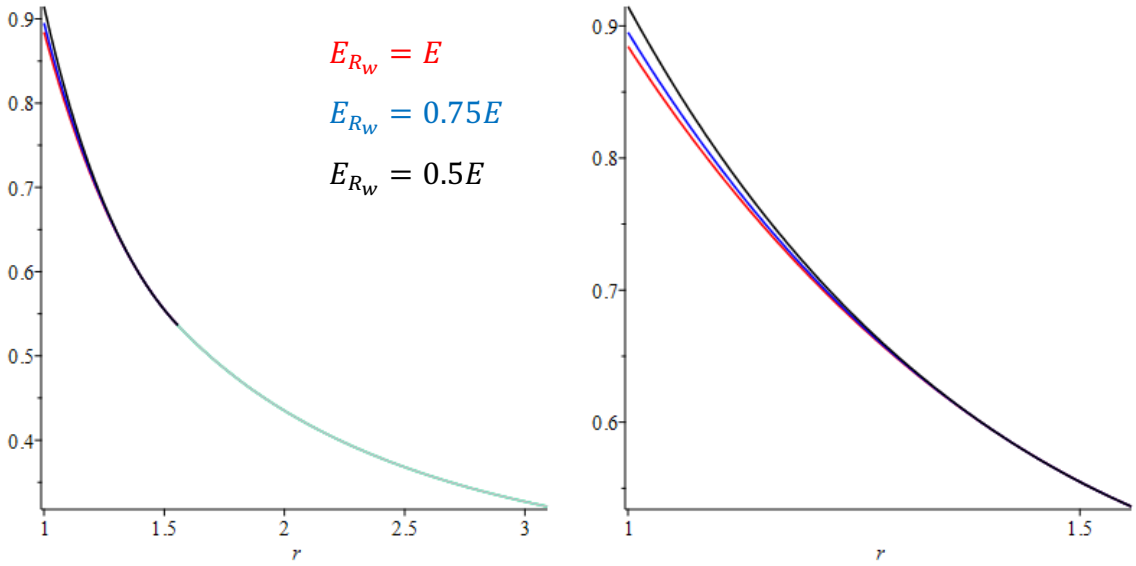

Figure 0.6: Dimensionless radial displacement $(u/R_w,\ in\ \%)$ vs. dimensionless radius (r/R_w), showing the effect of implementing the RDM model. Right graph shows the entire radius of the sample, left graph shows only plastic zone. These results are for axial stress modelled as in (Chen, et al., 1999) and (Zhang, et al., 2012).

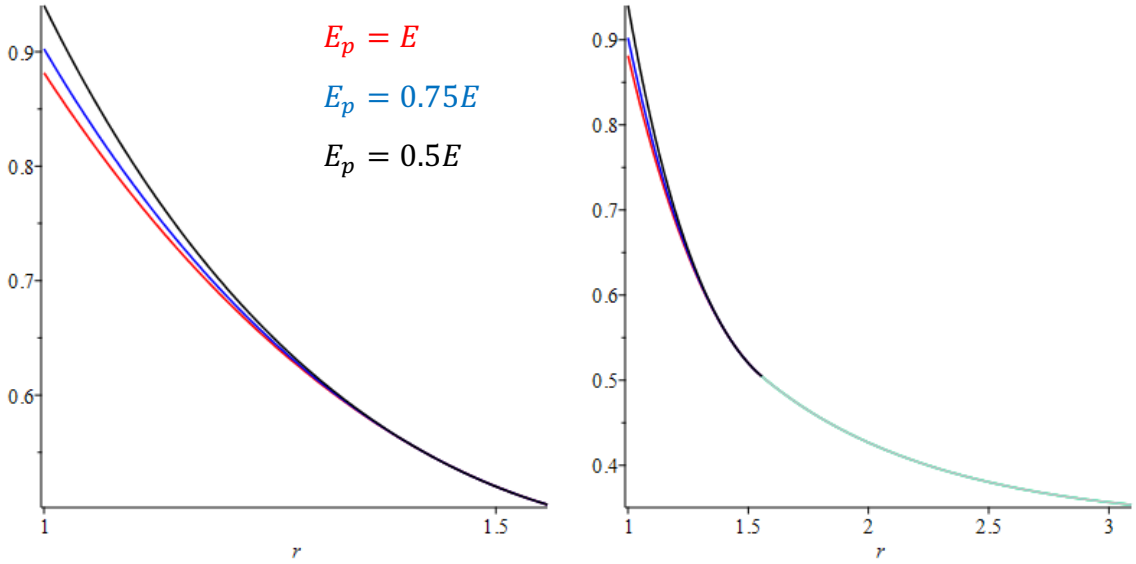

Figure 0.7: Dimensionless radial displacement $(u/R_w,\ in\ \%)$ vs. dimensionless radius (r/R_w), showing the effect of implementing the RDM model. Right graph shows the entire radius of the sample, left graph shows only plastic zone. These results are for axial stress as originally modelled in the derived solution.

Initial Conditions

The differences may also be linked to what is used as initial conditions as this is not made entirely clear in either paper. But results appear to be matching well with graphs from (Chen, et al., 1999), while (Zhang, et al., 2012) has some differences that perhaps are caused partly by initial conditions.

In the end, it is worth noting that initial conditions are directly included in the derivation above although changing this is not complicated, and can be done by setting $\sigma_h' = 0$. From there it is possible to subtract strain which for example is considered a result of consolidation stages.

1.6.3 Pore Pressure Evaluation

The pore pressure is assumed to immediately take a form given by equation 0.7. A more accurate solution is found by solving a diffusion equation given as (Fjaer, et al., 2008) (Kun Su, internal document):

$$C_D \nabla^2 p_f = \frac{\partial p_f}{\partial t} \tag{0.47}$$

Where C_D is the hydraulic diffusivity, p_f is the pore pressure and t is time. For a case where the well pressure p_w initially is equal to the pore pressure p_f and the resulting pore pressure changes are due to change in the well pressure Δp_w, the numerical solution to equation 0.7 is solved by Kun Su (Internal document) and (Detournay & Cheng, 1988). Plotting the dimensionless change in pore pressure $\left(\frac{\Delta p_f}{\Delta p_w}\right)$ as a function of dimensionless time $\left(t' = C_D \frac{t}{R_w^2}\right)$ and dimensionless radial distance into the formation $\left(\frac{r}{R_w}\right)$ gives the result as shown by the black lines in Figure 0.8.

By multiplying the outer radius R_o in equation 0.7 with some factor, here represented by k_{pf}, one can simulate how far the pressure disturbance from the well has reached:

$$p_f = p_o + \frac{p_o - p_i}{ln\left(\frac{R_o k_{pf}}{R_w}\right)} ln\left(\frac{r}{R_o k_{pf}}\right) \tag{0.48}$$

Where $R_o k_{pf}$ can be thought of as the radius of pore pressure disturbance. (This equation can easily be used to find the boundary pressure at $r = R_o$ which can be inserted into equation 0.7 in order to use the derived solution). When compared to the numerical solution of the diffusion equation referred to above, it matches reasonably well for dimensionless times of 10 and more in the dimensionless radius range of 1-4, see colored dotted lines in Figure 0.8.

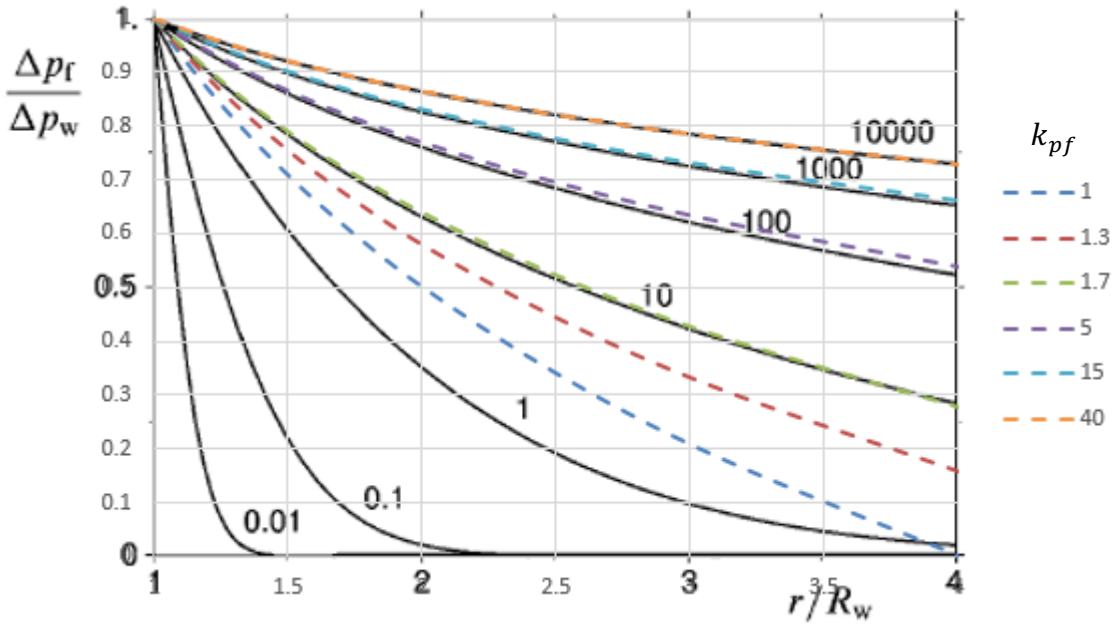

Figure 0.8: Dimensionless change in pore pressure as a function of dimensionless radius and dimensionless time (the numbers above the black curves) (Detournay & Cheng, 1988), compared to equation 0.7 with different radius of disturbance as shown in the legend to the right.

According to (Fjaer, et al., 2008): "For an 8-inch hole, $t' = 1$ corresponds to milliseconds or less for a high-permeable sand, and up to several days for a tight shale." The assumed pore pressure profile in the derived solution can thus be suspected to give a somewhat realistic image of long time pore pressure profiles in downhole shale formations. It can therefore be suspected to give a more precise modelling of a drained hollow cylinder test and also a better representation for certain borehole conditions, especially when used in combination with the diffusion equation. Note that if a mudcake exists $p_f(r = R_w)$ might not always be equal to p_w.

To show the effect of the pore pressure profile on the radial displacement in this model, the dimensionless radial displacement $(u/R_w, in\ \%)$ is plotted versus the dimensionless radius (r/R_w) for three cases with three different (not necessarily realistic) pore pressure profiles. The initial conditions for these calculations are the same as in section 1.6.1 and the inputs are the same as in Table 0.1 except the internal pressure (10 MPa) and the pore pressures (shown in the graphs). The axial pressure is as in the derived solution.

Case 1:

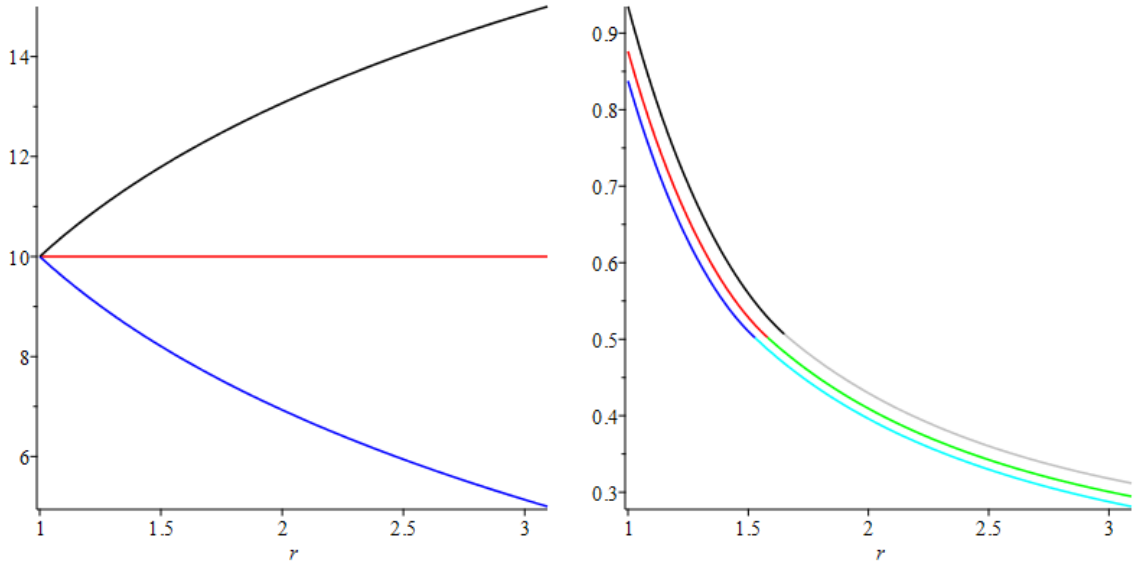

Figure 0.9: Left: Pore pressure profiles in MPa vs. (r/R_w). Right: corresponding dimensionless radial displacement $(u/R_w, in\ \%)$ vs. dimensionless radius (r/R_w). Blue curve on left graph corresponds to blue (and cyan) curve on right graph and so forth. The different colors in the right figure shows the plastic (red, blue, black) and elastic (green, cyan, grey) zones.

The dimensionless radius of the plastic zones (R_p/R_w) for the different pore pressure profiles are:

- Red= 1.580354102
- Blue= 1.528164254
- Black= 1.649842687

Case 2:

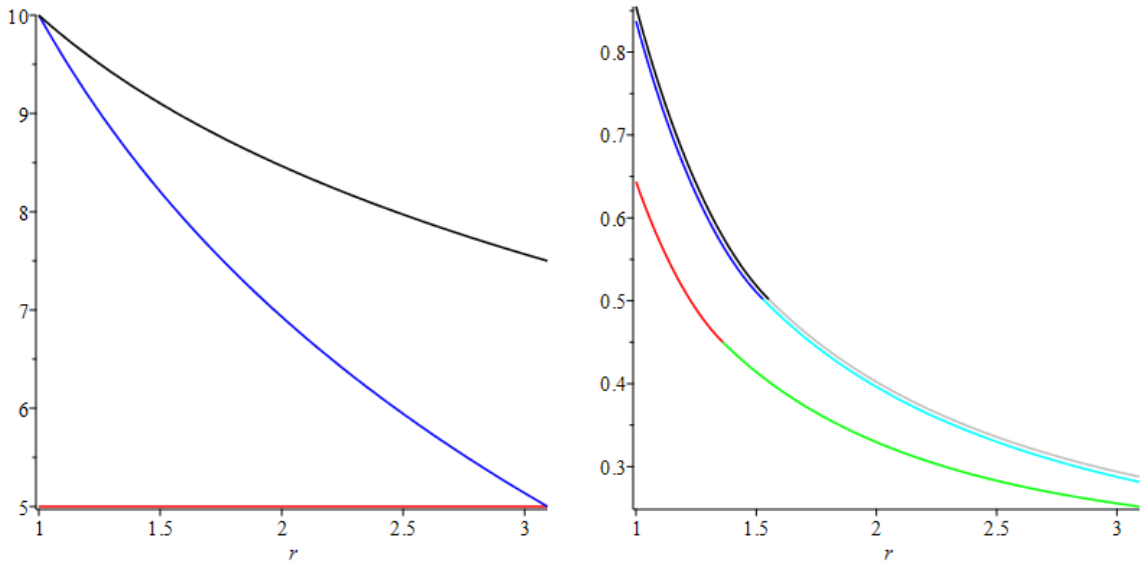

Figure 0.10: Left: Pore pressure profiles in MPa vs. (r/R_w). Right: corresponding dimensionless radial displacement $(u/R_w,\ in\ \%)$ vs. dimensionless radius (r/R_w). Blue curve on left graph corresponds to blue (and cyan) curve on right graph and so forth. The different colors in the right figure shows the plastic (red, blue, black) and elastic (green, cyan, grey) zones.

The dimensionless radius of the plastic zones (R_p/R_w) for the different pore pressure profiles are:

- Red= 1.360772779
- Blue= 1.528164254
- Black= 1.552558673

Case 3:

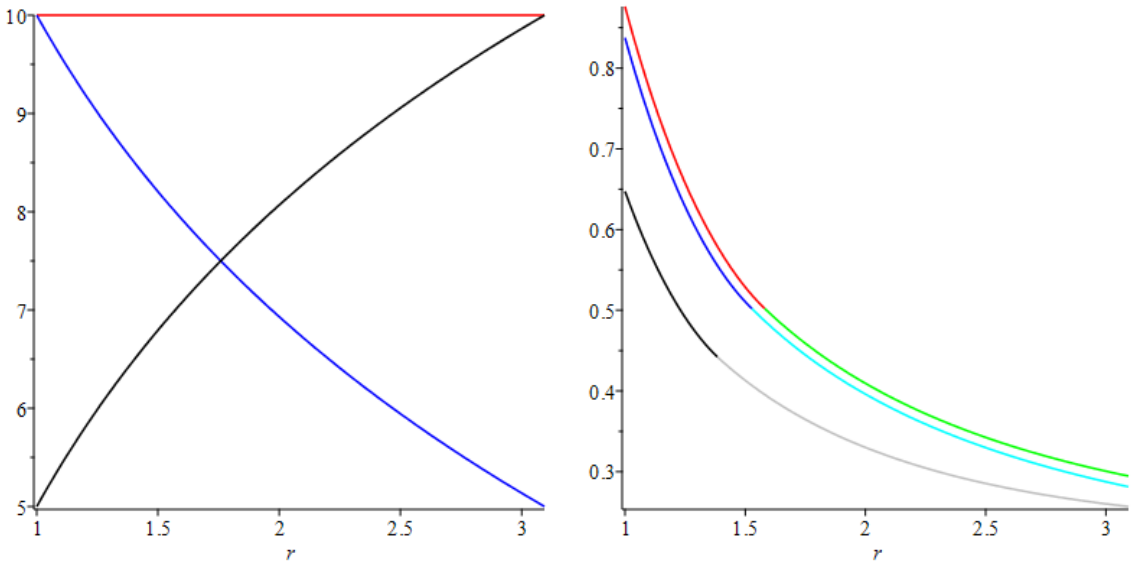

Figure 0.11: Left: Pore pressure profiles in (MPa vs. (r/R_w)). Right: corresponding dimensionless radial displacement $(u/R_w, in\ \%)$ vs. dimensionless radius (r/R_w). Blue curve on left graph corresponds to blue (and cyan) curve on right graph and so forth. The different colors in the right figure shows the plastic (red, blue, black) and elastic (green, cyan, grey) zones.

The dimensionless radius of the plastic zones (R_p/R_w) for the different pore pressure profiles are:

- Red= 1.580354102
- Blue= 1.528164254
- Black= 1.383791759

It is observed that higher pore pressure generally gives more radial displacement and that the effect of increased pore pressure closer to the inner radius has a higher impact on the radial displacement (in the range $r/R_w \leq 3.09375$) than an increase further away, see Figure 0.9, Figure 0.10 and Figure 0.11. The cases demonstrate that pore pressure increase and in particular close to the inner radius will have significant effects on the radial displacement, and that assuming a constant pore pressure for all situations can lead to significant errors. Increased pore pressure will in general bring the rock closer to the failure envelope (see section 0), thus the expected increase plastic zone and radial deformation is captured by the model.

For overbalance ($p_w > p_f$) this model, in combination with the diffusion equation (0.47), could perhaps provide a good approximation of the time-dependent pore pressure effects and their resulting effect on radial displacement (pore pressure in the near wellbore regions adjusting to the well pressure disturbance).

For underbalance ($p_w > p_f$) the largest deformation will be from the initial state, meaning that as pore pressure equilibrates in the near wellbore regions, the model predicts a more stable formation. The lack of tensile cut off in the yield criteria will likely overestimate the stability of the rock for underbalance conditions.

(An attempt to implement an alternative pore pressure profile more accurate for early-times as given in (Nes & Fjær, 2015) was made, but an analytical solution for plastic stresses could not be obtained. In order to keep the model mostly analytical the form of the pore pressure profile must remain relatively simple.)

1.6.4 Residual Strength and Flow Rule (Angle of Dilatancy)

An important parameter to analyze is the plastic cohesion c_p, governing the residual strength (C_0^p). The effect of this parameter is not easily seen from the equations for radial displacement, as it affects the stresses and radius of the plastic zone. Below in Figure 0.12 the dimensionless radial displacement for three different values of plastic cohesion is shown. The inputs and initial conditions (with the exception of plastic cohesion) are given in Table 0.1.

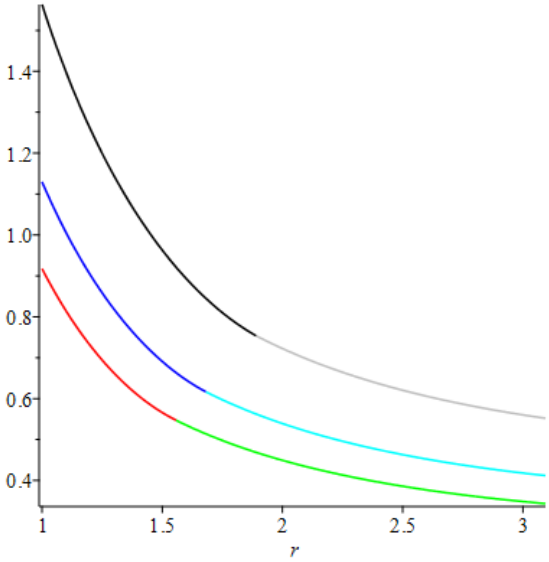

Figure 0.12: Dimensionless radial displacement (u/R_w, in %) vs. dimensionless radius (r/R_w) for residual cohesion of 100% (red and green) , 75% (blue and cyan) and 50% (black and grey) of the elastic cohesion

The dimensionless radius of the plastic zones (R_p/R_w) for the different plastic cohesions are:

- Red= 1.55706253
- Blue= 1.680746012
- Black= 1.890368973

The plastic cohesion has significant impact on the radial displacement (at least in the range of $r/R_w \leq 3.09375$). Furthermore from Figure 0.12 (and other calculations not shown here) it is observed that the relationship between reduced plastic cohesion and increased strain is not linear or simple. In addition, the effect (although significant for all r's in this case) is gradually decreasing the further away from the inner radius one is.

Following the discussion in section 0 the effects of the dilatancy angle and associated vs. non-associated flow rules can clearly be seen in Figure 0.13 The inputs and initial conditions (with the exception of dilatancy angle) are given in Table 0.1.

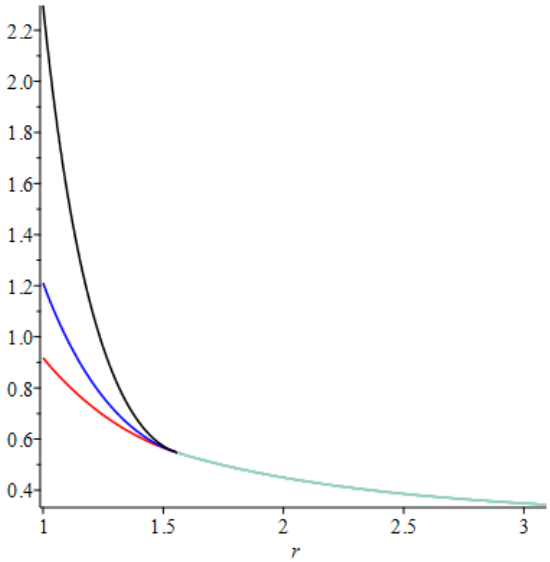

Figure 0.13: Dimensionless radial displacement $(u/R_w,\ in\ \%)$ vs. dimensionless radius (r/R_w) for dilatancy angles of 0° (red), 50% of ϕ (blue) and 100% of ϕ (black, associated flow rule)

The dimensionless radius of the plastic zones (R_p/R_w) for the different dilatancy angles are all the same (1.55706253) as the dilatancy angle only affects the plastic zone. While high values for the angle of dilatancy might not be usually encountered in practice, it is useful to illustrate the potential effect of dilatancy angles on radial displacement.

1.6.5 Stress Distribution

A consequence of reducing the cohesion in the plastic zone is a discontinuity in the tangential and axial stress at the elastic-plastic interface (see Figure 0.14) as the failure criteria corresponding to peak strength (equation 0.1) and post peak strength (equation 0.6) must both be maintained at the elastic-plastic interface. This can be avoided by using either RDM or dilatancy angle.

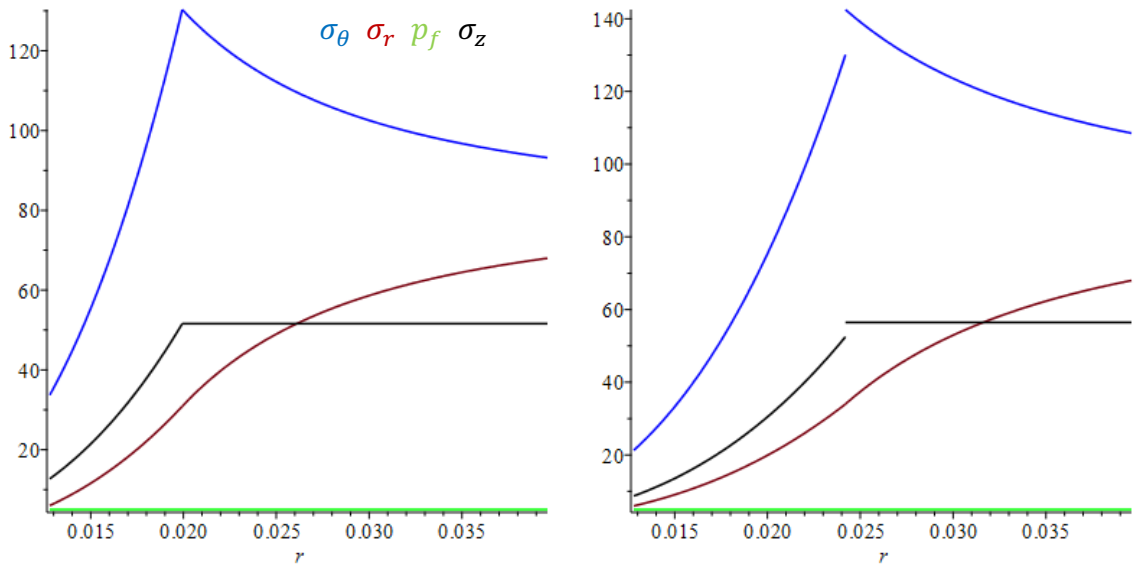

Figure 0.14: The effect of a plastic cohesion on stresses. Left graph $c_p = c$, right graph $c_p = 0.5c$, rest of the inputs are given in Table 0.1

1.6.6 Plastic vs Elastic Deformation Contribution

Following the discussion in section 1.4 it is of interest to investigate the difference in plastic and elastic contribution to radial displacement. The elastic and plastic contribution to the dimensionless radial displacement is shown for two cases below in Figure 0.15 the inputs (except plastic cohesion) is given by Table 0.1. The plastic contribution to the radial displacement is dominant for the inner parts of the plastic zone (in fact the elastic contribution is negative here, i.e. borehole expanding) but gradually decreases, and in the region close to the elastic-plastic interface the elastic deformation overtakes the majority of the contribution to radial displacement. When the residual strength is equal to the strength in the elastic zone the plastic contribution to the radial displacement will be zero at the elastic-plastic interface as there will be continuity in the stresses. Whereas the discontinuity in stresses when using a lower residual strength causes the plastic contribution to be non-zero, see Figure 0.15.

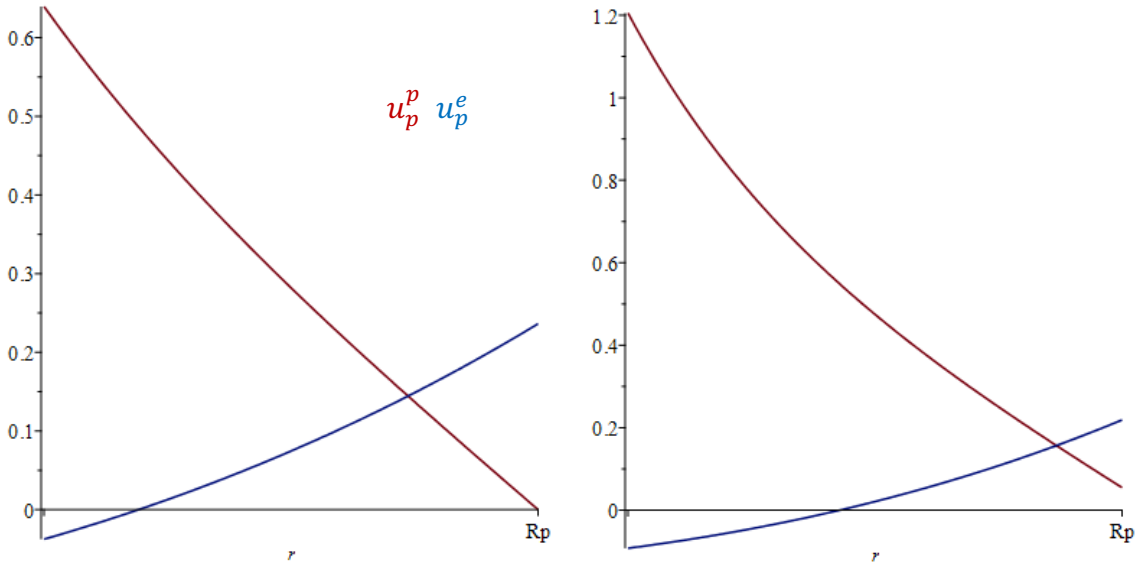

Figure 0.15: Dimensionless radial displacement $(u/R_w,\ in\ \%)$ vs. dimensionless radius(r/R_w). Left graph $c_p = c$, right graph $c_p = 0.5c$, rest of the inputs are given in Table 0.1

1.6.7 Important Sources of Error

Semi Analytical

The solution derived above is a semi-analytical solution as the plastic radius R_p is found numerically.

Ideal Behavior

The elastic-brittle-plastic model assumes ideal elasticity followed by an instant softening process and ideal plasticity. The ideal behavior does not give a truly realistic image of strain vs. stress as it does not take into account how strain changes the yield criterion. More realistic models will have to incorporate how the strain affects the yield criterion (hardening/softening) and must necessarily become much more complex mathematically. Numerical models should be used for more precise predictions/calculations, but the semi-analytical solution may be used for a quick overview.

Yield Criterion

It is known that the Mohr-Coulomb (MC) criterion does not give a very precise prediction of tensile and compressive yield. According to the MC criterion the compressive strength increases monotonically with the lateral confining stress. Observations shows that this is not the case, especially for sedimentary rocks where grain crushing will occur, as a consequence the real shape of the yield criterion usually curves down. The MC criterion also tends to overestimate the tensile strength of the rock. Furthermore, experience shows that the intermediate principal stress plays a role in the failure of rocks (see for example (Chen, et al.,

2000)), although small compared to the maximum and minimum principal stresses it can for many cases be considered significant. Criterions such as Von Mises, Hoek-Brown and unified strength theory are examples that takes this into account. The MC is however very convenient for keeping it mathematically simple and works reasonably well for many borehole cases.

Axial Stress

As explained, the axial stress is not always the intermediate principal stress.

Sealing Capacity

The model does not evaluate the rocks sealing capacity and how it potentially changes through strain, the effects on pore pressure from rock dilation and other strain is also not incorporated.

Porosity, Temperature and Anisotropy

The solution does not directly evaluate the effect of for example rock porosity and temperature, but these effects could to a certain degree be compensated by the material parameters. Furthermore, it does not consider anisotropy effects neither in stress regime or rock properties, which is shown to have big effects on deformation, this will be seen in section 0.

1.7 Concluding Comments

The following semi-analytical solution for radial displacement for a hollow cylinder subjected to boundary conditions is similar to previous solutions (Chen, et al., 1999) (Zhang, et al., 2012), but with an improved way to model pore pressure effects. This is advantageous for tests done under drained conditions and/or certain borehole conditions where a non-constant pore pressure profile can be expected.

For overbalance ($p_w > p_f$) conditions this model, in combination with the diffusion equation (0.47), could perhaps provide a good approximation of the time-dependent pore pressure effects and their resulting effect on radial displacement (pore pressure in the near wellbore regions adjusting to the well pressure disturbance). For underbalance ($p_w > p_f$) the largest deformation will be from the initial state, meaning that as pore pressure equilibrates in the near wellbore regions, the model predicts a more stable formation. The lack of tensile cut off in the yield criterion will most likely overestimate the formation strength in under balanced cases and therefore the results should be critically evaluated.

A comparison to a collapse test suggests that it can provide a good approximation for certain cases, but it remains to be properly compared to a test under drained conditions.

The model was made by Kun Su, while the derivation was conducted by the author. With the equations from the author the solution can easily be implemented and used in other software than Maple (which has proved to be unstable). The addition of potential improvements (changing axial stress, and including RDM model) has been discussed and analyzed.

The solution is based upon many more or less realistic assumptions and should only be used to give an idea of an expected result. For more accurate results, more complicated numerical models should be used.

Literature Review on Creep Tests for Shale and Clay

Based on high quality formation barriers formed in more than 40 wells in the North Sea, creep is suspected to be the primary displacement mechanism (Williams, et al., 2009). While the contribution of other mechanisms is debatable, it appears commonly accepted in the industry that creep has a key involvement. Creep tests on shale samples is not an excessive literature, and in particular not for hollow cylinder samples, which are most relevant for the barrier problem.

This section will discuss some of the creep tests carried out by underground nuclear waste projects where creep has been more extensively studied. While this is for shallower onshore clay-rich rocks and not shales per se, they share many properties and it is reasonable to assume much of the same behavior can apply for downhole shale formations. Besides, the exact transition/difference between clay and other argillaceous rocks to shale is not entirely clear, both rock types contain a high amount of clay minerals (>40% (Fjaer, et al., 2008)) and clays and argillaceous rocks tend to develop the typical fissile and layered structure of shales under deeper burial. In the end, with the help of these geomechanical tests (and more) the creeping capacity of the relevant P&A formation will be evaluated.

1.8 What is Creep

In short, creep is a time dependent slow deformation of a solid material under constant loads lower than the materials failure strength. It comes from visco-elastic effects in the framework of the material and creep deformation is mostly plastic. The time scale of creep can last from few minutes to many years. Typically creep is divided into three stages, see Figure 0.1 (Fjaer, et al., 2008) (Hosford, 2005):

1. Primary creep: Transient elastic deformation with decreasing strain rate
2. Secondary creep: Plastic deformation with constant strain rate
3. Tertiary creep: Plastic deformation with accelerating strain rate.

Unless the stresses are reduced, tertiary creep eventually leads to brittle failure. Stress arching effects or support from the casing can provide such stress relief in a borehole, potentially lowering the stress state below the creep threshold (Fjaer, et al., 2016).

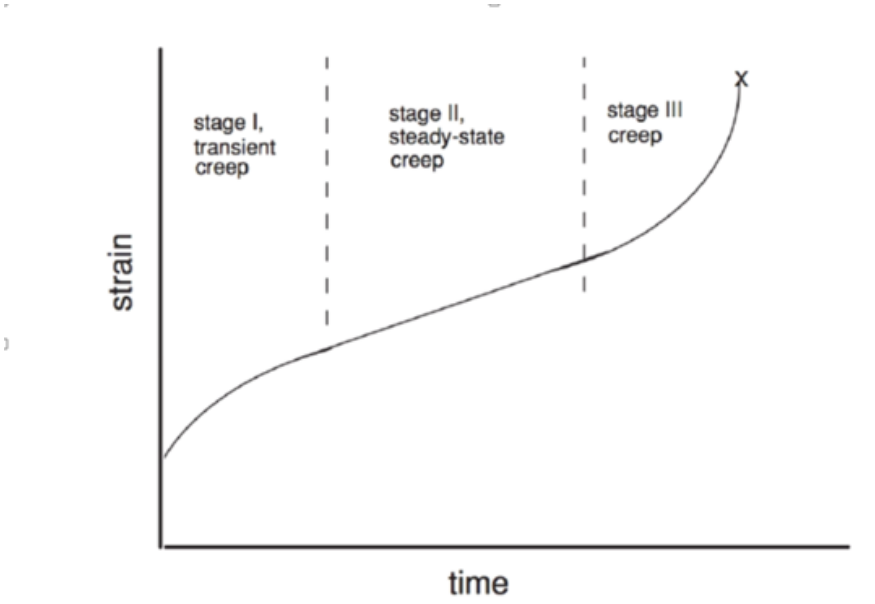

Figure 0.1: The three different creep stages illustrated on a strain vs time plot (Hosford, 2005)

1.9 Creep Tests

Creep tests are rock mechanical tests carried out in order to measure a rocks ability to deform and redistribute stresses when subjected to constant deviatoric loads, temperatures and (potentially) chemical conditions over long time intervals. The duration of such tests is typically in the range of several weeks or months and the deformations are usually measured in axial and radial strains. For the following section it can is useful state the difference between drained and undrained conditions:

- Drained conditions mean that the fluid is allowed to enter or leave the sample. This means that the pore pressure can be controlled by controlling the surrounding pressure.
- Undrained conditions mean that no fluid is allowed to leave or enter the sample. Changing surrounding pressures will result in a change of pore pressure as it is not allowed to equilibrate.

1.10 Callovo-Oxfordian Argillite and Opalinus Clay from Mont Terri

Both rocks are consolidated sedimentary rocks where the rough composition of the Callovo-Oxfordian Argillite is given in section 1.10.1 and the Opalinus Clay in section 1.10.2. The rocks are compact and relatively homogenous with less significant bedding planes than what is typically found in overburden shales. This is especially true for the Argillite (also known as mudstone) which consists mostly of indurated clay particles. Both rocks grades into shale when layered fissile structure develops (typically occurs at deeper burial). Evaluation of the deformation abilities for these stiff clayrocks can perhaps be relevant for consolidated deeper

shales and it is worth noting that the Opalinus Clay does not appear very different to some North Sea overburden shales.

1.10.1 Experimental Study of the Hydro-Mechanical Behavior of the Callovo-Oxfordian Argillite (Zhang & Rothfuchs, 2004)

Material Characteristics

Creep tests on cylindrical core samples taken from various depths (434-506 meters) in the Callovo-Oxfordian argillaceous formation were performed to evaluate suitability for radioactive waste disposal. The composition is roughly 40-45% clay minerals, 20-30% carbonates and 20-30% quartz (Lebon & Ghoreychi, 2000) (Hoteit, et al., 2000). The samples were largely homogeneous with small variations of physical properties, summarized below in Table 1:

Average properties	
Bulk density [g/cm^3]	2.41 $\pm$ 0.03
Dry density [g/cm^3]	2.25 $\pm$ 0.05
Grain density [g/cm^3]	2.7
Water content [%]	7.7 $\pm$ 1.27
Porosity [%]	16.8 $\pm$ 2.0

Table 1: Average Physical properties of the samples tested (Zhang & Rothfuchs, 2004)

Uniaxial compression tests shows saturated samples failing at 24.5 MPa with 1 % axial strain and unsaturated samples at 41.7 MPa and 1.9 % axial strain. A typical result for undrained multistage triaxial compression tests on samples (d/l=50/98 mm) perpendicular to the bedding planes is shown below in Figure 0.2. Results shows onset of dilatancy before failure and the normal trend of increased strength (peak and residual) with increased confining pressure.

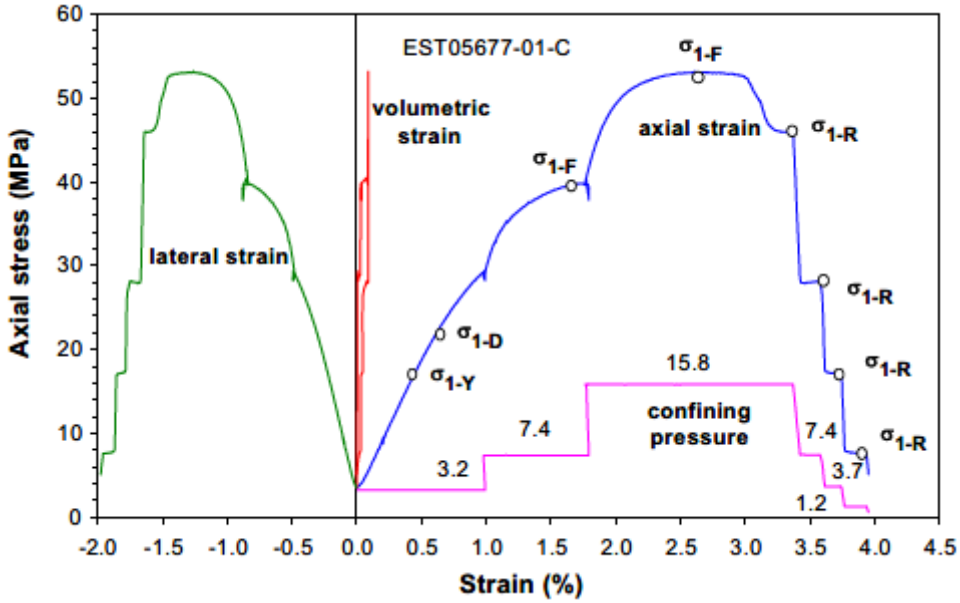

Figure 0.2: Typical result from multistage triaxial compression test, where σ_{1-Y} is yield stress, σ_{1-D} onset of dilatancy, σ_{1-F} peak failure and σ_{1-R} residual strength. (Zhang & Rothfuchs, 2004)

Heterogeneous Elastic Behavior, Homogeneous Creep Behavior

During creep tests all the samples (six big *d/l* = 100/200 mm, five small *d/l* = 45/90 mm) were sealed with rubber jackets and steel platelets to prevent water loss i.e. undrained conditions. Axial loads (2-15 MPa) are applied stepwise and lasts from 1-7 months, between each step is an unloading in order to measure plastic and elastic deformation. Creep is observed for relatively low deviatoric stresses (2 MPa) (deviatoric stress is in this case the difference between confining and axial stress), suggesting a practically insignificant threshold for creep (the authors (Zhang & Rothfuchs, 2004) suggests no threshold). Samples taken from deeper intervals shows expected trends of smaller instantaneous strain (elastic deformation). However creep rates appears to be unaffected by depth, which is contradicting the normal trend, see Figure 0.3.

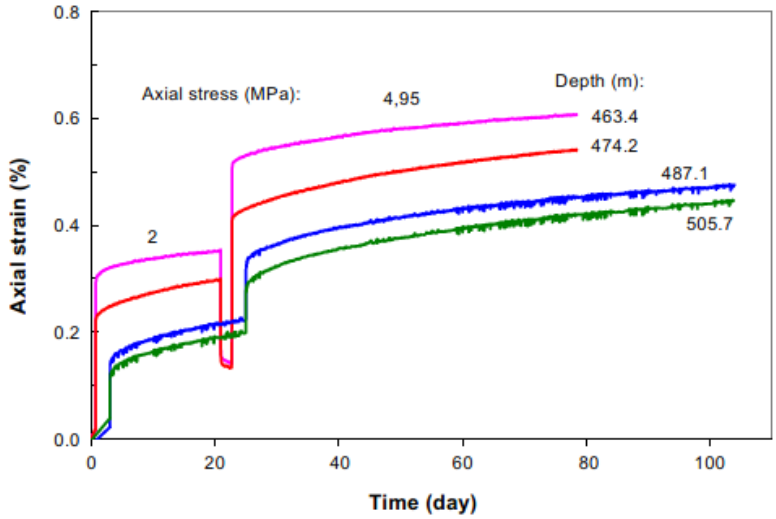

Figure 0.3: Strain rates for samples taken from different depths (Zhang & Rothfuchs, 2004)

Scaling effects are observed for total strain (higher total strain for larger samples), but the creep contribution to the total strain appears similar, see Figure 0.4. So for this case it appears that scaling effects should be considered for elastic effects (Young's modulus was independent of saturation degree and typically 2-2.5 times larger for small samples), but seems negligible for creep effects.

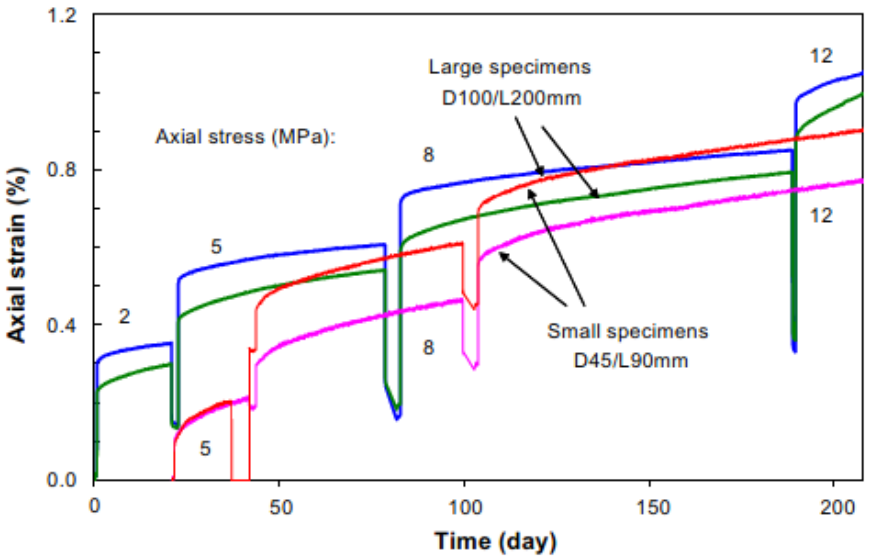

Figure 0.4: Scaling effects for elastic and creep deformation/strain (Zhang & Rothfuchs, 2004)

Larger axial strain is observed for samples loaded perpendicular to the bedding planes than for samples loaded parallel (Young's modulus was ~1.5 times larger in the direction parallel to the bedding planes). However once again creep rate seems fairly independent. The heterogeneity of the elastic properties follows expected trends, but the homogeneity of creep effects is a bit of a curious result (this also appeared puzzling for the authors (Zhang & Rothfuchs, 2004)).

Effect of Pore Water

At the loading step of 15 MPa two samples were allowed to desaturate (drained conditions) by opening them to the surrounding air, the result was an immediate increase in axial strain, but no observation of creep was observed after desaturation. Thus pore water appears to be essential for creep in this clay.

Follows conventional creep stages

The conception of creep consisting of three stages, fits well with the results as be seen by the initial strain rate gradually decreasing (transient stage) and then stabilizing at a more or less constant rate (quasi-steady rate) as predicted by the secondary creep stage (steady-state). When plotted the quasi-steady creep rates has a rather linear relationship with the applied stress, disregarding effects from anisotropy, see Figure 0.5. (The authors note however, that it should be taken into account that sufficient time to reach steady-state might not have been given (Zhang & Rothfuchs, 2004).)

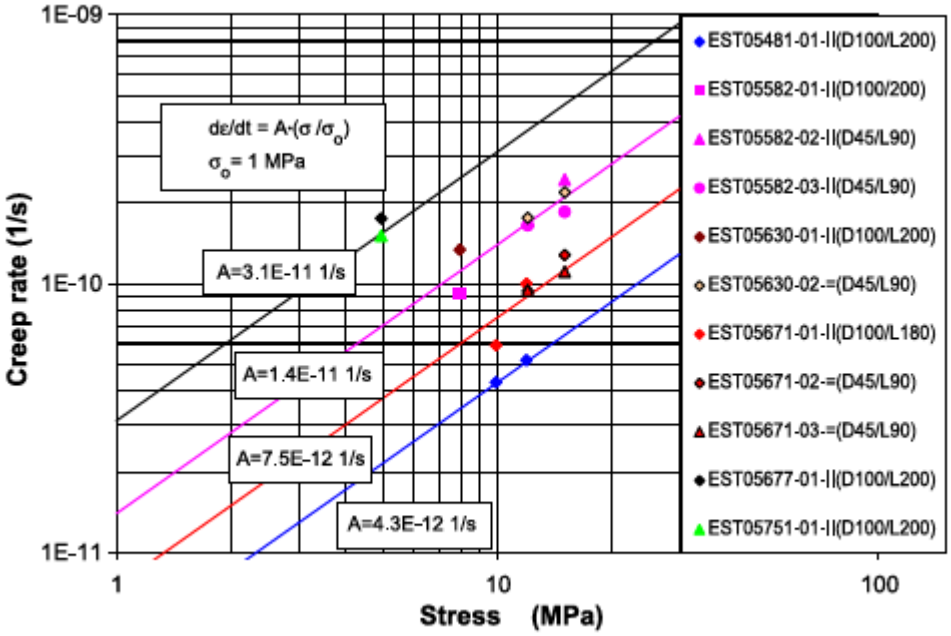

Figure 0.5: Graph showing the quasi-steady creep rate vs the stress applied (Zhang & Rothfuchs, 2004)

1.10.2 Experimental Study of the Thermo-Hydro-Mechanical Behavior of Indurated Clays (Zhang, et al., 2007)

Material Characteristics

This study investigated the so-called "thermo-hydro-mechanical" behavior of the Callovo-Oxfordian Argillite at Bure and the Opalinus Clay at Mont Terri. The study includes a remarkably long creep test lasting over two years. The composition of the Callovo-Oxfordian Argillite is given in the previous section and the Opalinus Clay consists of 45-76 % clay minerals, 6-30 % quartz, 6-39 % calcite and 2-4 % of feldspars (Pearson, et al., 2003). The samples are assumed completely water-saturated in situ, but some saturation loss occurred before testing. Some key petrophysical properties are given below in Figure 0.6.

Average property	Callovo-Oxfordian argillite Bure	Opalinus clay Mont Terri
Grain density (g/cm^3)	2.70	2.71
Dry density (g/cm^3)	2.25	2.31
Bulk density (g/cm^3)	2.41	2.46
Porosity (%)	16.8	15.1
Water content (%)	7.7	6.7

Figure 0.6: Petrophysical properties of the investigated rocks (Zhang, et al., 2007)

Effects of Pore and Interstitial Water

Two tests to determine swelling and shrinking effects of the clays were carried out, one where the sample had a constant axial load and another where the sample was axially fixed, both tests with laterally unconstrained conditions. The saturation was changed by injecting gas with varying humidity. In the constant load test the sample swelled during hydration and shrank during dehydration showing that the deformation of such rocks depends on the water uptake and release, it is also worth noting that these effects appear to be somewhat reversible, see Figure 0.8. The test measuring stress while axially fixed, shows swelling pressure as a function of saturation, as expected the stress increases during hydration and decreases during dehydration, see Figure 0.7.

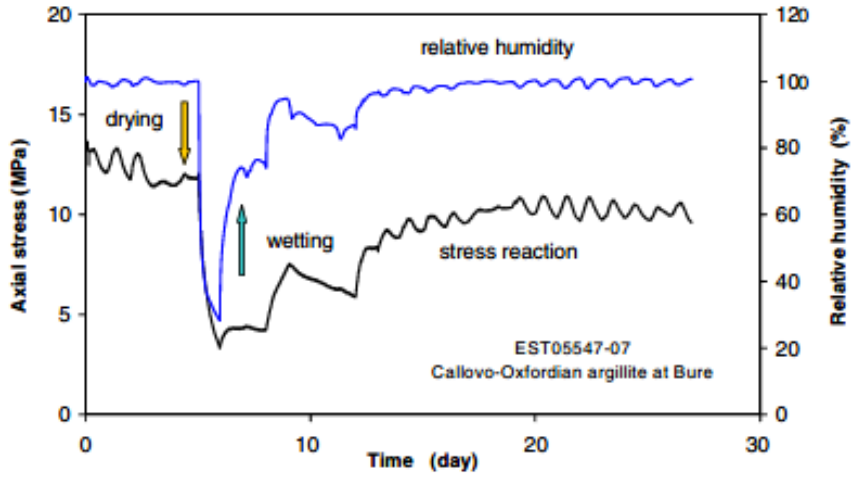

Figure 0.7: Axially fixed, laterally unconstrained Collovo-Oxfordian Argillite sample exposed to changes in air humidity and observed stress responses (swelling pressure) (Zhang, et al., 2007).

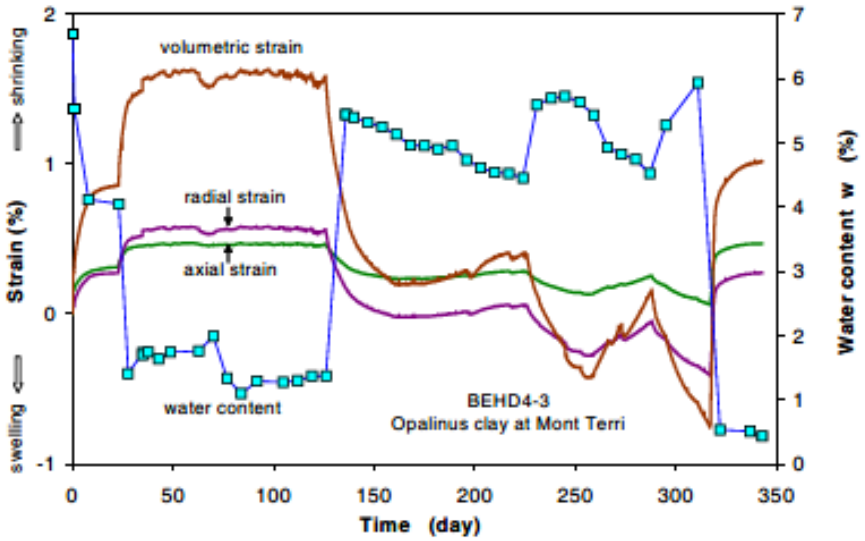

Figure 0.8: Constant axially loaded, laterally unconstrained Opalinus Clay sample exposed to changes in air humidity and observed strain responses (swelling and shrinking) (Zhang, et al., 2007).

Triaxial compression tests with different saturation conditions on the Opalinus Clay (see Figure 0.9), shows some of the correlations between water (both free pore water and interparticle water films) and deformation. An initially (83%) saturated sample was isotropically loaded (5 MPa) under drained conditions, which resulted in compaction (1.03%), then re-saturated from one side (inlet pressure 4 MPa) while other communication channels were kept closed (outlet) which expanded the sample (1.05%), when saturated from outlet channel too (4 MPa) the expansion increased (0.7%), see Figure 0.9. The tests shows that the water affects the deformation through not only consolidation effects (pore pressure equalization). In the undrained load step the pore pressure increases, thus reducing the effective stresses and also the resulting deformation. The water clearly has a load bearing capacity in this case, illustrated well

by the high measurement of Skempton's B-coefficient. It was estimated to be around 0.9 (based on the undrained load step) and can be interpreted as the fraction of an extra load carried by the pore fluid, expressed mathematically as $B = \frac{\Delta p_w}{\Delta \sigma}$, where $B = 1$ means the entire change in load is carried by the pore fluid. This indicates that the interparticle water films are stress supporting, and potentially might be able to carry the entire lithostatic stress. In the last step, the sample is allowed to drain which as expected results in a compaction due to the large effective pressure.

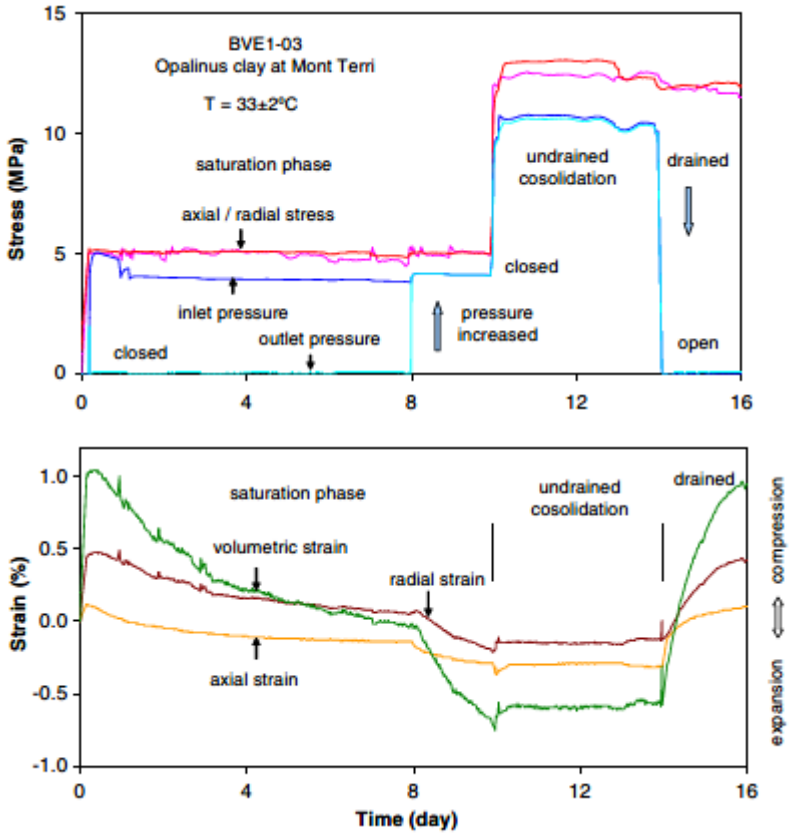

Figure 0.9: Triaxial compaction test with varying saturation, showing pore water effects on strain/deformation on an Opalinus Clay sample (Zhang, et al., 2007).

Effects of Temperature on Creep

An expansion test under constant loads with stepwise changes in temperature on an Opalinus Clay sample, shows that an increase in temperature leads to a rapid expansion in the direction perpendicular to the bedding planes and a much smaller expansion in the radial direction. The expansion was followed by a compaction as a function of time, most likely due to pore water drainage according to the authors (Zhang, et al., 2007), in other words not 100% undrained conditions, see Figure 0.10 a and b. Dropping the temperature gives rapid contraction in the direction perpendicular to the bedding planes and expansion in the direction parallel to the bedding planes. The results gives strain rates an order of magnitude higher in the direction

perpendicular to the planes compared to parallel, in other words the Opalinus Clay appears highly anisotropy when it comes to thermal effects, see Figure 0.10 c.

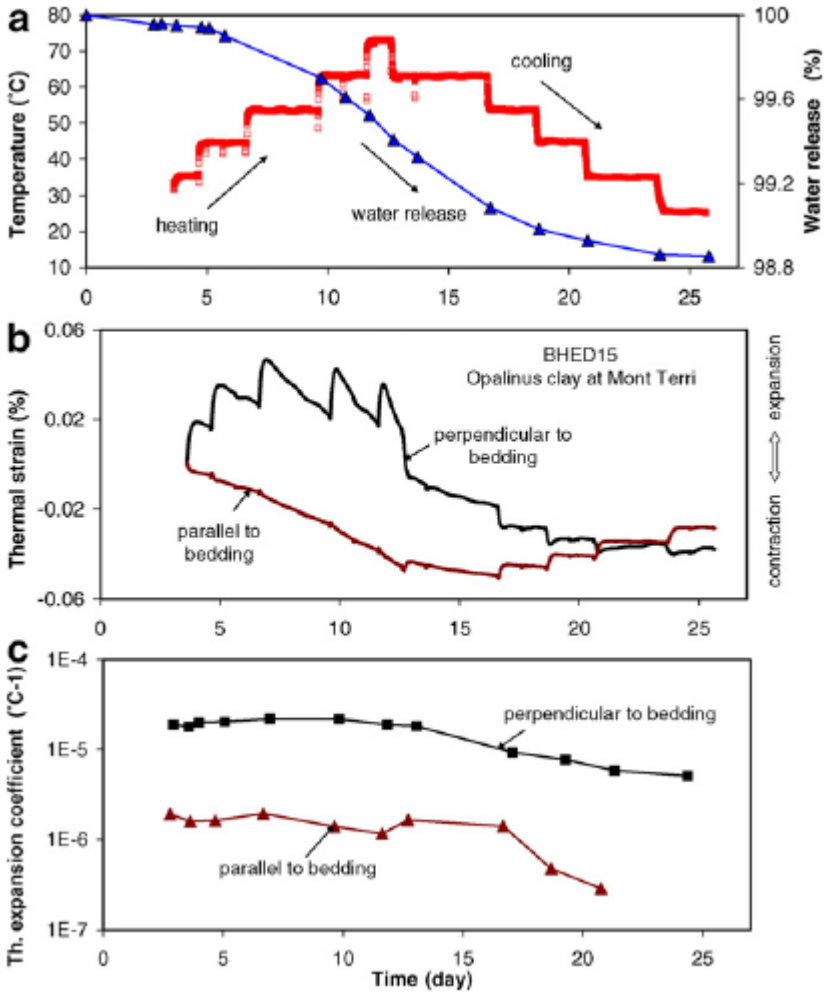

Figure 0.10: Thermal expansion test results (a) temperature steps and water release vs time (b) total strain vs time (c) strain rates vs time (Zhang, et al., 2007).

Increasing temperature leads to an increase in pore pressure due to the difference in the thermal expansion between the pore fluid and the solid particles. Furthermore, because of the low permeability in this case the pore water is not allowed to distribute adequately and therefore might induce local overpressured zones, explaining why also under drained increased temperature showed an increase in pore pressure and expansion (for short time, followed by gradual compaction as pore fluid leaves the sample).

Uniaxial creep tests with constant load, undrained conditions and stepwise change in temperature with duration of about two years was carried out. In short, the exceptionally long creep tests show that a threshold for creep is practically non-existent for the Argillite in the tested temperature range, as significant creep is observed for stresses down to 0.7 MPa, see Figure 0.11. For each temperature increase an initial expansion for a short time, is proceeded

by creep at an increased rate. (Except for temperatures above 50 °C, possibly due to the leakage the authors indicated). Cooling results in sudden compaction, but no creep effects even after months. It is also worth noting that in the last temperature step (from 40-60 °C) the sample under 14 MPa load behaves different compared to the lower stressed ones (it responds by further compaction and then stops creeping). Figure 0.11 displays the results graphically.

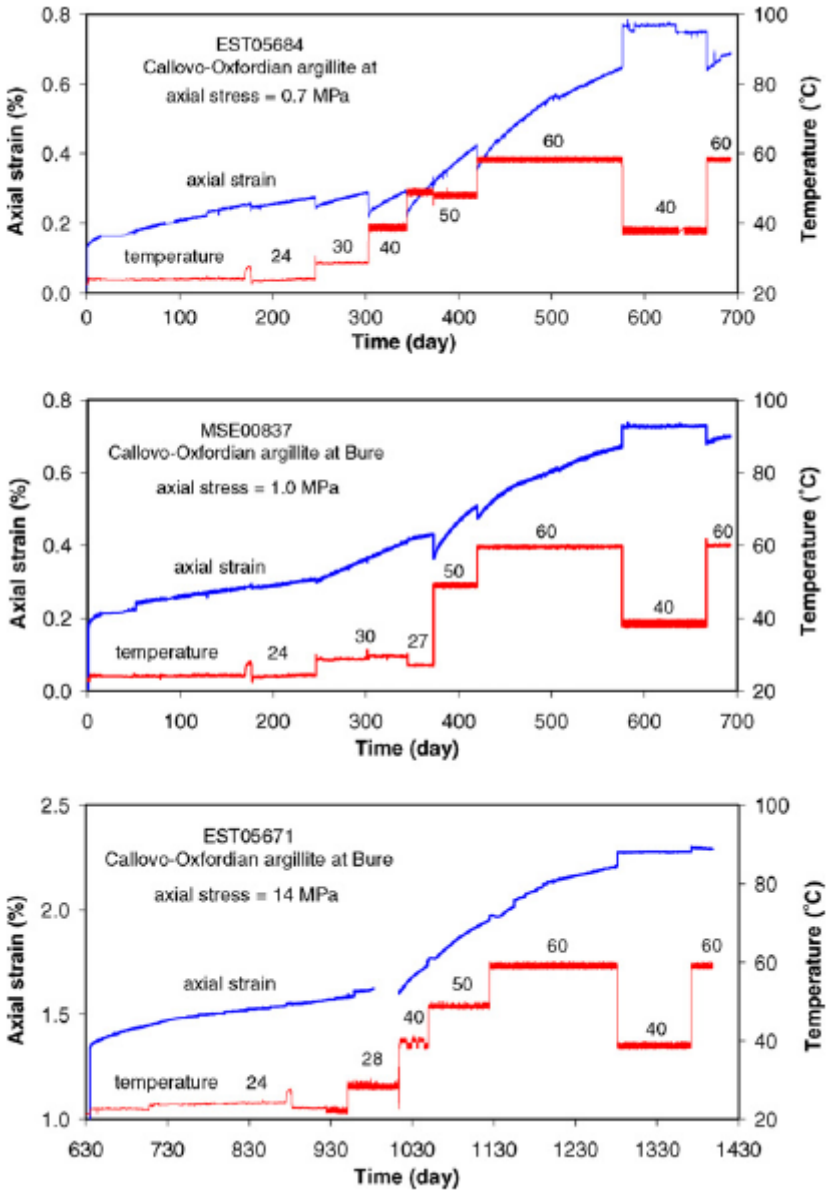

Figure 0.11: Temperature effects on creep for Callove-Oxfordian Argillite samples for different loads (Zhang, et al., 2007).

The authors suggests decreased water viscosity and in turn decreased shear resistance between particles containing clay bound water as the mechanism that increases creep rate. In addition pore water release due to thermally-induced evaporation could cause shrinkage (technically not a creep-mechanism). This desaturation might also cause increased shear resistance as fluid is removed, and thus reduce creep.

Effects of Temperature on Strength

Triaxial tests with different temperatures were performed on the Opalinus Clay. The sample was brought to failure with a constant strain rate under undrained conditions and constant lateral stress. The samples exhibited typical elasto-plastic behavior as they became significantly weaker (failure at lower deviatoric stress) and more ductile at elevated temperatures, see Figure 0.12. Onset of dilatant behavior is observed and it continues until brittle failure of the sample (i.e. when the rock sample loses its load bearing capacity), see Figure 0.12. This loss of strength can be linked to the overpressure in pores created by the elevated thermal expansion effects, in fact the pore pressure could eventually exceed the lateral pressure and create tension failure (rocks usually have low tensile strength).

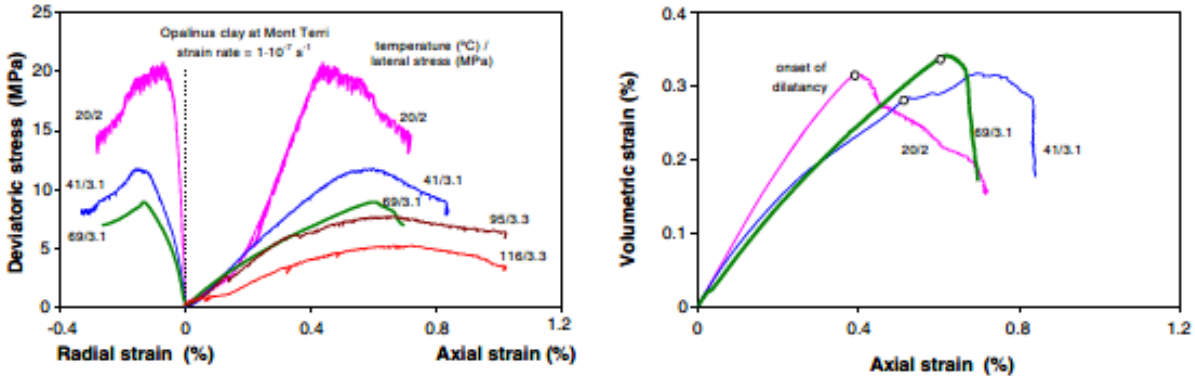

Figure 0.12: Triaxial strength tests with different temperatures (Zhang, et al., 2007).

Self-healing Abilities

Finally, another experiment showcased the characteristic ability indurated clays have of healing itself, or more precisely, self-mitigation of pre-existing or creep induced fractures. Two failed samples of Callovo-Oxfordian Argillite were tested by injecting gas with 50% relative humidity under constant pressure conditions. The results show that the permeability of the samples decreases significantly over the course of two months, see Figure 0.13. The explanation is probably linked to the swelling and creeping capabilities of the samples, and possibly also chemical reactions.

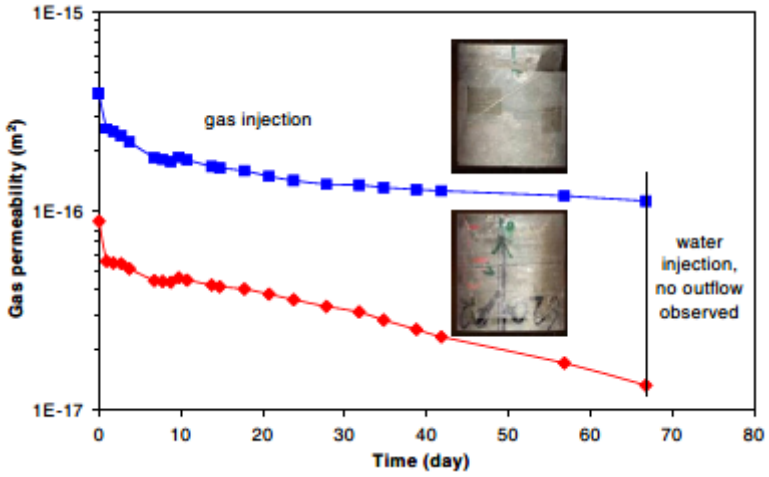

Figure 0.13: The reduction of gas permeability as a function of time. This effect demonstrates the self-healing abilities of the Callovo-Oxfordian argillaceous samples (Zhang, et al., 2007).

1.10.3 Anisotropy Effects on Dilatancy, Strength and Creep

The Opalinus Clay and its deformation was also investigated by (Naumann, et al., 2007) with triaxial compression tests. It was observed a clear anisotropic behavior, in strength, dilatancy and creep between samples loaded parallel and samples loaded perpendicular to the bedding planes. Lower strength was observed when the samples were loaded perpendicular to the bedding planes but onset of dilatancy almost coincided with failure, and was much more distinct when loaded parallel. Larger axial strain rates are observed for samples loaded perpendicular to the bedding planes, this was more pronounced in the transient than in steady-state stage.

1.11 Boom Clay Experiments

The Boom Clay has been researched during more than 30 years, with both in situ and laboratory experiments. It is a water saturated clay formation at 190-290 meters depth found in Belgium, and can be described as rather plastic and homogenous. More precisely it is qualitatively homogenous laterally with some heterogeneity vertically related to grain-size distribution (silt or clay-dominated intervals). Depending on where the samples are retrieved from the weight percentage of non-clay minerals (mainly silicates) vary from 27-77wt% and for clay minerals 25-71wt%. The clay minerals mainly consist of pure smectite and illite and interstratified layers of smectite and illite or kaolinite (You, et al., 2010) (Zeelmaekers, et al., 2015) (Li, et al., 2009). The Boom Clay represents is a less consolidated clayrock and while it is perhaps not similar to typical rocks (some similarities to deep clays in Hordaland group) found in the North Sea the extensive studies (also on hollow cylinders) are useful for understanding the mechanisms behind creep.

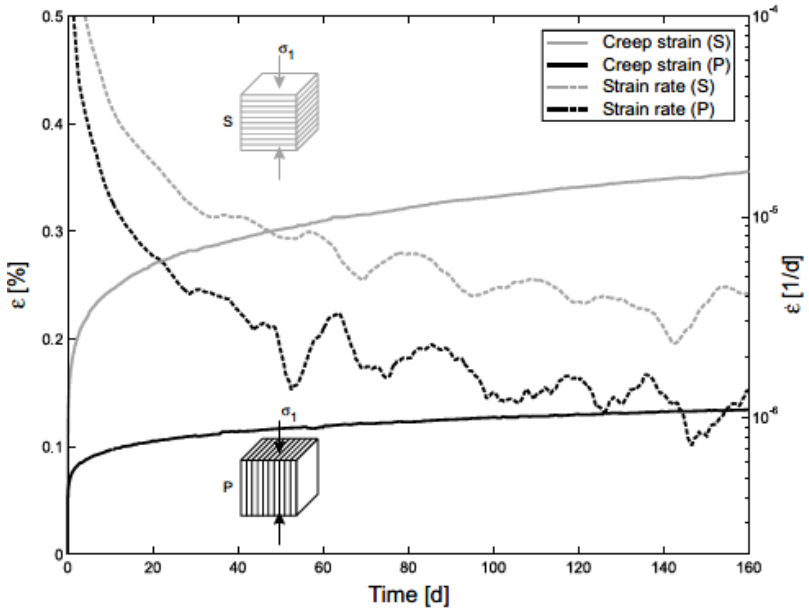

Figure 0.14: Deformation behavior of samples loaded parallel (P) or normal (S) to the bedding planes under constant applied stresses (r3= 12 MPa, Dr = 13 MPa, T = 30 °C, cylindrical samples). (Naumann, et al., 2007)

1.11.1 Time-dependent behavior of rocks: Laboratory tests on hollow cylinder (Rousset, et al., 1989)

Belgium Boom Clay cores extracted from around 250 meters depth underwent creep tests all the way back in 1989. The tests were conducted on hollow cylinder samples, an advantageous geometry that better represents in situ conditions of a borehole. Properties of the samples are shown below in Figure 0.15. (The short term undrained cohesion of the Boom Clay was 1 MPa, in addition there existed a long term cohesion which may be used in order to interpret long term stability).

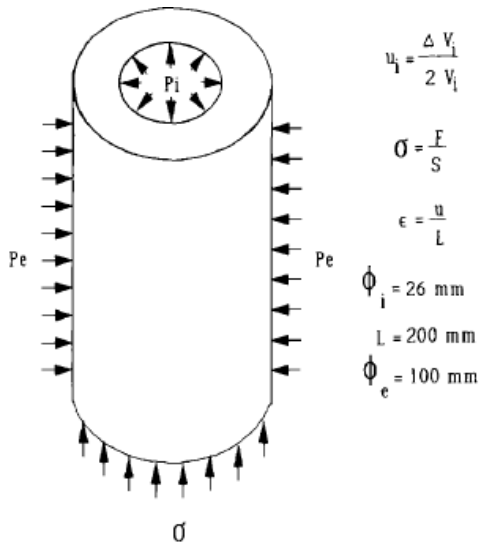

Figure 0.15: Sample dimensions and definitions of different parameters (Rousset, et al., 1989)

The experimental procedure consisted of loading the core isotropically to 5 MPa, followed by stepwise reduction in the internal pressure. For each pressure reduction step the conditions are kept constant and the volumetric change of the internal volume is measured. When the internal volume is stabilized the internal pressure is reduced further and the process repeated. The time for each loading step varied from hours to a couple of days.

The results indicates that time dependent effects are dominant as the immediate convergence per loading step only represented ~10% of the ultimate deformation. The Boom Clay demonstrates non-linear behavior as the convergence and time for stabilization increases when the difference between external and internal pressure increases, see Figure 0.16. All samples failed at around 8% deformation with sliding surfaces from inner to the outer wall. When tests were stopped before failure occurred, the samples maintained a relatively perfect hollow cylinder shape with a diameter smaller than the original one, suggesting that eventual strain localization observed is likely due to brittle failure mechanisms.

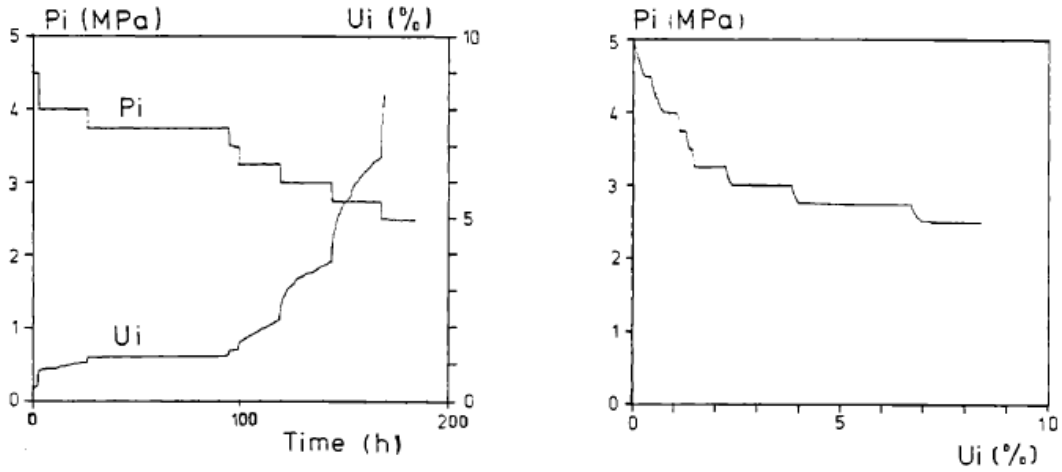

Figure 0.16: The graphs show the internal volumetric strain vs internal pressure and on the left graph time is also included. (Rousset, et al., 1989).

1.11.2 Medium resolution X-Ray computed tomography of hollow cylindrical samples of Boom Clay (You, et al., 2010)

Thick-walled hollow cylinder samples (OD=86 mm, ID=14 mm, L=172 mm) were made from cores drilled parallel to the bedding planes. The tests consisted of loading the sample to in situ conditions (4.5 MPa vertical stress and 2.2 MPa pore pressure), then decreasing the internal pressure from 4.5 to 1 MPa. X-Ray Computed Tomography (XRCT) and permeability measurements were used in order to study the evolution of the inner hole without removing the sample.

The results shows larger convergence parallel to the bedding planes on the clay close to the walls, however this trend is according to the authors reversed further inside the clay, see Figure 0.17 and Figure 0.18 (You, et al., 2010). Although this is not a creep test per se, it excellently demonstrates considerable ductile radial displacement as a result of rapid internal pressure reduction. Clear anisotropic displacement effects related to the bedding planes are observed and also considerable deformation has taken place without the results here showing signs of significant localized fracturing.

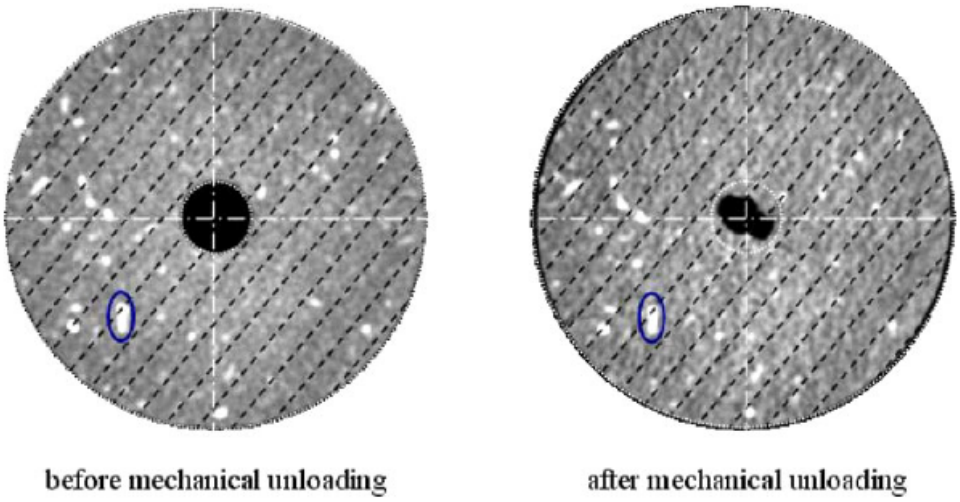

Figure 0.17: CT-slices of the Boom Clay sample before and after the mechanical unloading. It is clearly visible that the radial strain parallel to the bedding planes is significantly larger in the vicinity of the internal hole (You, et al., 2010).

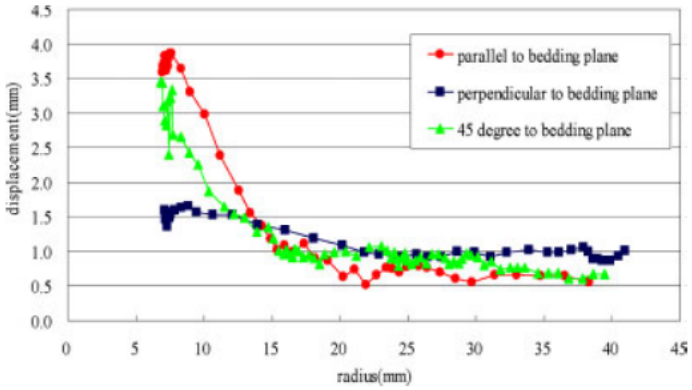

Figure 0.18: Displacement vs radius for different angles to the bedding planes (You, et al., 2010)

1.11.3 Time-dependent behavior of deep clays (Giruad & Rousset, 1996)

Material Characteristics

Cylindrical Boom Clay samples were cored from a depth of 230 meters and had high porosity (~45%) with a density of 1.95 g/cc. An undrained triaxial test with 5 MPa confining pressure shows that the deviatoric stress reaches its maximum (~2 MPa, can be interpreted as short term strength) value at high levels of axial strain ~5%, highlighting the expected ductile behavior of the material. A cyclic test reveals that a major part of the deformation remains after unloading, the sample generally showed plastic behavior with strain hardening. In an undrained isotropic load-unloading test the Skempton's B coefficient was determined to be 1 (meaning the pore fluid carries the extra load applied) something which is to be expected from water saturated plastic clays (Giruad & Rousset, 1996).

Effects of Pore Water

The creep test was done both under undrained and drained conditions in order to determine the Boom Clays time dependent deformation's relationship with water pressure diffusion. The first load step was under undrained conditions with 1 MPa deviatoric stress with 5 MPa confining pressure, i.e. approximately half of the short term strength determined earlier. No significant time dependent changes occur, axial deformation quickly comes to an end, practically instantaneous, see Figure 0.19. In the subsequent load step (sample still not being allowed to drain) the deviatoric stress is increased to 1.5 MPa and shows an instantaneous increase in axial strain from 0.5 to 0.8 %, a further increase from 0.8 to 1.3 % is then observed over the course of 600 hours. During this loading step the pore pressure increases slightly, consequently slightly pushing the effective stresses more towards tension (and conventional failure envelopes). The main point here is that the time dependent effect can be observed under undrained conditions, where homogenous pore pressure distribution is somewhat reasonable to assume, supporting pore water being linked to deformation not only through consolidation effects.

The last part of the creep test allows the sample to drain through the bottom (under equal stress conditions). Sudden increase in strain rate is observed before it stabilizes to the same rate as before after 100-200h. This can be interpreted as consolidation effects i.e. pore pressure equalizes resulting in water leaving the sample and allows the pore spaces to be reduced. The results can be viewed in Figure 0.19, note that the second load step shows the deviatoric stress to be 1 MPa, this is supposed to be 1.5 MPa (Giruad & Rousset, 1996).

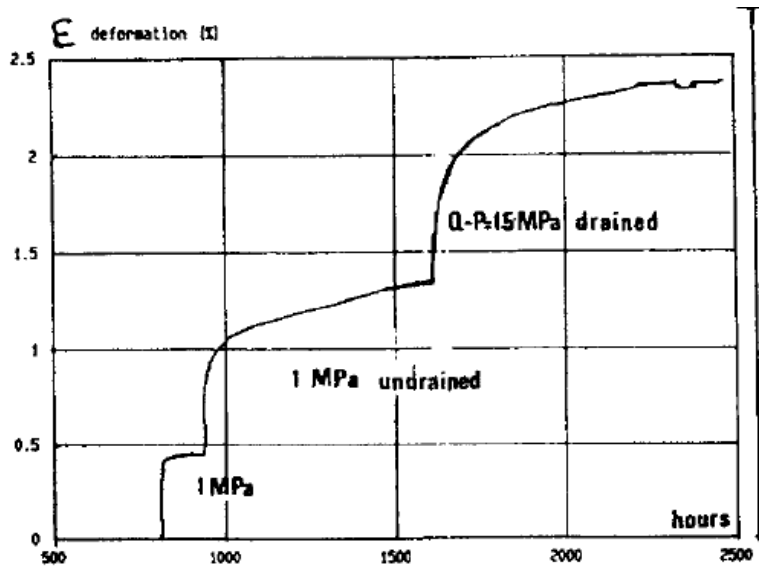

Figure 0.19:Results from the triaxial creep test showing strain as a function of time for the three stages (Giruad & Rousset, 1996)

Effects of Temperature

Other creep tests performed, but not described, under higher temperatures suggests that creep is enhanced by higher temperatures. The threshold for creep is lowered, the rate of strain is increased and the failure strain is higher.

1.11.4 Creep behavior of boom clay (Yu, et al., 2015)

Material Characteristics

Cylindrical samples consisting of about 60% clay minerals dominated by illite, interlayered smectite and illite, kaolinite and traces of chlorite (matches relatively well with the composition given in section 1.11). The cores were retrieved from 233 meter depth with in situ conditions of 4.5 MPa vertical stress, 2.2 MPa pore pressure and horizontal to vertical stress ratio $\left(\frac{\sigma_h}{\sigma_v}\right)$ in the region of 0.5-0.9. The water content in the samples ranged from 24.4-25.5% and it was taken special care to avoid altering the in situ saturation. The apparatus used is specifically designed for creep tests and to prevent excessive influence from temperature and chemistry from the synthetic water used. For a more detailed description of the preparations before the loading steps (saturation phase etc.) the reader is encouraged to see original report (Yu, et al., 2015).

Effects of Pore Water

The creep test consisted of several deviatoric load steps under both drained and undrained conditions that lasted two months each, see Figure 0.20 below:

Samples	Confining pressure σ_3 (MPa)	Water pressure p_l (MPa)	Deviatoric stress $(\sigma_1 - \sigma_3)$ (MPa)	Drained conditions
TCP1	4.7	2.2	0.5, 1.0, 1.5,	Undrained
	4.7	0.0	2.0, 2.5, 3.0, 3.5, 4.0	Drained
TCP2	4.7	2.2	0.5	Undrained
TCP3	4.5	2.0	0.5, 1.0, 1.5, 2.0, 2.5	Drained

Figure 0.20: Test procedures for the creep phase, note that compressive stresses are defined as positive (Yu, et al., 2015).

Each load step resulted in an immediate increase in strain, but as the deviatoric stresses increased this effect became decreasingly significant, see Figure 0.21.

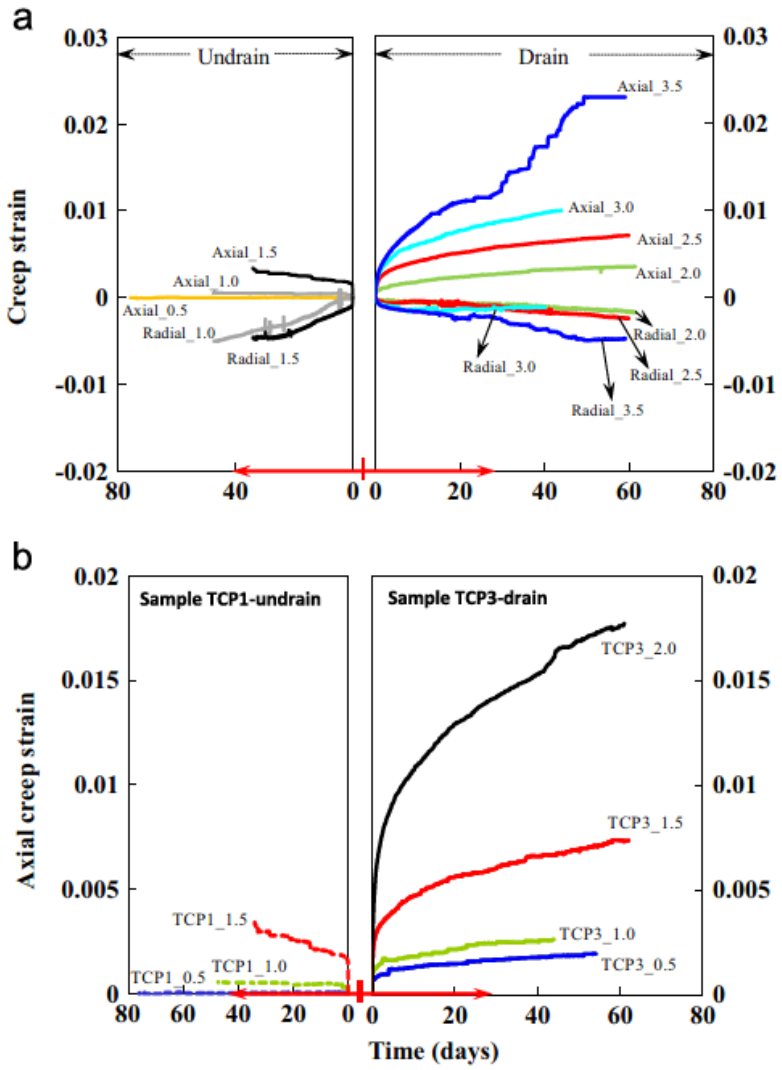

Figure 0.21: Comparison of strain with respects to time and deviatoric stress level. (a) Sample TCP1 (b) Sample TCP1 vs. Sample TCP3 (Yu, et al., 2015).

In an effort to characterize the threshold for creep, low deviatoric load steps were observed and the results suggested that the threshold for creep is around 1 MPa, this matches nicely with other experiments (Yu, et al., 2015) and sources therein (Giruad & Rousset, 1996). For each load step the strain rate converges to an approximately constant rate after 20 days, by taking the average strain rate from this point until next stress step (two months) a quasi-steady state creep rate is determined. This rate increases exponentially as the deviatoric stresses increases. Sample TCP3 failed at the loading step of 2.5 MPa deviatoric stress and 0.8 years into the test, while sample TCP1 failed at the loading step of 4.0 MPa deviatoric stress 1.5 years into the test, see Figure 0.22.

Figure 0.22: The failed samples. TCP1 left and TCP3 right (Yu, et al., 2015).

In situ comparison

To interpret and validate the results from the creep test in the laboratory a comparison of data retrieved in situ from the Boom Clay formation is also included. The data for a wellbore which has been monitored for ~19 years is shown below in Figure 0.23, it demonstrates that after all this time the strain rate is still not reduced to zero. The in-situ data confirms Boom Clay creeping ability, but shows a quasi-steady creep rate one order of magnitude lower than the from the laboratory creep test. The in situ quasi steady state diameter reduction rate (taken from 1996-2006) for the wellbore was calculated to be in the order of $10^{-8}\ 1/hr$, and was not reached before around seven years. This is not very surprising as there are several differences from lab experiment, in particular the tendency of samples getting damaged during extraction and also in this case the timescale (two months might not be sufficient for reaching steady state creep rate), existence of fractures, support from tunnel linings and scaling effects.

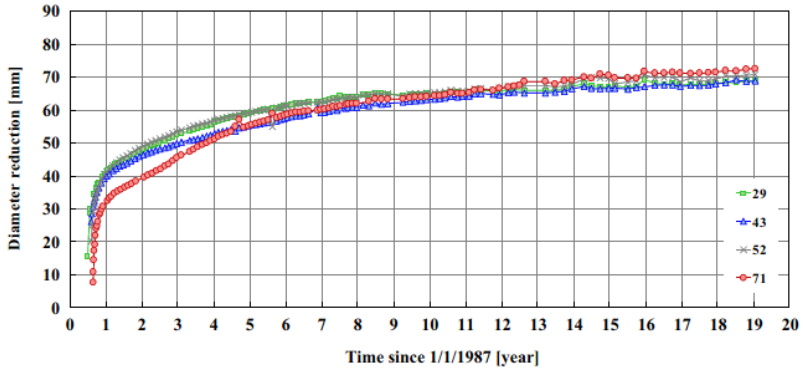

Figure 0.23: Measurements of in situ wellbore diameter reduction with different diameter rings (Yu, et al., 2015).

1.12 Brief summary of preliminary results from SINTEF Research project: "Shale as a Permanent Barrier after Well Abandonment" (SINTEF Petroleum Research, 2016)

Total is part of an ongoing research project on shale barriers at SINTEF Petroleum Research in Trondheim. The main focus and goal of the project lies in researching how to engineer a shale barrier in a consistent way, i.e. what can be done in order to stimulate and/or make the process happen in a consistent manner when barriers are not forming naturally? This is partly done by triaxial lab experiments on hollow cylinder samples (both outcrops and field materials), testing pressure, temperature and chemical effects on the convergence of the inner hole. In addition a shale barrier test is also performed, with a steel tube in the in the center of the hollow cylinder (representing the casing). Keep in mind that scaling up the hollow cylinder samples to borehole conditions is not trivial and the experiments are mainly carried out to investigate how different conditions affect the displacement mechanisms.

Material Characteristics

The tested materials are provided by the operators and are mostly from formations where experience has shown barriers forming repeatedly, typically high porosity weak rocks with high amounts of clay minerals and in particular smectite, and low amounts of carbonates and quartz. See Figure 0.24 for some of the tested materials.

	Porosity [%]	Total clay [%]	Smectite [%]	Quartz [%]	TOC [%]	Surf. Area $[m^2/g]$	G [GPa]	v -
Pierre	20.8	47.9	5	26.6	1.1	17.0	0.18	0.43
Field material 388	39.7	85.2	67	5.3	3.3	17.2	1.4	0.39
Field material 357	38.1	62	45	14.5	0.8	39.9	0.5	0.5
Sele equiv.	47.5	75.4	25	9.6	1.3	54.5		
Lillebelt	50.1	87	25	8.0	0.5	28		
Mont Terri	16	62		19				

Figure 0.24: test materials at ongoing research at SINTEF (taken from steering committee presentation 7, Trondheim 24.11.2016 (SINTEF Petroleum Research, 2016))

Preliminary Results

So far chemical effects, such as swelling, has not shown promising results and are consequently also not extensively tested. The current experience suggests that while potentially beneficial to creep/displacement, it seems to have slower and perhaps smaller impact than temperature and pressure effects.

Temperature has shown mixed effects. Increasing the temperature on the Field material 357 gave positive effects on barrier forming (softening the shale), while increased temperature had negative effects (stiffening the shale) on the Pierre shale sample (outcrop). This is potentially not only linked to the different compositions of the materials, but also their origin, the field material could perhaps be more representative for downhole formations.

The effect of decreasing internal pressure is both done by stepwise reduction of the internal pressure and observing creep response and also rapid drawdown of internal pressure with a constant rate. The latter has for example shown promising results on for example the Field material 388, see Figure 0.25, Figure 0.26 and Figure 0.27. The different creep tests show that some of the materials form barriers (Field material 357 and 388 sample) while others do not (Pierre), despite massive persuasion, see Figure 0.28.

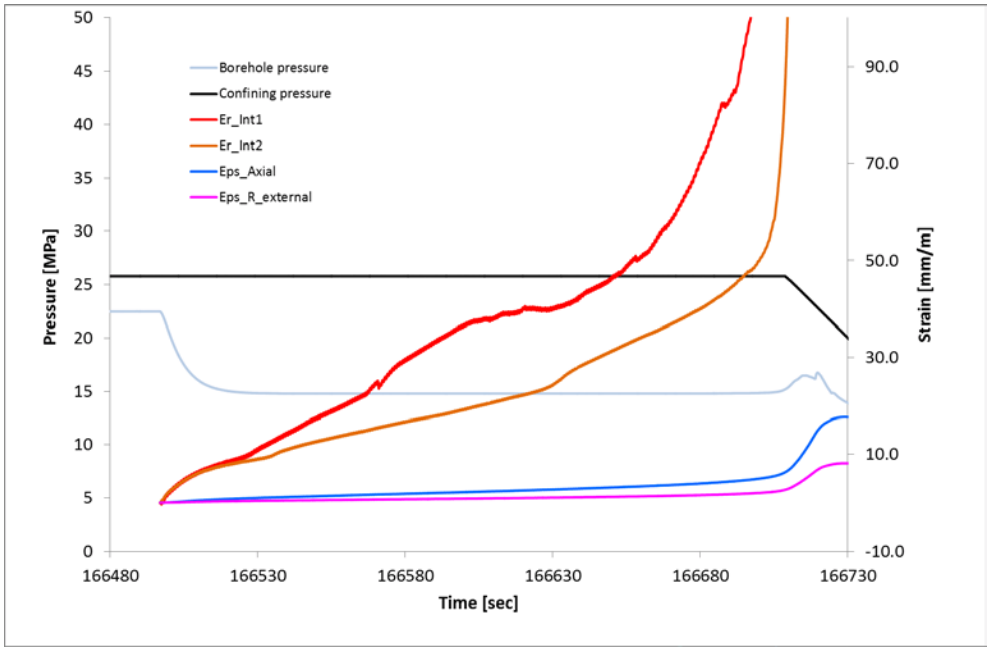

Figure 0.25: The effect of rapid decrease in "borehole" pressure on the Field Material 388 (SINTEF Petroleum Research, 2016).

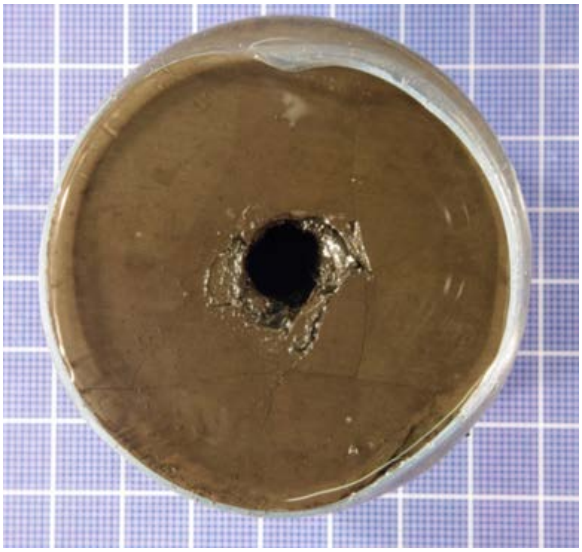

Figure 0.26: Top surface of sample where after test. Borehole was closed (before debris was removed) and the plastic region was extended to the sample boundary (taken from SINTEF REF 2015_8_27 ML388 (SINTEF Petroleum Research, 2016)).

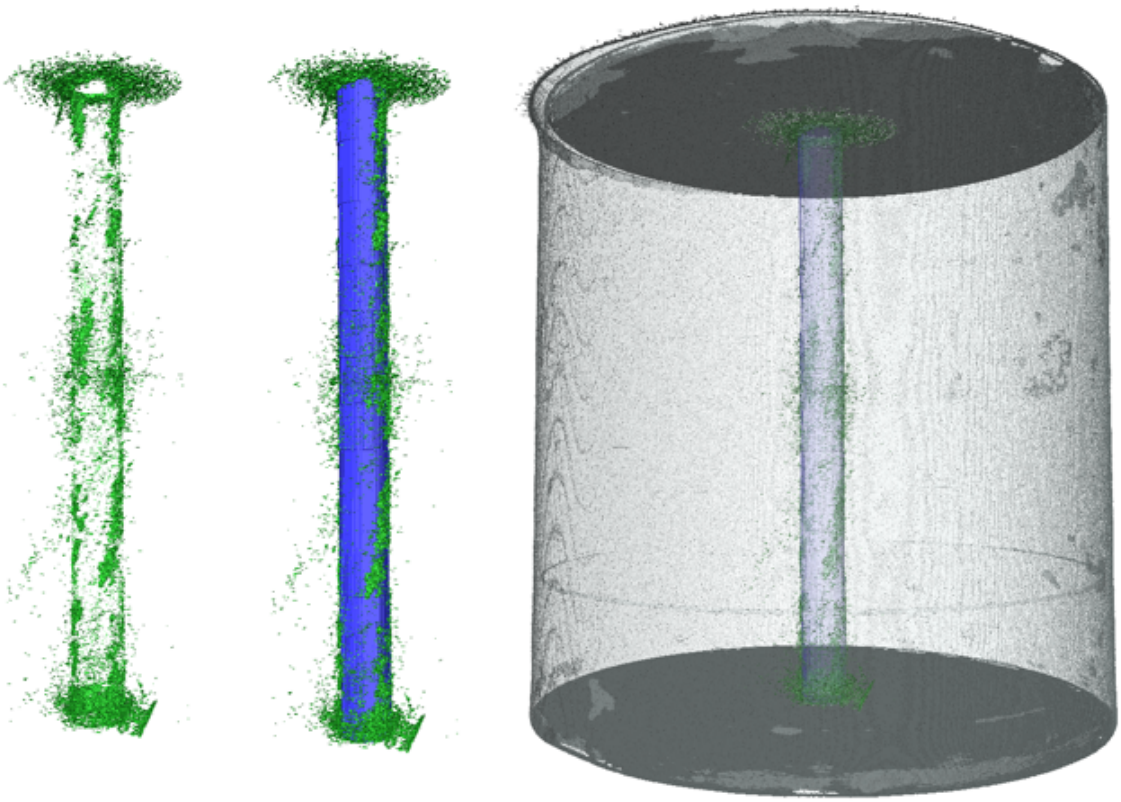

Figure 0.27: Post-test µCT scan of the the Field material 388 showing that the annulus is sealed, but with a region around the casing with higher porosity. Green areas represent holes/defects, while blue represents casing (SINTEF Petroleum Research, 2016).

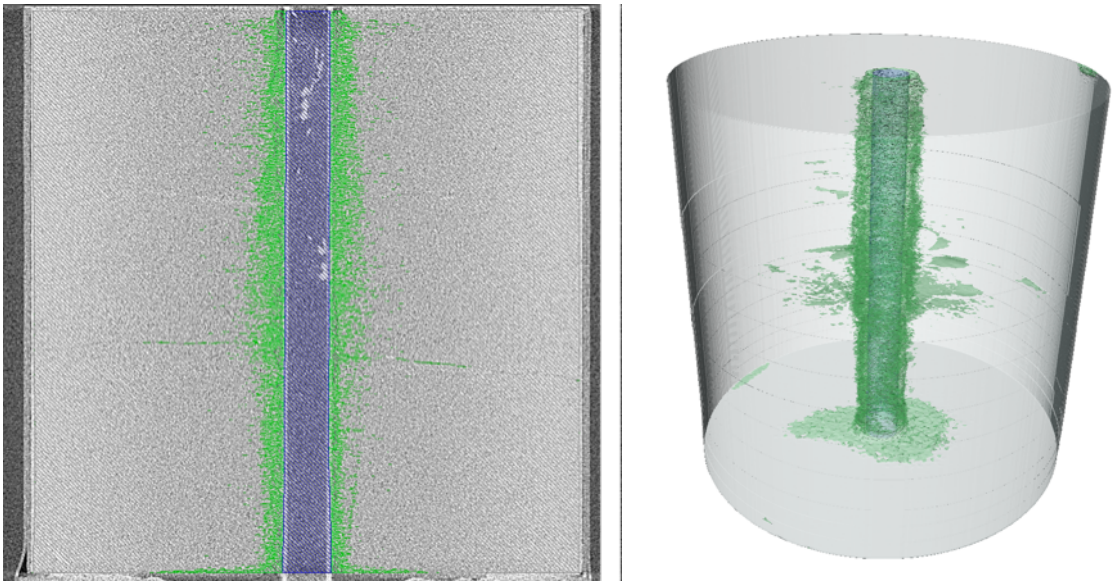

Figure 0.28: post µCT scan image of Pierre shale showing a significant volume of high porosity around the casing. Green areas represent holes/defects, while blue represents casing. (SINTEF Petroleum Research, 2016)

1.13 Discussion: Some General Creep Correlations

In addition to what is discussed above multiple experiments; for example (Li & Ghassemi, 2012) (Sone & Zoback, 2014) (Sone & Zoback, 2013), show that the material composition has strong influence on the amount of creep. In general rocks with low amounts of typical cementing materials such as quartz and carbonate and large amounts of clay minerals and organic material creep more. Young's modulus of a shale generally increases with increasing quartz and carbonate (depends on distribution and grain size) content and increasing brittle strength of a rock, which implies that it can be a useful indicator for degree of creep, this is shown well in for example (Sone & Zoback, 2013).

The ductile creep behavior of a rock correlates relatively well with the rocks brittle strength, and unconsolidated rocks usually creeps more than consolidated ones. The degree of compaction/consolidation in a clay-rich formation is linked to pore pressure diffusion and effective stresses, and porosity is usually an excellent indicator for degree of consolidation. It is shown well by (Mondol, et al., 2008) that smectite dominated shales can be expected to be significantly less compacted and have lower permeability than for example kaolinite dominated shales. This is linked to stress being distributed to a very large number of clay contacts in smectite rich clays, as smectite is an extremely small particle (10^{-4} to 10^{-5} mm) compared to for example kaolinite exceeding 0.01 mm. High amounts of smectite appears to be beneficial for creep, which is probably due to several reasons. Available industry experience confirms a strong correlation between creeping formations and smectite content, see for example (Williams, et al., 2009) (Kristiansen, 2015) (Hogg & Davison, 2015) (Carlsen, 2017).

In highly compacted indurated clays a considerable part of the total water content is strongly bound to clay-mineral surfaces, and will not undergo advective transport in the presence of normally-encountered pressure gradients. These interparticle water films are also able to carry stress (potentially entire lithostatic stress) and thus act as hydraulic barriers preventing external water from entering and undergo transport if the external water pressure is lower than the local pore pressure/water film pressure (Horseman, et al., 1996). Furthermore, it is a recognized phenomenon that certain clay minerals have swelling abilities in presence of water (see section 0), such swelling shales are suggested as good candidates for forming barriers (Williams, et al., 2009). Water appears to play a key role in the creeping mechanisms. Thermal expansion of pore fluids is larger than expansion of the solids, this and swelling effects potentially increases the pressure in pores and interlayer water. Combined with low permeability, this can give rise to localized overpressured zones even under drained conditions, see for example (Zhang, et al.,

2007). The increased internal pressure effectively brings the rock closer to conventional failure envelopes (/reduces its strength) and increases creep. Normally clays become hard and lose their plasticity when subjected to heat (see Pierre shale from SINTEF project) (University College London, s.d.) and the trend that higher temperature appears to enhance creep can potentially be linked to reduced viscosity in the interstitial water leading to less shear resistance between the clay particles (Zhang, et al., 2007). Pore water release due to thermally-induced evaporation could cause shrinkage (technically not a creep-mechanism). This desaturation might also cause increased shear resistance as fluid is removed, and thus reduce creep. Simulations in (Fjaer, et al., 2016) suggests that temperature appears to increase the strain rate but not the final strain significantly, however for example (Giruad & Rousset, 1996) and suggests that final strain is also increased. Thus it seems temperature effects can in combination with water appear to be beneficial for some, but not all shales. In general the temperature effect on creep rate is observed to be higher for less compacted/consolidated shales, see experiemnts above and (Su, 2013).

The above creep tests (and many more) show that more profound creep is observed for higher deviatoric loadings. It is a general conception that the closer a rock is to failure the more it creeps. Moreover, ductile behavior has a tendency to occur more frequently under high confining pressures when opening a fracture is hard, see (Zhang & Rothfuchs, 2004) (Fjaer, et al., 2008). Creep tests also reveal that for some rocks there exists a threshold for creep while in other rocks it does not (Fjaer, et al., 2008)

The structure of shales leads to a significant degree of anisotropy, more strain and lower strength is observed in the direction perpendicular to the beddings, but more profound dilatancy when loaded parallel to bedding planes, see for example (Naumann, et al., 2007). No such features were tested for the Heather shale but similar behavior is assumed to be realistic.

Industry Experience and Field Cases

This section investigates and briefly discusses the available industry experience, what are the reoccurring patterns? Can potentially the logging while drilling (LWD) data (Porosity, Density, Gamma Ray, mud type and weight etc.) be of help when predicting shale and/or claystone sections creeping - or call it displacement capacity. Which, if any, indications can be of help from this data? Available industry experience on the NCS suggests that the shales and clay in the Hordaland group are particularly conducive formation for barrier forming with several operators (Statoil with several fields, Shell with "Brent" and BP with "Valhall") having confirmed barriers in this formation (Hogg & Davison, 2015) (Carlsen, 2017) (Kristiansen, 2014). For Total, repeated cement bond logs (CBL) and isolation scans (IS) with time intervals of up to six months, in the Middle Lark Formation (Eocene to Mid-Miocene in the Hordaland Group), show clear indications of formation closing the annular gap, further supporting this trend. The repeatedly good results in the Hordaland Group makes it interesting to study the well data for this lithology, and compare it to other groups less suitable for barrier forming.

1.14 Total Field Case, Can Creep be Linked with LWD?

To investigate the possible patterns on LWD data that perhaps could be of help in predicting creep, a comparison between the intervals which has demonstrated good creeping capacity with the intervals which has shown no or little creeping capacity is done for Totals' two available wells (with relevant data). Available LWD data in the relevant intervals (where logs have proved significant creep) are scarce, thus in order to make an assessment the LWD data from the pilot holes (not same welltrack which is logged for bonding) are used under the assumption that the geology is homogeneous laterally. In practice this is done by comparing measurements from the same true vertical depth (TVD) intervals. Consequently it should be noted that a certain degree of error is associated with the following analysis.

(However the TVD assumption seems to be somewhat reasonable, supported by the fact that NORSOK allows for logs alone to qualify formation barriers once the initial barrier for that formation has been confirmed through pressure testing)

1.14.1 Field Case Details

The geometry and drilling fluid parameters for the relevant wells in the relevant sections are shown below in Figure 0.1. As mentioned previously, this geometry requires the formation at the borehole wall to undergo a total strain of approximately 27.2%. The drilling fluid is non-aqueous-based-mud (NABM) with a density of 1.40 SG and an oil-water ratio of 75/25. (It is

assumed that the same mud is used in both wells, but only confirmed in Well A). Therefore it is assumed that swelling/chemical displacement is negligible in this case. Small deviations in borehole size, casing centralization, mud density and composition, are also assumed negligible.

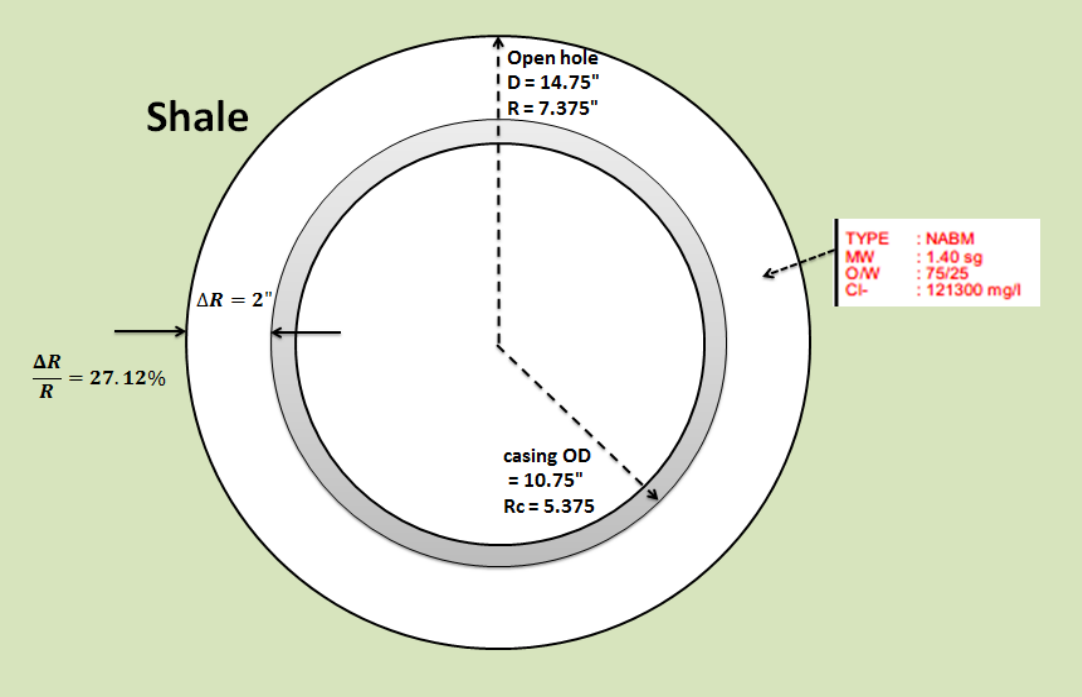

Figure 0.1: Wellbore geometry and fluid parameters

The intervals in focus are the Clay regions in the Hordaland group. Based on XRD/QemScan analysis of cuttings from Norwegian and UK continental shelf, the mineralogical composition is described as complex, but can roughly be summarized as (Skaug, 2016):

- Low amount (<10% mass) of calcite and dolomite (exception is lower parts of studied interval)
- In most samples there are small amounts of apatite, barite, anatase and clinoptilolite
- Total amount of Clay and Micas from 12-70% mass
    - Smectite 8-46% mass (strongly swelling)
    - Interstratified illite-smectite 4-19% mass (poorly swelling)

High amount of smectite content is found in the interval above the Utsira sands (commonly known as the Green Clay) in the Hordaland group. Below in Figure 0.5 mineralogy data are shown versus TVD, (these values are taken from Well C).

1.14.2 Case 1: Well A

The well section investigated stretches from top of Frigg reservoir (1968.7 m MD) and up to the 20" casing shoe (1208 m MD) and was drilled 14th of February 2015. Since the casing setting there has been run CBL and IS on four separate occasions (all in 2015):

Date of logging	Time since drilled [days]	Log interval [m MD]
February 21st	~7	283.47-2059.45
February 24th	~10 (+3)	166.69-2060.85
March 2nd	~16 (+9)	701.07-1989.76
July 10th	~153 (+146)	1683.42-2019.08

Difference in acoustic signatures reveals an increase in the amount of solids outside the casing between each log. While the increase in solids is clearly visible between the three first logs, there is not observed significant intervals with adequate bonding before the last log (approximately six months after the first log) see Figure 0.2 and Figure 0.3, implying a slow displacement rate, (which matches nicely with creep as displacing mechanism).

1180-1350 m TVD

From 1180 m TVD, the bond logs indicate free pipe down to 1340 m TVD where medium bond quality is observed for approximately 20 m TVD. These intervals matches reasonably well with expected behavior based on smectite and quartz content, the free pipe interval has relatively high quartz content, while the medium bond interval matches fairly well with a dip in quartz content and a jump smectite content at around 1350 m TVD. Comparing with the well data the most visible correlation is the sonic velocities and smectite content which seems to follow somewhat the same trend. More precisely as the smectite content increases the sonic velocities decreases (meaning increase in traveltime, which is what is shown in the logs), normally implying a more weak and ductile formation with lower bulk modulus. See Figure 0.4 and Figure 0.5.

1350-1410 m TVD

From ~1350-1410 m TVD the bond quality is poor, however the lithology here is most likely not shale. This can be interpreted from the gamma ray and effective porosity measurements (not displayed here) and the lithology log, see Figure 0.5.

1410-1780 m TVD

The rest of the logs down to ~1740 m TVD can very roughly be described by a somewhat gradual decrease of bond quality from high to moderate at ~1410-1435 m TVD down to poor bond quality at ~1560. Followed by a reversed trend of a somewhat gradual increase of bond

quality from “poor” to “high to moderate” at ~1715-1740. From here and down to the Frigg reservoir (~1780 m TVD) the bond quality is generally varying. Traces of creep are observed, but this section is more likely significantly affected by the solids from the cementation, and perhaps also deposited mud particles.

These intervals show distinct trends between the bond quality and the sonic velocities, porosity (from nuclear magnetic resonance (NMR) tool) and the density measurements. Please remark here that the scales for the different LWD data are altered in order to give a more visible result. Trend lines shows that the decrease in density and sonic velocities as well as the increase in porosity matches reasonably well with the gradually degrading bond quality interpreted from the CBL and IS. This trend reversed for the interval where the bond quality is gradually increasing. The trend seems perhaps to be more profound on sonic velocities, than density and porosity measurements, see Figure 0.4.

A strict TVD comparison between the mineralogy and LWD data gives some results which seem illogical compared to expected trends. In particular the interval ~1410-1435 m TVD (good bonding) which lines up with a dip in smectite content and jump in quartz content on the mineralogy chart. Although the lithology is considered relatively flat above the Frigg reservoir, considerable differences can exist for certain depths. It is tempting to think that the mineralogy of this interval is better represented around ~50 m lower on the mineralogy chart. When considering it on a larger scale however, it offers more logical explanations. The free pipe interval in the shallow part, has a bit lower smectite content and considerably higher quartz content compared to the deeper interval where good bonding has formed, see Figure 0.5. Although it is probably a combination of several factors such as lower pore pressure, temperature and stresses.

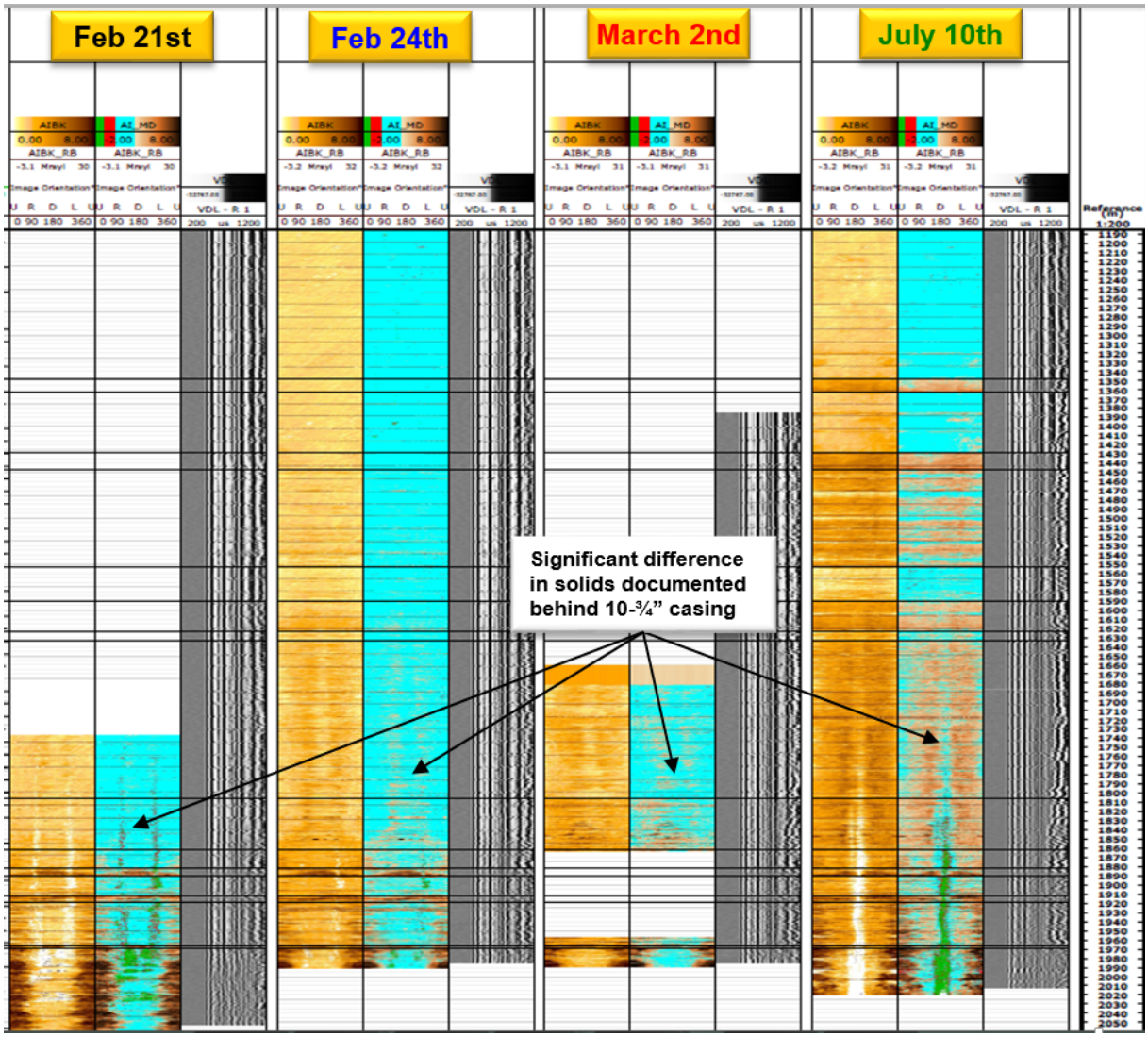

Figure 0.2: Comparison of the acoustic impedance and CBL amplitude for different times. The change in the acoustic signatures clearly show the difference in solid content outside the casing for different times. Graph made from (Skaug, 2016).

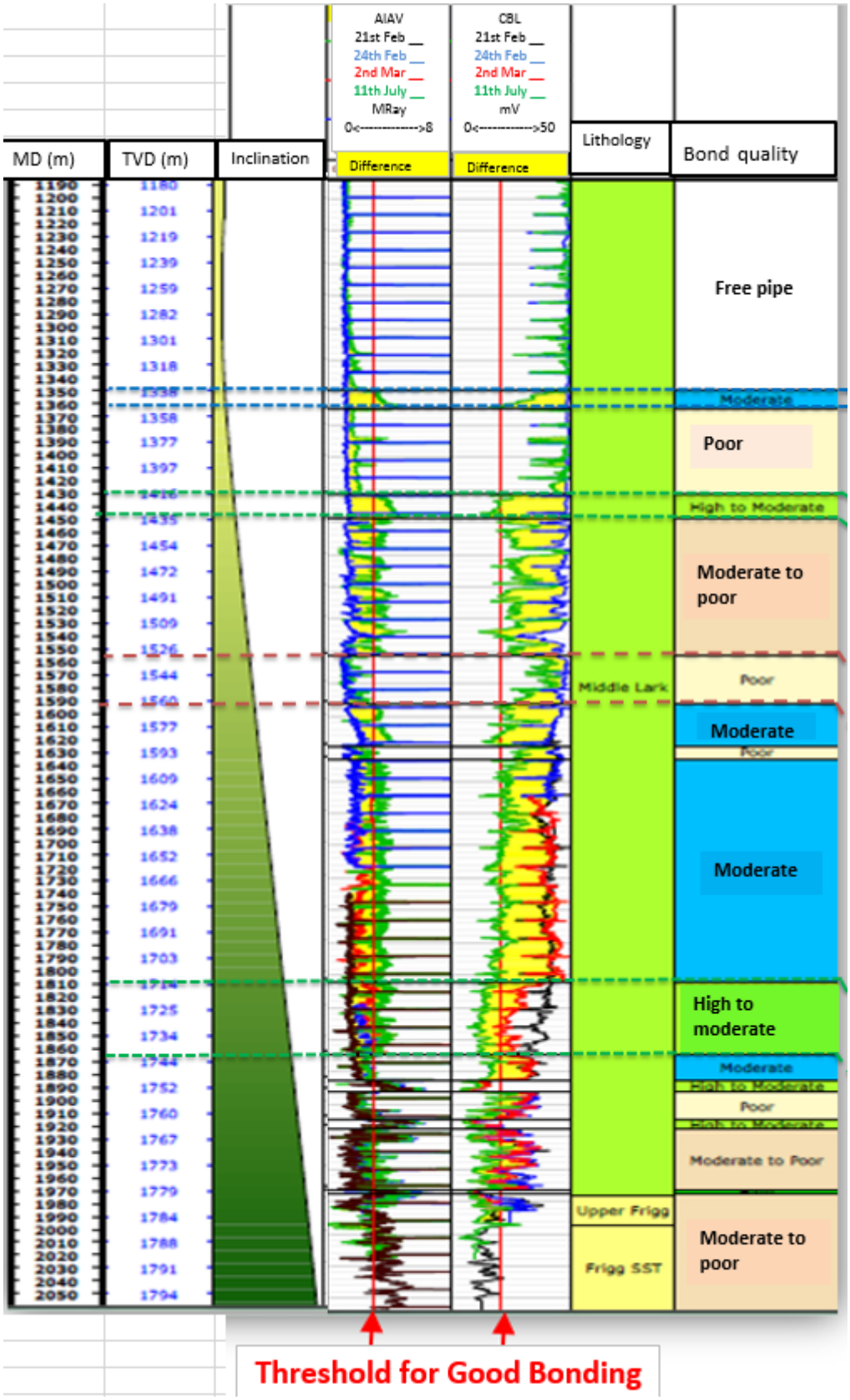

Figure 0.3: Graphs showing the difference in average acoustic impedance and CBL amplitude for the different logs. For comparison reasons measured depth, true vertical depth, inclination, lithology and bond quality are also included. The threshold for good bonding is set according to (Williams, et al., 2009) and the graph made from Totals JIP presentation (Skaug, 2016).

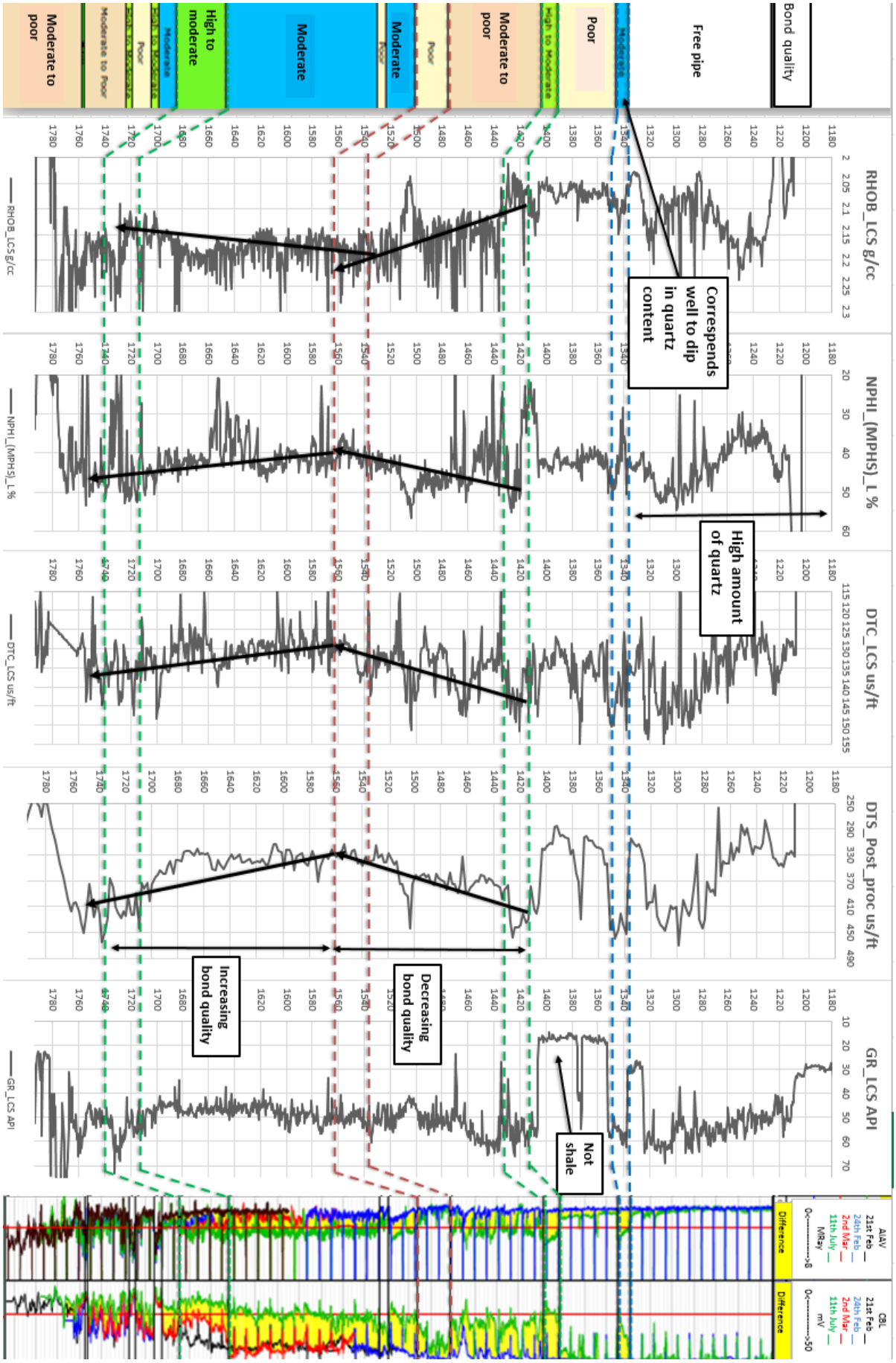

Figure 0.4: LWD data and CBL+IS measurements plotted with TVD correlation for case 1.

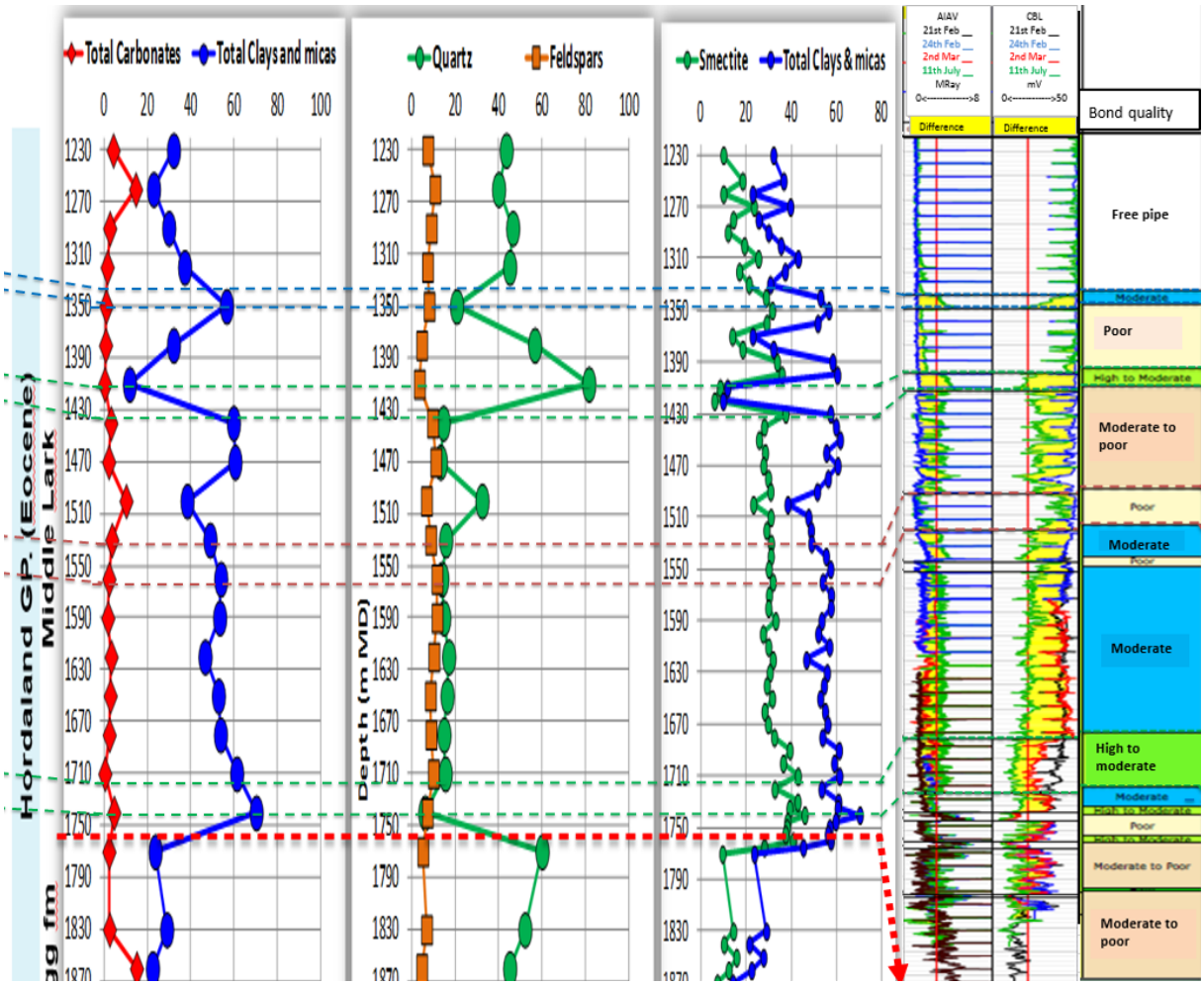

Figure 0.5: Mineralogy vs TVD with key sections extrapolated to the CBL+IS and bond quality measurements for case 1. Graph made from (Skaug, 2016).

1.14.3 Case 2: Well B

The well section investigated stretches from top of Frigg reservoir (2477.5 m MD) up to the 20" casing shoe (1236 m MD) and was drilled 28th of February 2015. Since the casing setting there has been run CBL and IS on two separate occasions (both in 2015):

Date	Time since drilled [Days]	Depth Interval [m MD]
April 6th	~6	1210-2444
April 23rd	~23 (+17)	1200-2444

It is observed an increase of solid content outside the casing which is revealed by the increase in acoustic signatures. Over the course of 17 days it is observed an average increase of acoustic impedance of 34% and average decrease in CBL amplitudes of 20%. At the time of the last log there are no extensive (> 1meter) intervals with adequate bonding quality, see Figure 0.6.

1485-1515 m TVD

In general, the TVD intervals with most profound creep correlates well with smectite content. The exception is the seemingly irregular interval where moderate bonding has formed in a relatively shallow interval (~1486-1507 m TVD). Nevertheless, this interval has low density and relatively slow sonic velocities supporting the trend observed in case 1. Regarding the porosity (from neutron porosity tool) and the gamma ray there are no clear trends which differentiate this interval from its neighboring intervals where significantly poorer bonding has formed, see Figure 0.8.

The interval does not give expected results when compared to same depth on the mineralogy, in fact there is a jump in quartz and carbonates while it has a dip in smectite compared to neighboring intervals. Lateral heterogeneity due to the considerable distance between the wells is suspected to be the reason for this.

1670-1780 m TVD

The same trend as in case 1 is also observed here, confirming that the most smectite rich interval from 1670 TVD down to the Frigg reservoir seems to give highest degree of creep. The sonic velocities and the density measurements follows the same patterns as in case 1 as they decrease with increased smectite content. However, the patterns on the porosity measurement in case 1 is somewhat contradicted here as the porosity appears to decrease in the interval with most creep. The reason for this is unknown, but it should be noted that the porosity is measured with different tools (neutron porosity (NP) tool in case 2, but NMR tool in case 1).

Some intervals in Well A with little creep after nine days still experienced profound creep over the course of six months and formed good bonding. Thus it should be noted that the time frame in this case is relatively short for analyzing the long-term extents of creep. Furthermore, the intervals with most creep between the 1st and 3rd log (nine days) did not proceed to be the intervals with highest amount of creep from 3rd to 4th log (although these intervals did give highest bond quality), see Figure 0.3.

In additions the continuous correlation between MD and TVD was not available for these well tracks, so the correlation was done by considering a few selected key points from the lithology log. Furthermore the distance between these well tracks and the well in which the mineralogy is taken from is longer (>2 km). It is therefore natural to expect a larger error associated with the analysis of case 2 than case 1.

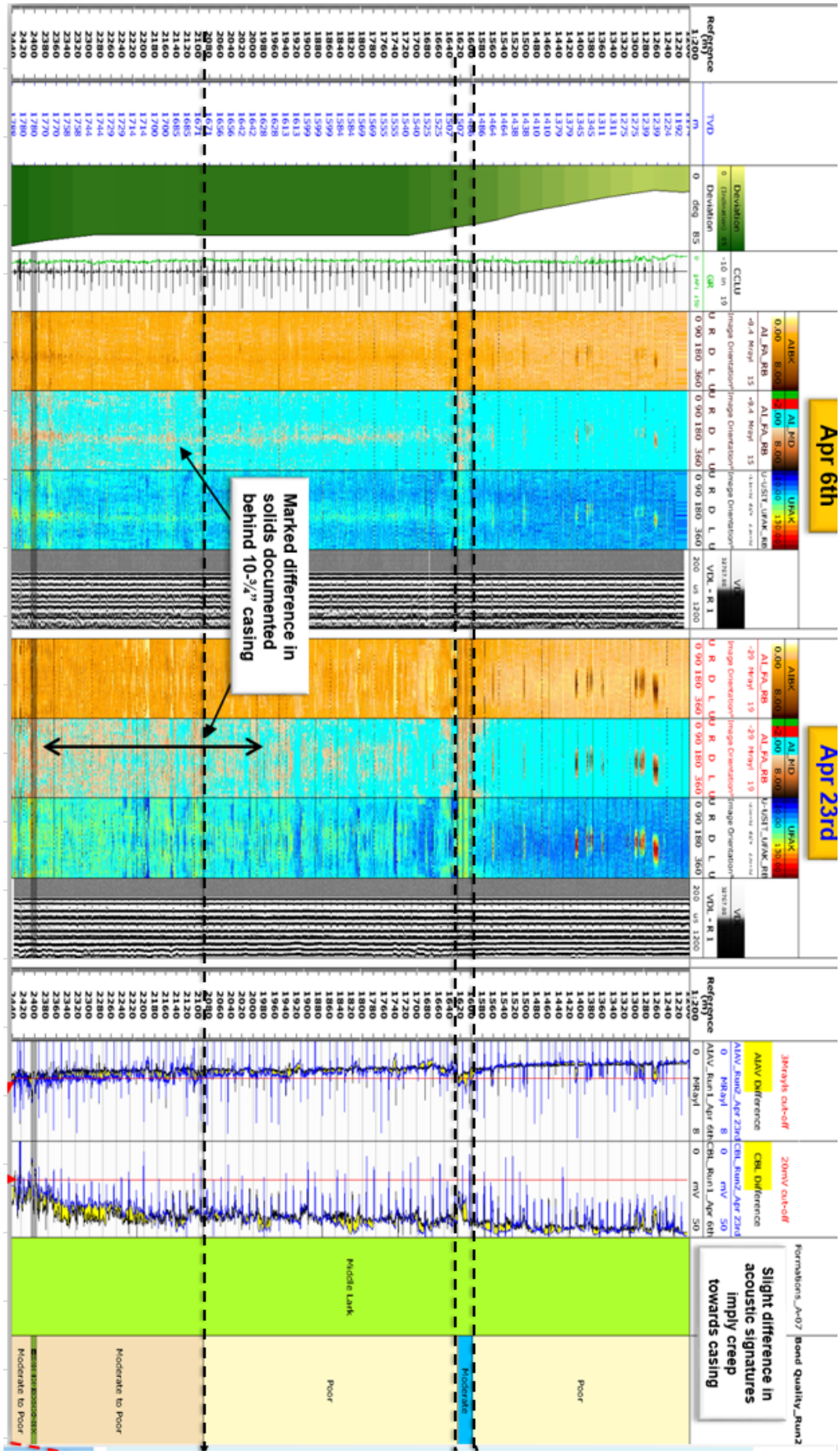

Figure 0.6: Comparison of the acoustic impedance and CBL amplitude for different times. The change in the acoustic signatures clearly show the difference in solid content outside the casing for different times. Graph made from (Skaug, 2016)..

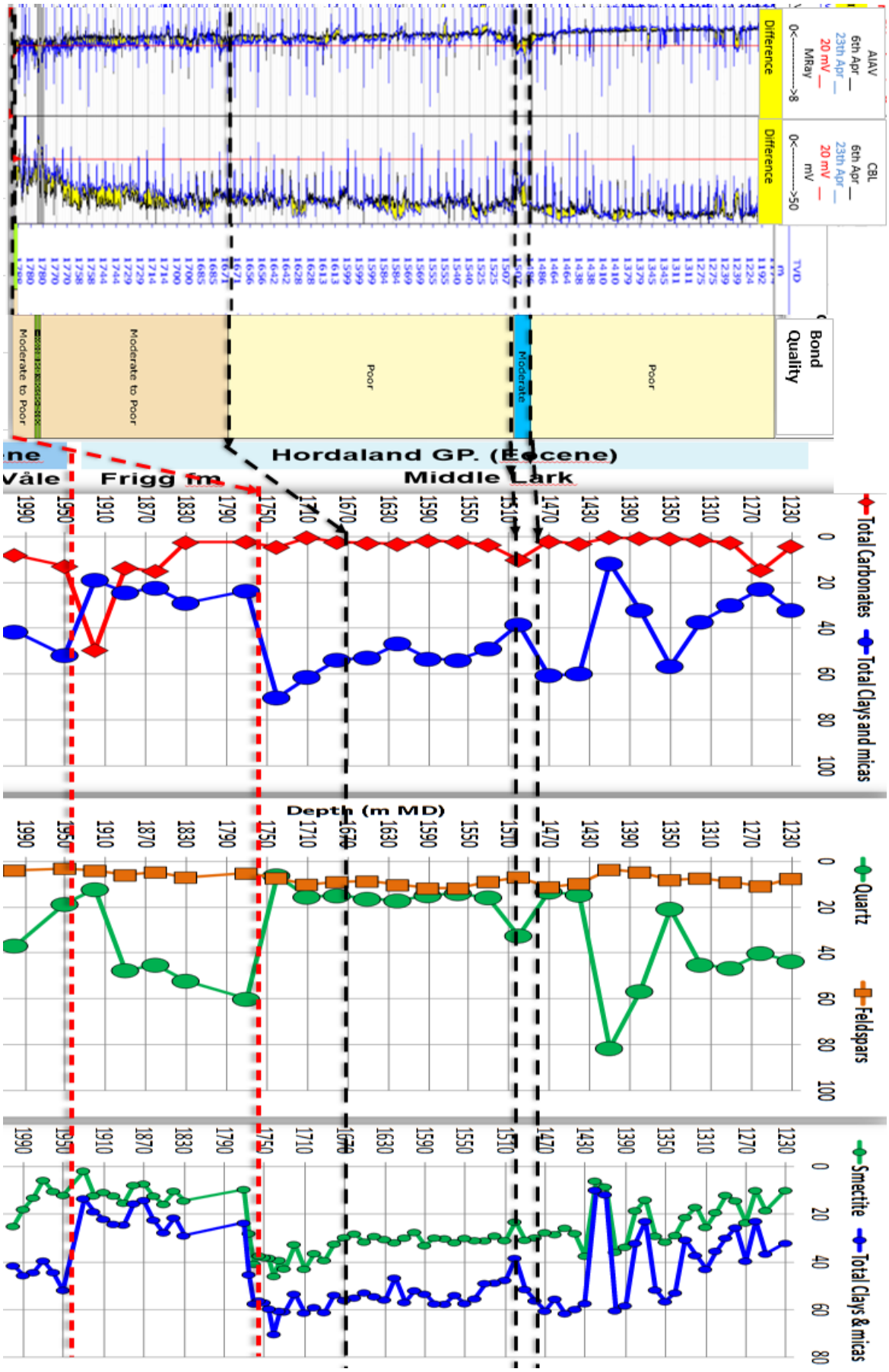

Figure 0.7: Mineralogy vs TVD with key sections extrapolated to the CBL+IS and bond quality measurements for case 2. Graph made from (Skaug, 2016).

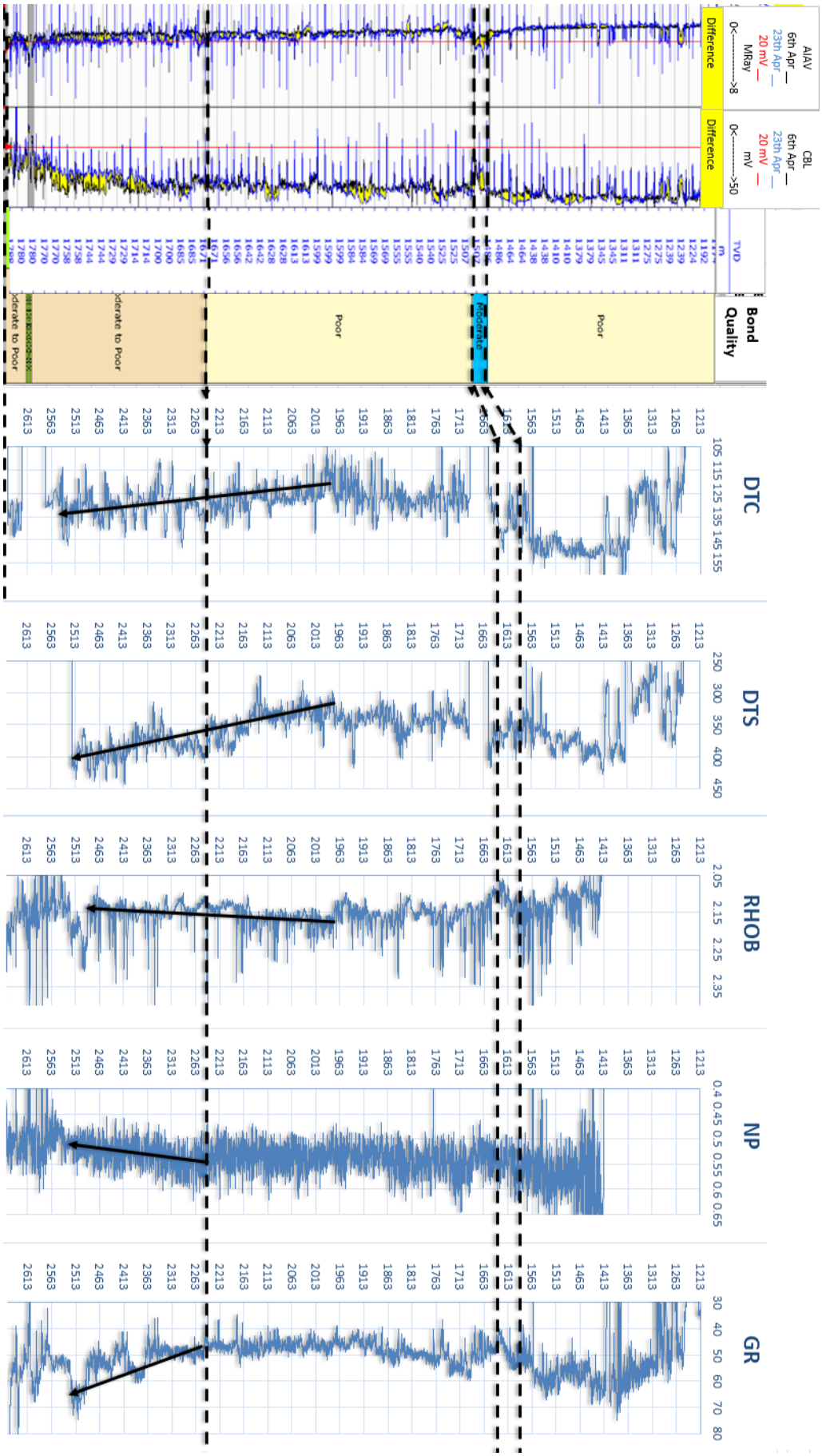

Figure 0.8: LWD data and CBL+IS measurements plotted with TVD correlation for case 2.

1.15 Experience from P&A at Brent (Shell)

Shell plugged 24 wells with shale barriers at the "Brent" field, of which 23 were in the Horda section, see Figure 0.9. Below in Figure 0.10 the geological layers of the overburden is displayed. It is tempting to draw the conclusion that the Horda shale here, is the same, or at least very similar to shale sections analyzed in section 1.14.2 and 1.14.3 (Middle Lark in the Hordaland group).

Annulus Isolation Types (to date)

Isolation	Total	Cement	Shale	Milled
Utsira (13 3/8″)	**41**	9	0	32
Horda (9 5/8″)	**41**	11	23	7
Shetland (9 5/8″)	**39**	23	1	15

Figure 0.9: P&A statistics for the Brent field as of August 2015 (Hogg & Davison, 2015)

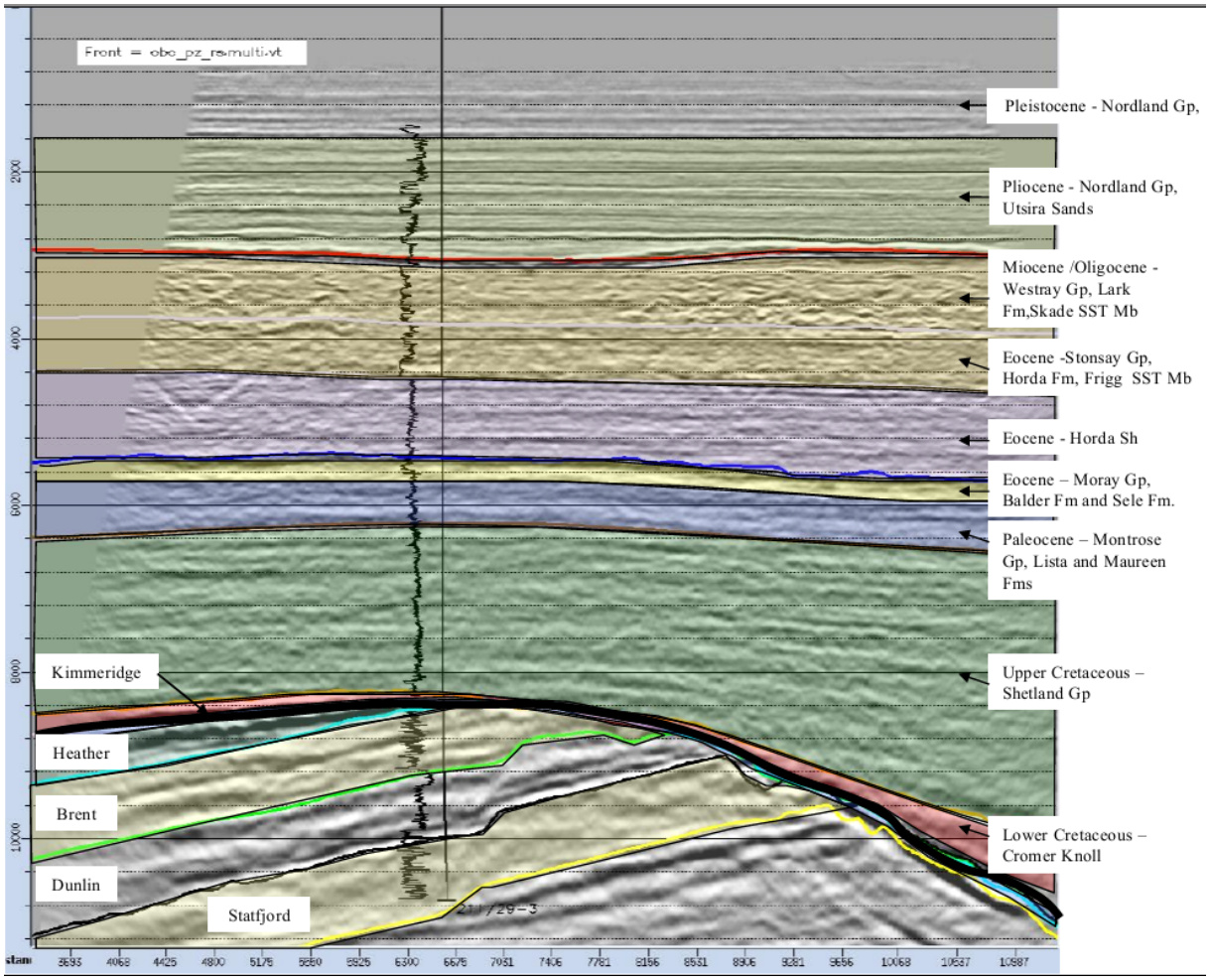

Figure 0.10: The different stratigraphic/geological layers in the overburden of the Brent field (Hogg & Davison, 2015)

The logs are shown below in Figure 0.11 and one of the trends outlined by Shell is the low water content, alternatively seen by the high density in the Pleistocene/Pliocene shales above (Nordland Gp Shales), compared to normal values at this depth. This is shown by the high velocity sonic log and high density log indicating a stiff formation. It is followed by a step change in rock properties starting from top of Lark and down to Balder. The density observed for this shale is lower than the trend, this is seen by the low density measurements and slow sonic velocities, normally implying a more weak and ductile formation with lower bulk modulus. Shell links this change in the trend to the smectite content of the formations, more precisely increasing amount of smectite at deeper intervals in the Eocene shales. (The increasing smectite content vs depth is supported by Statoil, and also the mineralogy from Well C (Carlsen, 2015) (Hogg & Davison, 2015) (Skaug, 2016) (Su, 2015)).

In the upper Shetland formation the logs reveal a relatively fast formation due to increased cementation (higher carbonate content). The lower Shetland appears to follow the same trend, but can be considered more likely to creep according to (Hogg & Davison, 2015).

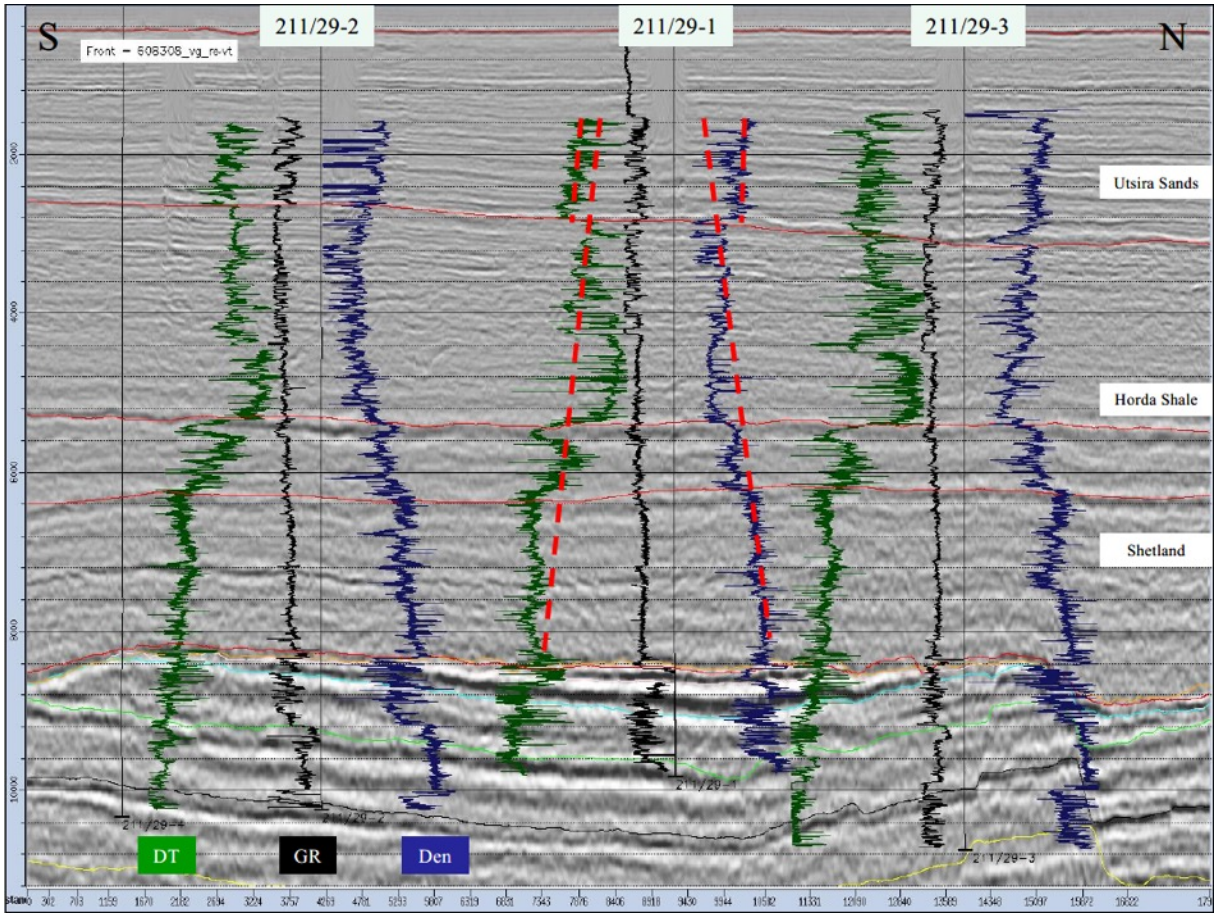

Figure 0.11: Density, Sonic and GR measurements for a selected convenient interval in the Brent overburden (Hogg & Davison, 2015)

A correlation between the specific surface area and the smectite content in a formation was suggested, see Figure 0.12, furthermore these values appeared to be consistent in several wells for the same stratigraphic level. The interval with the highest smectite content in the Shetland formation was the only one where a suitable barrier formed in this layer. The specific surface area also correlates well with the velocity of the sonic log as seen in Figure 0.12.

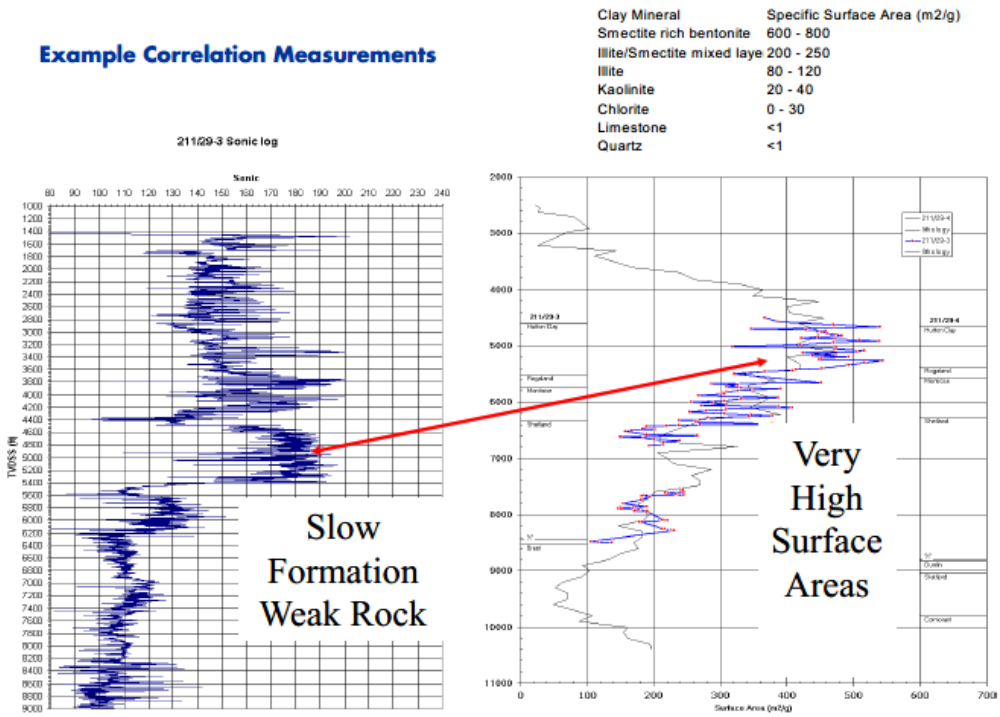

Figure 0.12: Illustration of the slow formation and smectite correlation (Hogg & Davison, 2015)

1.16 Discussion: Field Experiences and LWD Trends

Based upon the log data from the two wells from the Martin Linge field presented earlier and the summarized experience of Shells P&A operations on the Brent field, one can see a few trends between formations forming annular barriers and LWD data. It appears that high sonic travel time (i.e. low sonic velocities), low density and high porosity (compared to the trends in neighboring shales not forming barriers), are things pointing towards a barrier being more likely to form. While gamma ray data does not seem to give any consistent indications other than predicting whether the formation is shale or not.

However, without combining it with analysis of the mineralogy or stress data it appears to be hard to conclude with much based on LWD data alone. This can for example be seen from the interval ~1180-1340 m TVD in Figure 0.4, which has low density and sonic velocities and high porosity with a gamma ray indicating a “shaly” formation. In other words, LWD signs that are linked to creeping formations. When looking at the mineralogy and stress data however one can see that this interval has significantly lower pore pressure and lower amount of smectite and higher amount of quartz than the intervals creeping to the casing.

Based on the industry experience available it seems the clay rich regions in the Hordaland group seem to consistently form barriers. These shales, were deposited during the Eocene and according to (Hogg & Davison, 2015), published studies of the composition consistently show the North Sea Eocene shales having very high smectite content. They differ in several ways from other layers of the overburden; they generally contain less cementing materials such as quartz and carbonate and according to Statoil they are also more fine-grained (Carlsen, 2015). While gamma ray measurements typically are related (empirically) to grain size it did not appear to form clear and consistent differences between creeping and non-creeping shales in these cases.

The amount of smectite in the shales of the Hordaland group increases with depth, this trend can be seen from the mineralogy chart from the Martin Linge well (Figure 0.5) and is also supported by Statoil and Shell (Carlsen, 2015) (Hogg & Davison, 2015) (Skaug, 2016). It is in these deep and smectite rich regions of the Hordaland group (commonly known as the Hordaland Green Clay) that barriers seem to from most consistently. The number of barriers formed in this lithology by Shell and Statoil as well as the observed tendencies in the field cases for Total, indicates a strong correlation between the smectite content and the barrier potential of a formation.

The attributes of smectite is thus key to research in order to get a better understanding of how this mineral coincides with creeping ability of formations (some of which is done in section 0, (Appendix A)). Regarding LWD data smectite often cause very significant effects on petrophysical properties such as porosity and water saturation (Petrowiki, s.d.). From logs, this will lead to reduced density, sonic velocities and resistivity and increased porosity.

Furthermore, smectite content seems to have important effects on degree of consolidation and permeability of a shale formation, with high smectite content potentially leading to high porosity and low permeability as shown in (Mondol, et al., 2008). This can offer some explanation to the very high porosity measurements and the higher pore pressures in the smectite rich intervals. It is worth noting that the depth with highest smectite content coincides the highest pore pressure is found (Su, 2015). Degree of consolidation and proximity to failure have significant effects on the creeping capacity of a rock (see section 0), the high porosity indicates a weak rock and the high pore pressure makes it intuitive to assume proximity to failure. It seems relatively clear that smectite leads to several conditions in a formation that are very beneficial for profound creep. Potentially it plays a big role on the molecular scale (small

scale) too when it comes to the actual displacement processes which takes place when a formation creeps. The naturally high water content in smectite rich shales is probably of great importance, although clay bound water between the clay platelets is more rigid and does not have a comparable viscosity (/residual strength against moving compared to free water) it is tempting to suspect that it plays a role in making the clay platelets slide more easily, in practice acting as a type of lubrication. Smectite is also well known for its swelling effects which often leads to instabilities/displacement (see section 0, (Appendix A)) and although oil based mud (OBM)is used in this case the general chemistry of smectite could still play a key role in the displacement mechanisms. Lastly, (Williams, et al., 2009) suggested that shales that are observed swelling during drilling can be good candidates for forming barriers, tight spots were reported in Middle Lark (Well C) (see post mortem).

As a side note it can be worth mentioning that AkerBP has had field tests where they have circulated fresh water behind the casing in an attempt to stimulate a shale formation not initially forming a barrier. The results were mixed with one successful attempt (after several circulations with breaks in between) and one unsuccessful case (Kristiansen, 2014).

Conoco Phillips tried replacing OBM behind the casing with sea water which perhaps could stimulate the shale barrier forming process. In this case it was not observed significant positive changes after a relatively short period of time (Conoco Phillips, 2015). This can of course be linked to several factors (time, trapped fluid etc.) and later observations from the same company could however suggest that there exists a correlation between the use of water based mud (WBM) and formation creep (Hovda & Holien, 2017)

(Note that clear bond forming differences (creep differences) are observed over short intervals (< 3 meters) as well. However the attempt to analyze these intervals resulted in very varied results without clear or consistent patterns and they are thus not emphasized here. Probably the error associated with the TVD assumption is too substantial, to properly perform an analysis one should have a detailed overview of the geological layers etc.)

P&A Assessment for Well C.2

The main case is the abandoned (but not plugged) well in the Martin Linge field located deeper and under the Frigg field. Performing a conventional P&A operation (e.g. section milling, perforate wash and cementing or similar) could be complicated, time consuming and expensive, creating motivation for investigating the possibility of potential annular barriers created by the shale sections between the completion and 9 7/8" casing shoe. (Note that no CBL was ran on the 9 7/8 casing cement (DM#1068210, internal document))

1.17 General Case Details

The 102 meter (MD) long 8.5" section from the 9 7/8" casing shoe to top of reservoir is completed with 5.5" premium screens and filled with OBM, see Figure 0.1and Figure 0.4. Cementing through the premium screens is expected to be complex and challenging. According to the lithology log the interval consists of three different shale formations, Corner Knoll, Draupne and Heather shale. According to (DM#1068210) the shales are described as "nominally impermeable" and their stability as "questionable". The hydrostatic column of gas (assuming reservoir virgin pressure) is less than the fracture closuring pressure (FCP) all the way up to the 9 7/8" casing shoe (equal at 48 m TVD / 52 m MD above shoe), meaning that the strength of the formation at current time fulfills NORSOK requirements. From lithology log average inclination is 35-30° but for simplicity in the proceeding calculations it will be considered as a vertical well with a stress regime as shown below in Figure 0.2.

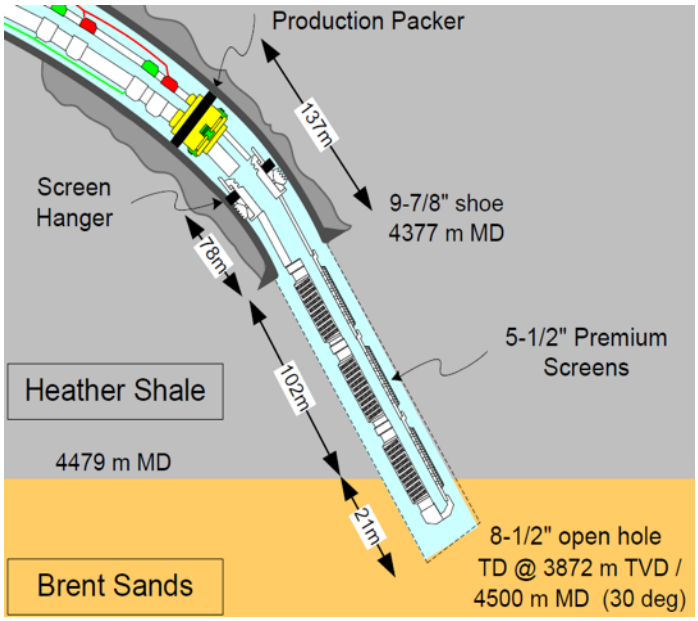

Figure 0.1:General details about the well completion

Well :	30-4-D-1AH				
Depth	4257.708	MDRT	3693.64074	TVDRT	

Bar	Stress XX	YY	ZZ	PP
1/1/2016	765.59	774.06	779.31	715.28
1/1/2020	754.72	769.28	783.26	715.28
1/1/2025	751.78	767.94	780.57	715.28

Source : 3D Geomechanical Model PetrelRGML2013 Case3_36

Figure 0.2:Stress regime for different times taking into account the effects from reservoir production

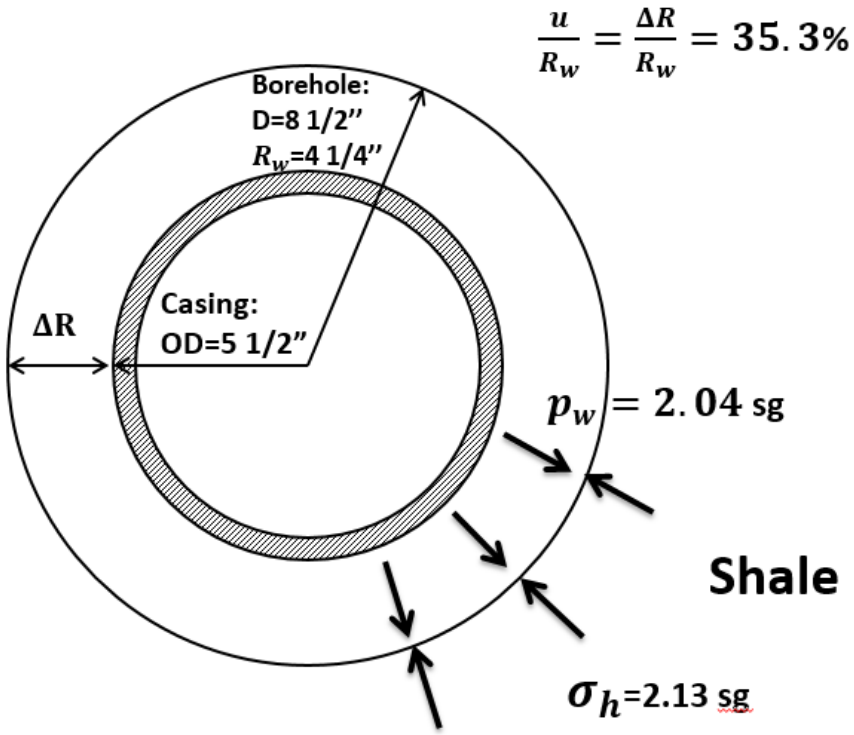

Figure 0.3: Borehole, screen geometry and drilling fluid details (based on lithology log")

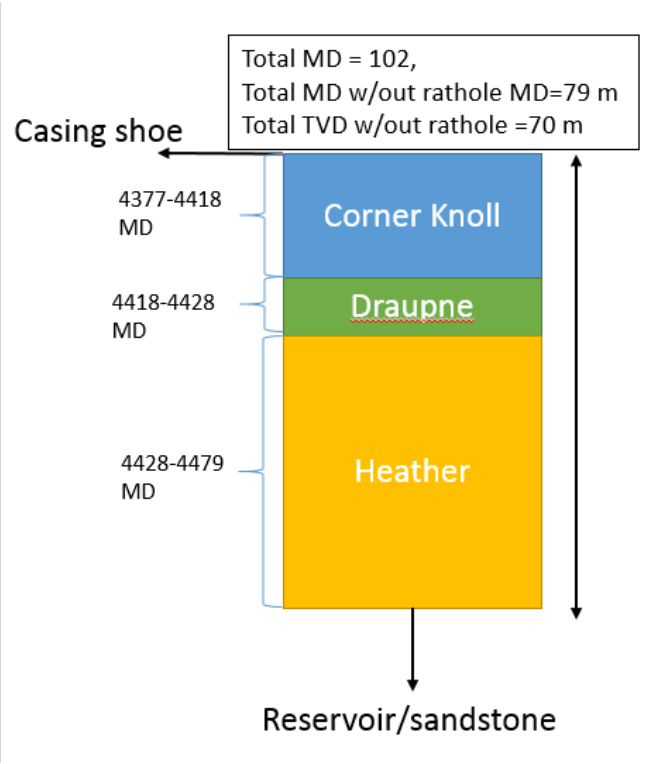

Figure 0.4: Shale formation in the interval between 9 7/8" casing shoe and top of reservoir (based upon lithology log)

1.18 Corner Knoll and Draupne Assessment

Based upon the lithology log for the relevant welltrack (Well C.2) (comparing the descriptions from lithology logs from different wells reveals some small inconsistencies, the relevant welltrack is emphasized most).

1.18.1.1 Corner Knoll

Is described as strongly carbonaceous, slightly silty, moderately firm, and partly calcareous. Stringers of lime stone are observed in the deeper intervals close to Draupne, limestone does not creep. Without much details, this section does not appear to have material characteristics of a strongly creeping shale. Furthermore, the majority of this is formation is in the rathole and the lower section which is not contains limestone stringers. It is believed that its contribution to forming a barrier will be minimal.

1.18.1.2 Draupne

Is described as medium hard, carbonaceous, very slightly to non-calcareous. Has been known to from barrier (Statoil). Could contribute to forming a barrier, but the interval is very short and the formation of an adequate barrier relies on the Heather formation.

1.19 Heather Shale Composition

The mineral composition is based on XRD analysis on cuttings from Well D. It is worth noting that the samples maybe are contaminated with Barite from the drilling fluid. The composition can very roughly be described as (see also Figure 0.5 and Figure 0.6):

- 4.6-41% (average 23%) Carbonate, mainly calcite (assuming all barite is from drilling fluid contamination, average becomes ~27.25%)
- 9.5-21.7 % (average 15%) Quartz (without barite, average becomes ~17.8%)
- 10.8-45.8% (average 31.9%) Clay, see Figure 0.5 for clay mineral composition (without barite, average becomes ~37.8%)

The clay minerals are shown to have the largest effect on creeping capacity, and are therefore the main interest. The detailed composition of the clay fraction for the different samples is displayed below in Figure 0.5:

MINERALOGICAL COMPOSITION OF CLAY FRACTION (<5 µm) *(Clay percentages are estimated visually from XRD patterns)*				
Smectite *(%)*	**Interstratified Illite/smectite Ordered R1 or R3** <15% Smectite *(%)*	**Illite and/or micas** *(%)*	**Kaolinite** *(%)*	**Chlorite** *(%)*
0	60	10	20	10
0	40	10	40	10
0	70	10	15	<5
0	60	10	30	Trace
0	50	10	35	<5
0	65	10	20	<5
0	35	15	45	<5
0	40	10	50	Trace
0	30	20	50	Trace
0	30	20	50	0

Figure 0.5: Composition of clay fraction in Heather

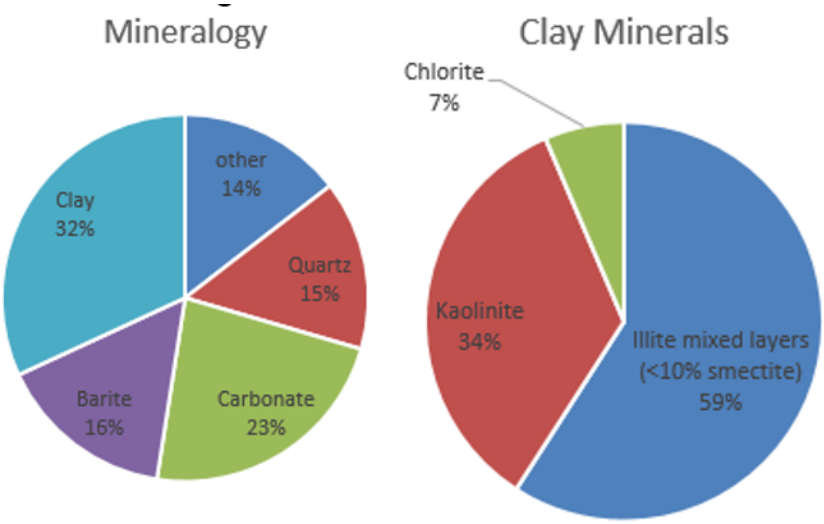

Figure 0.6: Composition based on average values from cuttings for the relevant depth

Based on experiences from Statoil the composition (see section 1.19) this shale contains too much carbonate and in many intervals too little clay minerals (in particular smectite) to from good barrier. Statoil's preliminary findings on mineralogy is shortly described below (Carlsen, 2017), see Figure 0.7:

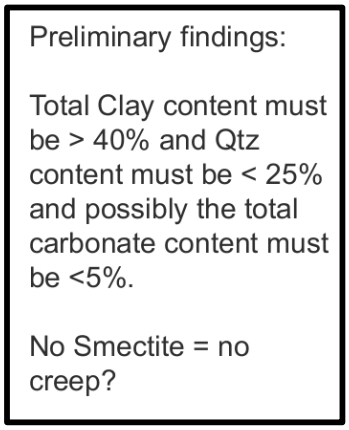

Figure 0.7: Statoil on mineralogy (Carlsen, 2017)

There is no pure smectite in the clay composition and only small amounts in the interstratified illite-smectite layers (<5% mass). Indicating that for the given in situ conditions (high temperature and pressure) the smectite to illite conversion has been going on for some time. This reaction may produce significant amounts of micro-quartz cement, reducing porosity and increasing density (Bjorlykke, 2013) (Inoue, et al., 1988)). Smectite has a strong link to the shale barriers formed on the NCS, the lack of smectite and abundance of carbonates compared to previous successful cases is not considered a positive indication. No pure smectite, but significant amounts of Kaolinite should indicate a relatively low porosity, consolidated shale, based on the tendencies observed in for example (Mondol, et al., 2008).

No strongly swelling clay minerals in addition to the use of OBM means no significant chemical effects should be expected.

1.19.1 Comparable Materials

The calculated porosity is in the range of 11-21% and averages around 16%. This is based on all the pore space being filled with brine, grain density from the XRD analysis and bulk density measured in the creep test. Barite contamination is suspected in the XRD analysis, but no amounts are known for the creep sample. The actual in situ porosity may be expected to deviate from this estimation. Compared to the studied creep test materials, Heather is found to be most comparable to the Opalinus Clay and Callovo-Oxfordian argillite. However, it should be noted that there is generally significantly less clay minerals in the Heather shale. The most similar composition-wise from the SINTEF project is the Pierre shale. Again, there is generally less clay minerals and as mentioned the Pierre shale is an outcrop. Based on empirical log values (see Figure 0.8) and a strength test (see Figure 0.14) the Heather shale is also significantly stronger and stiffer shale than the other investigated shales. Below is a table comparing some key values for different shales (Su, 2013), see Figure 0.8.

Type of shale	depth	Rho	Porosity	Clay	Creep rate at 25°C	Creep rate at 80 °C	Creep rate at 120 °C	E	C	Phi
	(m)	(g/cc)	(%)	(%)	(1/hr)	(1/hr)	(1/hr)	(MPa)	(MPa)	(°)
Boom Clay	250	2.03	39	23-59	4~5x10E-05	4~5x10E-04 (50°C)	-	300	0.5-1.3	18-25
Hordaland	1500-2000	2.18	30-40	40-70	-	6.3x10E-05	-	~4000	-	-
Opalinus Clays	650	2.45	18	49	1.0x10E-06	2.9x10E-06	-	3000~6000	3	25
Callovo Oxfordian Clay	490	2.45	18	45	0.2~0.4x10 E-06	1.3x10E-06	-	5500	6	28
Heather	3700	2.56	10-20	20-40	-	-	1.6-2x10E-7	7200	-	-
Tournemire	250	2.55	9.5	55	1.6x10E-07	-	-	9300-24000	6	28

Figure 0.8: Comparisons of creep rates for the some investigated shales. Creep rate on Hordaland shale is based on conservative estimates from the closing of the annular gap in well A. Creep rate in Heather is based on the creep test discussed in section 1.20.

1.20 Discussion of Heather Shale Creep Test

A creep test on a cylinder sample from the Heather formation was performed by the University of Lille. The creep test is performed under drained conditions and high temperature (120°C). The general creep procedures are shown below in Figure 0.9.

- ✓ The sample is subjected to a hydrostatic stress, proximately equal to the in situ horizontal effective stress, say $\sigma_h^{'} = 8MPa$;
- ✓ One measures the creep deformation at this stress state until the;
- ✓ The lateral stress (confining pressure) is decreased (from 8 to 1, by three steps of 2MPa and one step of 1 MPa), and one increases the axial stress with the ratio $\Delta\sigma_{axial}^{'} = -2\Delta\sigma_{lateral}^{'}$, so that the mean effective remains unchanged;
- ✓ At each stress step, the creep deformation is measured (until the stabilization is obtained if the secondary or tertiary creep does not occur);
- ✓ After the creep test, the sample is loaded until failure in conventional triaxial compression with a confining pressure of 1 MPa.

Figure 0.9: Load steps and procedure in creep test.

As a consequence of drained conditions the observed deformation is likely a result of several mechanisms and not just creep, such as for example consolidation effects. Drained conditions mean pore fluid is allowed to escape and the high temperature could lead to evaporation of pore water, which most likely increases the pore fluid escape. As a consequence, it is challenging to distinguish the deformation stemming from creep from other displacement mechanisms. Nevertheless, in an attempt to give estimates of when, or if, one can expect a barrier to form in the Heather formation some more or less realistic assumptions simplifying the analysis will be used. The result show axial compression and lateral expansion, see Figure 0.10. The core sample is first consolidated isotropically at 8 MPa effective stress before different deviatoric load steps are applied as seen in Figure 0.11.

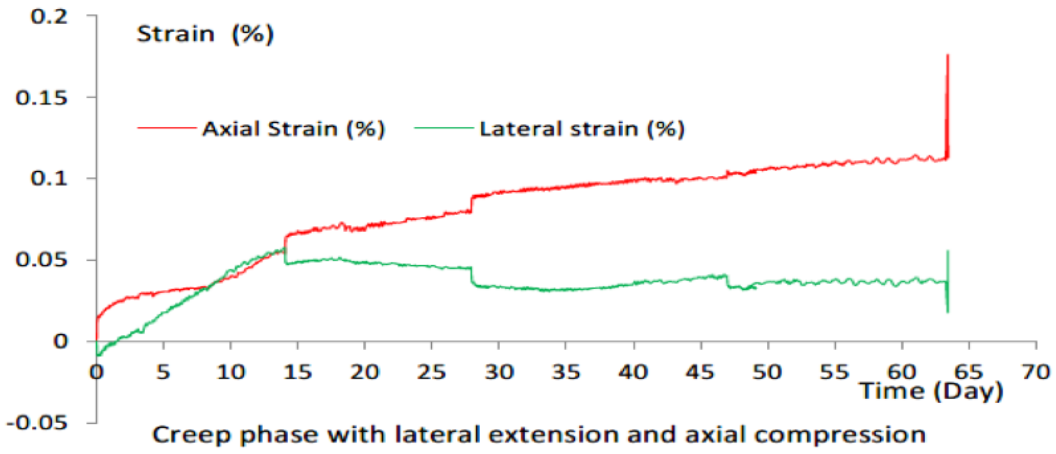

Figure 0.10: Evolution of axial and lateral strains with time during the phase of deviatoric creep

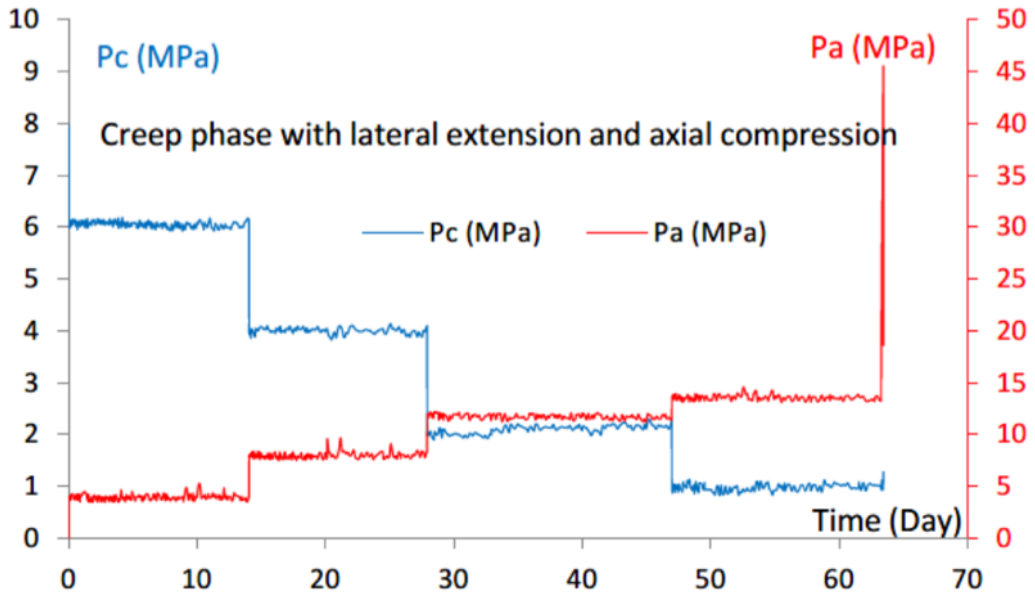

$$(P_a = \sigma_{axial} - \sigma_{lateral} = \sigma_{axial} - P_c)$$

Figure 0.11: Load steps for the creep test

The deformation after the first load step is assumed to mainly be a result of further consolidation effects, in other words pore fluid escape which leads to compression both laterally and axially. Significant porosity reduction is not assumed unrealistic as the pore fluid leaving the sample is likely stimulated by the high temperature, potentially also evaporating the water. The in-situ total pressure is larger and thus a higher boiling point can be expected for the in-situ pore water, in the lab experiment however the pressure might not be high enough to avoid water evaporation and thus larger effects from pore fluid drainage. For the proceeding load steps the sample clearly displays axial compression and lateral extension. The main part of the deformation happens rapidly (elastic deformation), but some varying time-dependent effects can clearly be seen. The measured creep rate, or rather deformation rate, is shown below in Figure 0.12

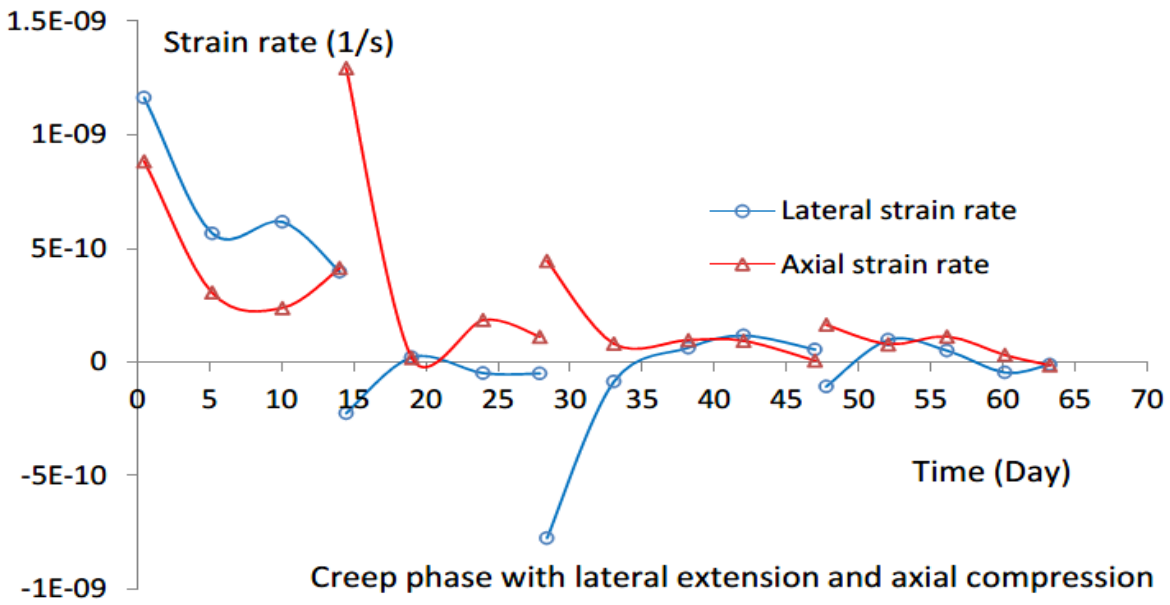

Figure 0.12: Rate of deformation shown for different times

The creep/deformation rates appear to be considerable, although there are several factors that has to be taken into account. One is that the sample was strongly cracked before the creep test commenced, see Figure 0.13. Like mentioned, it is hard to separate the creep deformation from deformation stemming from other mechanisms. Under the assumption that steady state phase of creep was only reached for the two longest lasting load steps (12 and 14 MPa), after which much of the least trapped/easily escapable pore fluid could have left the sample. The average creep rate based on the four last measurements of the two last load steps gives an axial creep rate of $\sim 5 * 10^{-11}\ 1/s$ and a radial creep rate of $1.85 * 10^{-11}\ 1/s$. This is one order of magnitude lower than the tendency measured for the Oxfordian Argillite for example (see Figure 0.5). Considering these creep rates are for a strongly cracked sample under higher deviatoric loadings and temperature it shows that the even though the composition and porosity is comparable, the Heather shows considerably lower creep rate.

An interesting effect is that the sample creeps at a lower rate for higher deviatoric loadings, creep hardening, this is contradictory to general creep behavior and theory and further indicates that other displacement mechanisms are significant. Potentially this effect can also be linked to the carbonate content as the same creep hardening effect was observed by (Rassouli & Zoback, 2017) in creep tests for very carbonate rich shales. It can also be linked to the threshold for reaching steady state creep phase was not reached (although this is somewhat contradicted by the low deviatoric in situ stresses). Possibly, sufficient time was not given for the sample to reach steady state creep rate, suggesting that the sample was still in transient stage. This would indicate that an even lower steady state creep rate should be expected. In any case, the creep

hardening phenomenon is not deemed positive for potential altering of the in-situ conditions, i.e. reducing the annulus pressure in order to stimulate barrier forming as shown in for example the SINTEF project.

After the final creep stage the sample was axially loaded with 1 MPa confining pressure until brittle failure at 45.5 MPa with less than 0.2 % axial strain, see Figure 0.14 and Figure 0.13. The Heather sample is thus, despite being strongly cracked, a relatively strong shale. Which again is generally shown to be negative for creeping applications.

Figure 0.13: Core sample before (left) and after (right) the test. The sample is cracked before being tested.

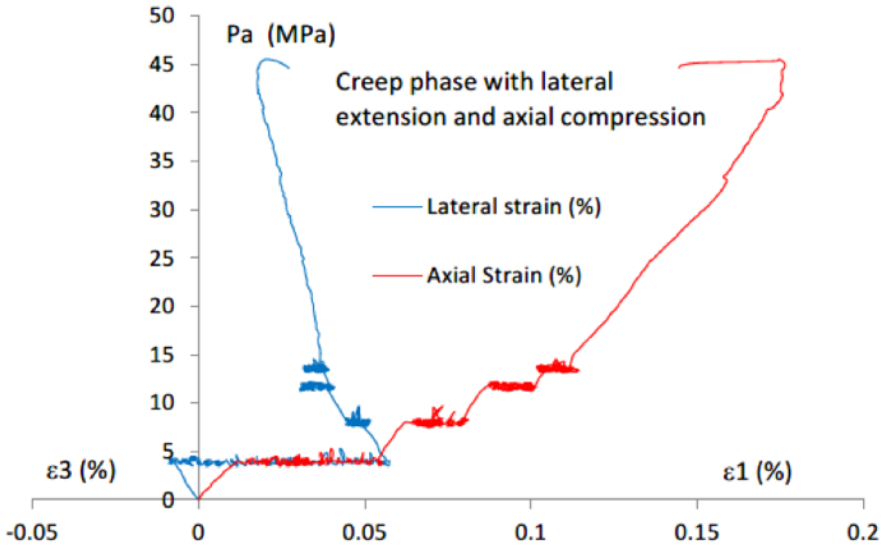

Figure 0.14: Axial and lateral strains versus deviatoric stress during the creep phase and final triaxial compression phase

1.21 Discussion on Heather Shale's Creeping Ability

Heather contains less clay minerals than the other creep test materials investigated, in addition to relatively large amounts of quartz and carbonate. No Young's modulus or other elastic properties are measured on the Heather sample (only empirical values based on logs), but degree of consolidation and quartz and carbonate content suggests a pretty stiff and strong shale.

Heather contains no pure smectite in the clay fraction, only small amounts in the interstratified illite-smectite layers (<5% total mass). Indicating that for the given in situ conditions (high temperature and pressure) the smectite to illite conversion has been going on for some time. This reaction may produce significant amounts of micro-quartz cement, reducing porosity and increasing density (Bjorlykke, 2013) (Inoue, et al., 1988)). The clay fraction has significant amounts of Kaolinite, following trends from (Mondol, et al., 2008) one can expect a considerable degree of consolidatio. From SINTEF's project it is seen that the smectite rich samples form barriers, while Pierre shale with little smectite (similar amount to Heather), does not form barriers despite massive persuasion. This is a negative observation, especially for potential creep stimulating operations such as reducing annulus pressure, increasing temperature or injecting fresh water.

The general trend of increased temperature showing increased creep is of great interest for the P&A case as the Heather formation has a temperature of ~133°C. It is not easy to determine the exact reason linking higher temperature to increased creep. If it is the reduced shear viscosity, it will have a positive impact on the Heather formation, but how much interstitial water which could be expected with such low amount of smectite is questionable. The effect for pore fluid expansion vs the solid matrix expansion is likely already at an equilibrium in-situ and for this to have any further effect a temperature increase is required. Already high temperature, lack of conventional tools for performing such a task, and the fact that the Pierre shale showed stiffening effects with temperature increase, should be considered before attempting to increase the temperature to stimulate creep.

In general increasing load leads to larger creep and creep rate. The opposite effect was observed for the Heather shale, for drained conditions where fluid is allowed to enter or leave the sample it could be linked to porosity reduction as sample (pore space) gets compacted. A similar trend was observed by (Rassouli & Zoback, 2017) in creep tests for carbonate rich samples, so another possible explanation could be linked to the relatively high carbonate content in Heather. Creep tests reveal that for some rocks there exists a threshold for creep while in other rocks it

does not (Fjaer, et al., 2008). This is hard to interpret for the Heather shale due to the drained conditions and the varying creep rates. Long enough time might also not have been given for the Heather to reach steady-state. But considering that the Heather shale is a relatively strong consolidated rock, a threshold for creep is not assumed unrealistic by the author, however the magnitude is hard to predict and might be considerably different between lab experiments and in situ conditions. The in-situ temperature might be beneficial in this case as it appeared to lower the threshold for some shales (see for example Boom Clay (Giruad & Rousset, 1996)), but then again these shales are not necessarily very similar to the Heather shale.

Chemical effects, such as salinity may also affect the viscosity in the interstitial water. But given that the drilling fluid in the Heather case is oil-based and lack of smectite leads the author to believe chemical effects to be very small in this case.

From what is covered here it shows that the lack of smectite and abundance of carbonates and quartz in the Heather formation are clearly expected to negatively affect its creeping ability. Available LWD data for Heather show average neutron porosity of ~30 and density of ~2.5, these values were relatively constant with depth (Well C, lithology log). This is much lower porosity measurements and higher density measurements than in Middle lark where neutron porosity consistently was 50+ and density less than 2.2. This is not unexpected as Heather is a much deeper formation and what is interesting is comparing the Heather values to the trends of the other overburden layers, sufficient data was unfortunately not available though.

On a positive note, low deviatoric stresses in-situ could indicate that the Heather has (or potentially used to have, before smectite conversion) low threshold for creep. In combination with the high pore pressure the disturbance created by drilling may have reactivated the creep.

1.22 Mathematical Predictions

Creep rates measured in lab experiments are generally higher (see for example section 1.11.4) than what is observed under in situ conditions. The extraction of shale core samples is not simple and significant damages occur, and in this case the sample was strongly cracked before the test, see Figure 0.13. Despite this and several other effects which has to be taken into account the results from the Heather creep test will be used together with some mathematical models in order to attempt to predict how the Heather formation will creep in the following section.

1.22.1 Conventional Creep Modelling

Based on curve matching typical creep tests a proposed formula for predicting strain can be given as (Jaeger, et al., 2008):

$$\epsilon = \epsilon_e + \epsilon_1(t) + Vt + \epsilon_3(t) \quad \textbf{0.1}$$

Where ϵ_e is the instantaneous elastic strain, $\epsilon_1(t)$ the transient creep, Vt the steady-state creep and $\epsilon_3(t)$ the accelerating creep. In order to model the steady-state creep which is of main interest, a popular approach is to assume a power law often similar to the form (Robertson, 1964) presented:

$$V = V_0 \left(\frac{\sigma}{\sigma_0}\right)^n \quad \textbf{0.2}$$

Where V_0 is a characteristic strain rate with the unit (1/s), $\sigma_0$is a characteristic stress and n is a dimensionless exponent which according to (Robertson, 1964) varies from 1-8. Based on creep being related to the diffusive motion of defects or dislocations, V_0 can according to (Jaeger, et al., 2008) be related to temperature T, free energy of activation Q and the gas constant R in the following manner:

$$V_0 = V_0^{\infty} e^{(-Q/RT)} \quad \textbf{0.3}$$

Where $V_0^{\infty}$is a hypothetical strain rate at infinitely high temperature. Many models (as can be seen later) take a similar form to the equations shown here.

1.22.2 Kun Su's Norton Power Law Model

Based on four different types of shale (many of which are covered in section 0) with data as shown in Figure 0.15 (minus Heather and Hordaland shale), the following Norton power law ($\dot{\epsilon} = A(\sigma_d)^n$) equations for relating creep to porosity (ϕ) and deviatoric stresses (σ_d) were suggested by Kun Su (Su, 2013)

For ambient temperature (25°C):

$$\epsilon^{\dot{v}p} = 7.23 * 10^{-16} * \sigma_d^{1.1364\phi + 1.1955} \left[\frac{1}{hr}\right] \quad \textbf{0.4}$$

At temperatures of 50-80 °C, the creep rate is about three times that of measured at ambient temperature for indurated shales and ten times for unconsolidated shale, see Figure 0.15. The following expressions were proposed for calculating creep rate at these temperatures

$$\epsilon^{\dot{v}p} = 2.17 * 10^{-15} * \sigma_d^{1.1364\phi + 1.1955} \left[\frac{1}{hr}\right], \; for\; T = 80\,°C \; and \; 0.1 < \phi < 0.2 \quad \textbf{0.5}$$

$$\epsilon^{\dot{v}p} = 7.23 * 10^{-15} * \sigma_d^{1.65} \left[\frac{1}{hr}\right], \; for\, T = 80\,°C \; and \; \phi = 0.4 \qquad \textbf{0.6}$$

Type of shale	depth	Rho	Porosity	Clay	Creep rate at 25°C	Creep rate at 80 °C	Creep rate at 120 °C	E	C	Phi
	(m)	(g/cc)	(%)	(%)	(1/hr)	(1/hr)	(1/hr)	(MPa)	(MPa)	(°)
Boom Clay	250	2.03	39	23-59	4~5x10E-05	4~5x10E-04 (50°C)	-	300	0.5-1.3	18-25
Hordaland	1500-2000	2.18	30-40	40-70	-	6.3x10E-05	← ~50-60°C	~4000	-	-
Opalinus Clays	650	2.45	18	49	1.0x10E-06	2.9x10E-06	-	3000~6000	3	25
Callovo Oxfordian Clay	490	2.45	18	45	0.2~0.4x10 E-06	1.3x10E-06	-	5500	6	28
Heather	3700	2.56	10-20	20-40	-	-	1.6-2x10E-7	7200	-	-
Tournemire	250	2.55	9.5	55	1.6x10E-07	-	-	9300-24000	6	28

Figure 0.15: Creep rate of different shales under a deviatoric stress of 2-5 MPa, as given by (Su, 2013), the Heather and Hordaland shales are included for comparison reasons. Note that the creep rate of the Hordaland shale is a conservative estimation based on the time it took before good bonding was observed in Well A.

It is important to keep in mind that the Heather creep test was performed under drained conditions and several displacement effects such as for example consolidation is probably involved. Nevertheless, based on the rough approximation made in section 1.20 it is found that these equations do not match very well for the heather material (they are overestimating creep rate). A new slightly altered solution is suggested to better fit the Heather creep rates:

$$\dot{\epsilon} = 2.3 * 10^{-16} (\sigma_d)^{1.1364\phi + 1.1} \qquad \textbf{0.7}$$

Under the assumption that the core sample's porosity is reduced during the test, it matches the creep rates measured for the three last stages to a certain degree, see Figure 0.16.

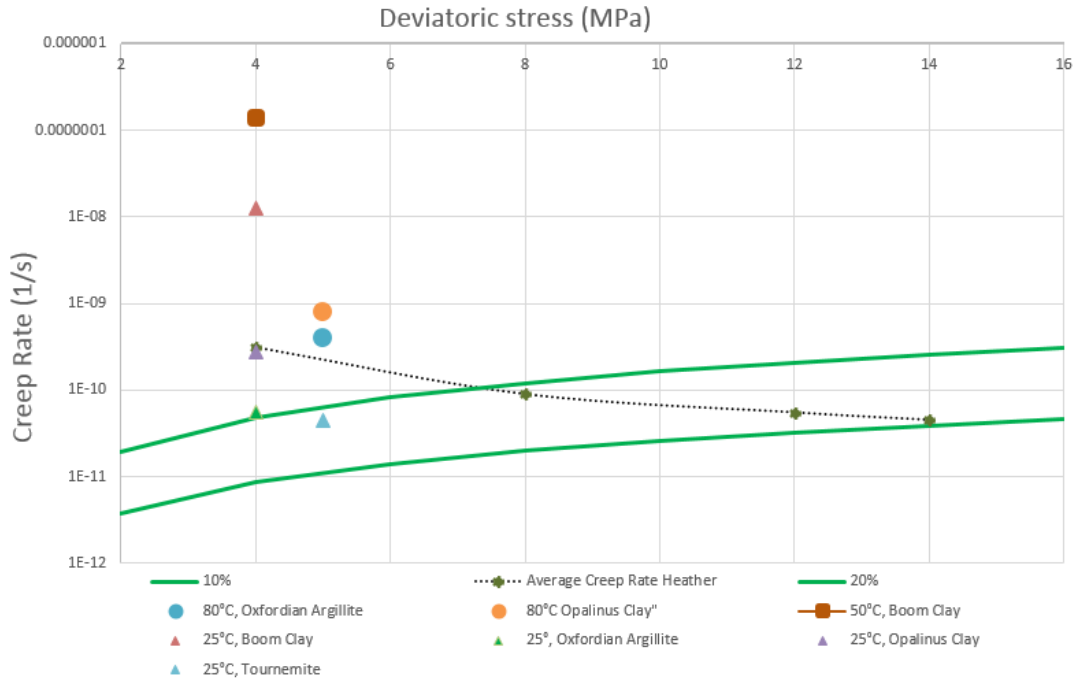

Figure 0.16: Creep rates for different materials under different deviatoric loadings. The power-law model for creep is also included for different degrees of porosity (10-20%). Keep the temperature difference for the different creep rates in mind.

There are of course a lot of uncertainties involved, for example as can be seen the somewhat abnormal behavior of the heather shale having lower creep rates at higher deviatoric stresses is not replicated by the equation. But without further creep tests or additional details it is questionable how accurate a calibration could be. Nevertheless, this new equation will be used in an attempt to predict time for a barrier to form in the Heather formation based on the following analytical solutions for borehole convergence problem.

1.22.3 Barker's and Liu's Solutions for Wellbore Closure

It is worth noting that generally, most analytical creep models for boreholes have been developed with the intention of preventing stuck pipe/casing due to borehole convergence during drilling operations. Thus, a conservative approach when deriving such models (leading to over-predicting borehole closure rate) could on the contrary be too optimistic in the case of predicting annular barriers. Furthermore, these solutions are analytical and the assumptions made when deriving them, while convenient mathematically, are not necessarily realistic.

In order to take into account the temperature difference between the lab and in-situ conditions an alternative way to write the Norton model is adopted and shown below:

$$\dot{\epsilon} = Ae^{-B/T}(\sigma_d)^n \qquad \textbf{0.8}$$

Where T is temperature B is temperature exponent and A is viscosity constant. Under the assumption that the creep rate for indurated shales at 80°C is three times the creep rate at 25°C

(Su, 2013), combined with power law suggested above, the B parameter is found to be 2102, and $A = 1.05171 * 10^{-13}$.

Barker derived a solution for wellbore closure in a linearly elastic rock (Barker, et al., 1994):

$$R = R_{w0} e^{\left[-\frac{\sqrt{3}^{n+1}}{4n-2} A e^{\frac{-B}{T}} (\sigma_{ro} - p_w)^n \Delta t\right]} \quad \textbf{0.9}$$

And Liu developed a similar solution but for an elasto-plastic rock (Liu, et al., 2011):

$$R = R_{w0} e^{\left[-\frac{\sqrt{3}^{n+1}}{2n^n} A e^{\frac{-B}{T}} (\sigma_{ro} - p_w)^n \Delta t\right]} \quad \textbf{0.10}$$

Where R is the current well radius, R_{w0} is the original well radius, T is temperature, σ_{ro} is the horizontal stress in the formation, p_w is the well pressure and n, A, B are material parameters. Assuming an in-situ porosity of 16% the closure rate is calculated and shown in Figure 0.17 below:

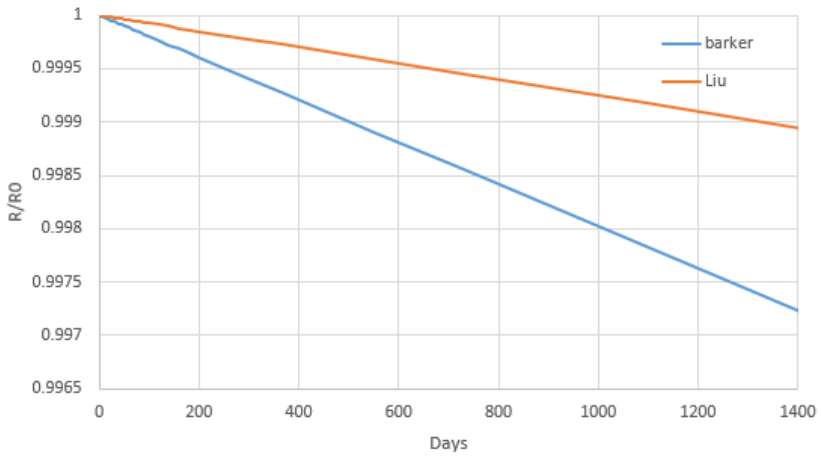

Parameters	Si units
Depth (m)	3693.65
Mud Weigh (sg)	2.040
R0 (m)	0.216
T°C	133
Farfield stress gradient	2.125
n	1.281824
B	2102
A	1.75261E-17
T (°K)	406
Sigh far field (Mpa)	76.95
P mud in the well(Mpa)	73.9

Figure 0.17: Barker's and Liu's solution for the inputs given to the right. The radius input displayed in the table to the right is actually the diameter, but this does not affect the result which is given in R/R_{w0}.

The results show that the Heather formation will not creep significantly (<0.5%) even after 1400 days (~3.8 years). For comparison reasons, the calculations based on the Boom Clay creep rate under 80 °C and for the same deviatoric stress is shown below in Figure 0.18:

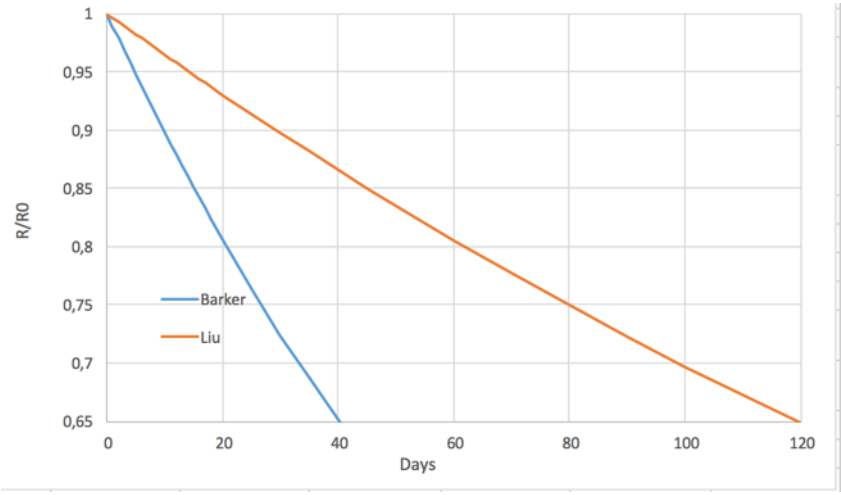

Parameters	Si units
Depth (m)	3693,65
Mud Weigh (sg)	2,040
R0 (m)	0,216
T (°C)	80
Farfield stress gradient (sg)	2,14
n	1,65
B (°K)	2102
A (1/s*Pa^n)	7,74E-16
T (°K)	353
Sigh far field (Mpa)	77,49
P mud in the well(Mpa)	73,9

Figure 0.18 Barker's and Liu's solution for the inputs given to the right. The radius input displayed in the table to the right is actually the diameter, but this does not affect the result which is given in R/R_{w0}.

According to Liu (Liu, et al., 2011) Barker's solution is known to overestimate the creep rate to some degree, depending on the n parameter. These results show that for even small values of n the two different solutions give significantly different creep rates. In order for these solutions to carry any weight, the material parameters must to be calculated with relatively good accuracy, this usually requires several creep tests, preferably also under undrained conditions. So not too much weight should be put on these, but also taking into account that the in-situ creep rate is usually lower than in lab experiments (see for example section 1.11.4), the calculations are not in favor of the Heather forming a barrier by creep.

1.23 Elastoplastic Model Results

Under the assumption that time dependent deformation of a downhole formation is governed by the effects of change in pore pressure and is not time dependent, the model derived can be used in order to predict the deformation in a wellbore. Unless specified the inputs used in the model are the same as shown below in Table 0.1. Again, note that the well radius is actually the diameter of the hole, but as long as the relationship between R_o and R_w is the same ($R_o = 5R_w$) the deformation in % will be exactly the same, so once again it is not of importance.

Table 0.1: Input values

$R_w\ [m]$	$R_o[m]$	$p_w[MPa]$	$\sigma_{ro}[MPa]$	$p_i[MPa]$	$p_o[Mpa]$	$E[MPa]$
0.2159	1.0795 ($5R_w$)	73.87	77.42	71.52	71.52	7218.7
ν	c	ϕ [°]	ψ [°]	α	c_p	
0.213	13	30	0	0.856	13	

Four different scenarios are inspected and their results are displayed in the figures below:

1. Initial deformation due to drillout (see Figure 0.19)
2. Inner pore pressure increased to initial well pressure (see Figure 0.20)
3. Well pressure decreased to initial pore pressure (see Figure 0.21)
4. Well pressure reduced until yield occurs (see Figure 0.22)

The results for the three first cases only result in elastic deformation and are as a consequence too small to carry much relevance in the P&A case. Failure is found to occur when well pressure is reduced to ~63.5 MPa assuming no pore pressure changes (lower pore pressure will require even lower well pressure). At this stage the well pressure is ~8 MPa lower than the pore pressure and it is pretty certain that for a real case tensile failure will occur before this stage. Thus the model appear have very limited use in predicting a barrier forming for this case. It could however be a useful tool should a hollow cylinder test be carried out on the Heather shale.

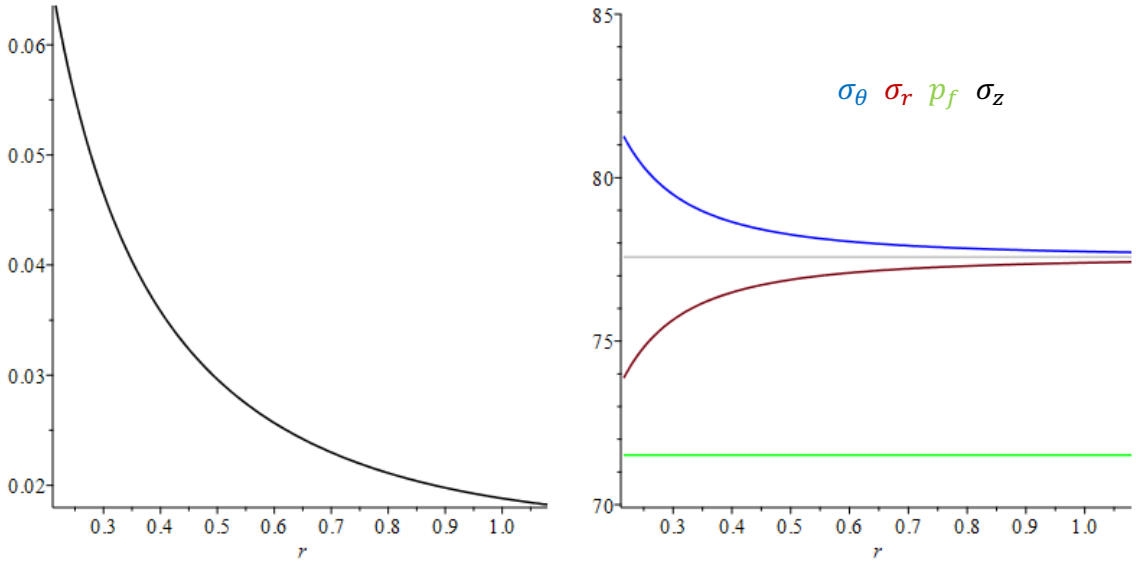

Figure 0.19: Displacement ($\frac{\Delta R_w}{R_w}$ in %) and stresses (MPa) for case 1

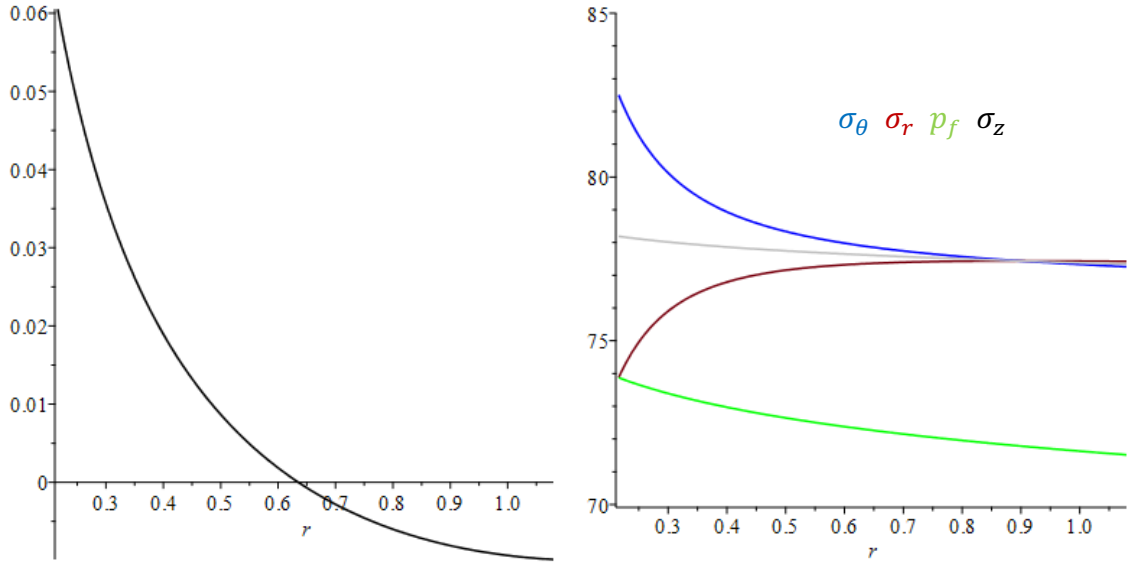

Figure 0.20: Displacement ($\frac{\Delta R_w}{R_w}$ in %) and stresses (MPa) for case 2

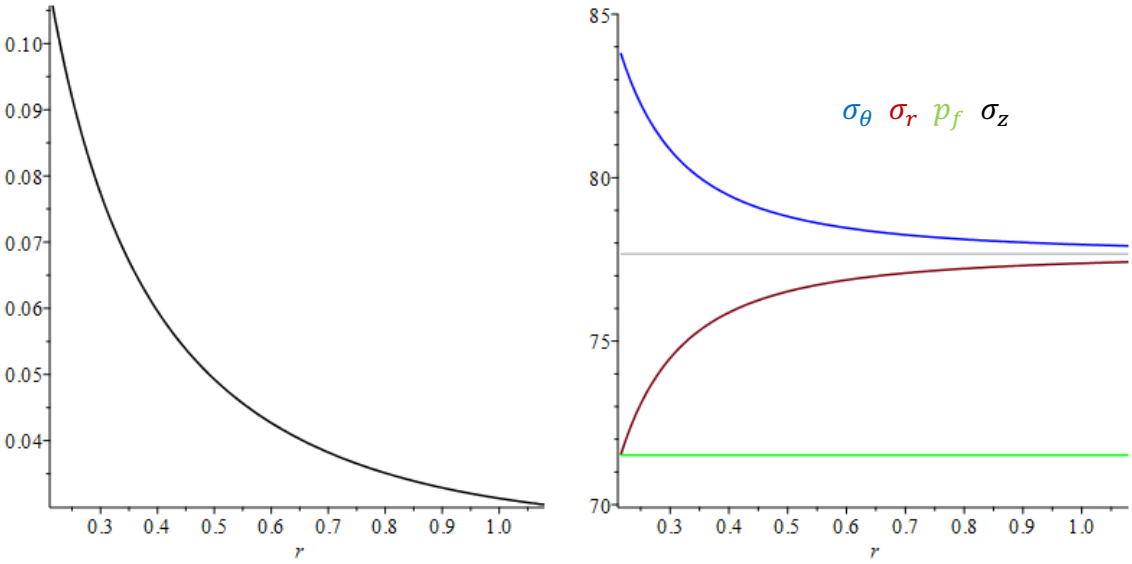

Figure 0.21: Displacement ($\frac{\Delta R_w}{R_w}$ in %) and stresses (MPa) for case 3

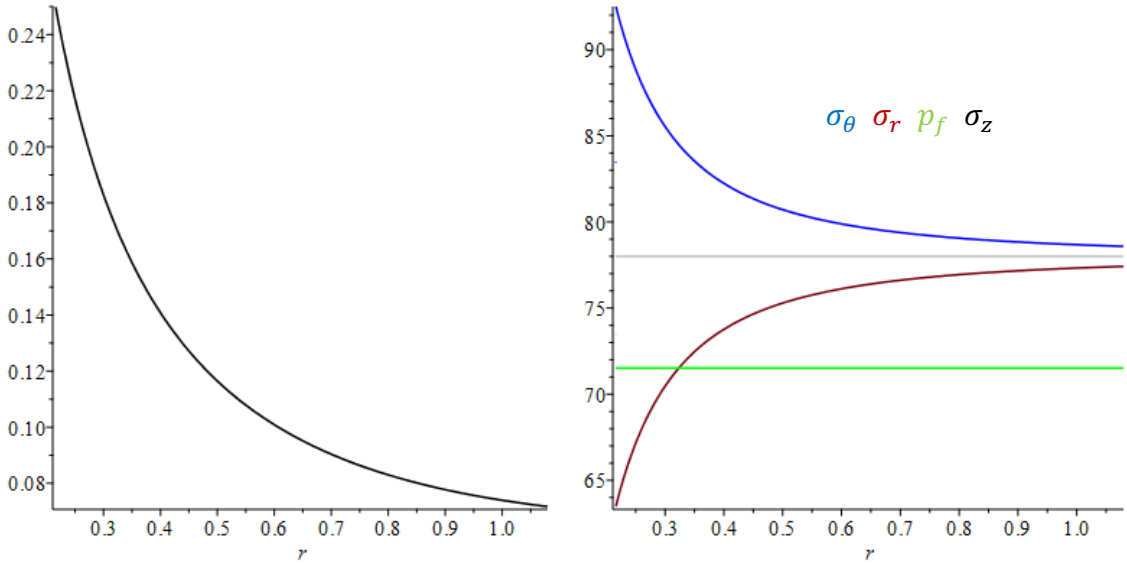

Figure 0.22: Displacement ($\frac{\Delta R_w}{R_w}$ in %) and stresses (MPa) for case 4

1.24 Numerical Modeling of Annular Space Closuring

The Heather shale creep is represented by two of the steady state components of the MDCF model see equation 0.11 (also known as the Munson Dawson model) (Munson, et al., 1990). The first component is "a dislocation climb mechanism" and the second is "an undefined (but empirically well specified) low stress and temperature mechanism". The third part related to "a dislocation slip mechanism" is considered negligible for this model. The equation then becomes (Munson, et al., 1990):

$$\dot{\epsilon}_c = A_1 \left(\frac{\tilde{\sigma}}{G}\right)^{n_1} e^{-Q_1/RT} + A_2 \left(\frac{\tilde{\sigma}}{G}\right)^{n_2} e^{-Q_2/RT} \quad \textbf{0.11}$$

Where:

$$G = G_0 - \frac{dG}{dT}(T - T_0) \quad \textbf{0.12}$$

$\dot{\epsilon}_c$ is the creep strain rate, $\tilde{\sigma}$ is the Von Mises effective stresses, T is the absolute temperature, R is the gas constant and $A_1, n_1, Q_1, A_2, n_2, Q_2, G_0$ and $\frac{dG}{dT}$ are material parameters. The Von Mises Effective stress is given by

$$\tilde{\sigma} = \sqrt{\frac{(\sigma_{11} - \sigma_{22})^2 + (\sigma_{22} - \sigma_{33})^2 + (\sigma_{33} - \sigma_{11})^2 + 6(\sigma_{12}^2 + \sigma_{23}^2 + \sigma_{31}^2)^2}{2}} \quad \textbf{0.13}$$

The material parameters used in this simulation are listed below in Table 0.2, and the creep rates as a function of the von Mises Effective stress are shown for three different temperatures in Figure 0.23:

Material parameter	A_1 $[1/s]$	n_1 $-$	Q_1 $[J/mol]$	A_2 $[1/s]$	n_2 $-$	Q_2 $[J/mol]$	G_0 $[GPa]$	$\frac{dG}{dT}$ $\left[\frac{MPa}{K}\right]$
Heather shale value	4.32E+28	4.397	2.39E+4	4.32E+28	4.397	2.39E+4	12.4	10

Table 0.2: Material properties used in the simulation

The geometry of the model is in 2 dimensions and it considers one fourth of the borehole in other words a 90°degrees angle intersection which due to simple geometry reasons is assumed to be representative for a complete borehole. By making this assumption/simplification the amount of running time used is reduced by a lot (nevertheless the running time is still several days).

1.25 Calibration

As mentioned it is challenging to calibrate the material properties based on one creep test, in particular under drained conditions. In line with what has been discussed earlier a very rough and rather optimistic (likely overestimating the creep) approximation is made. The values in Table 0.2 are represented by the yellow line in Figure 0.23, two other lines show the difference in creep rate for different temperatures:

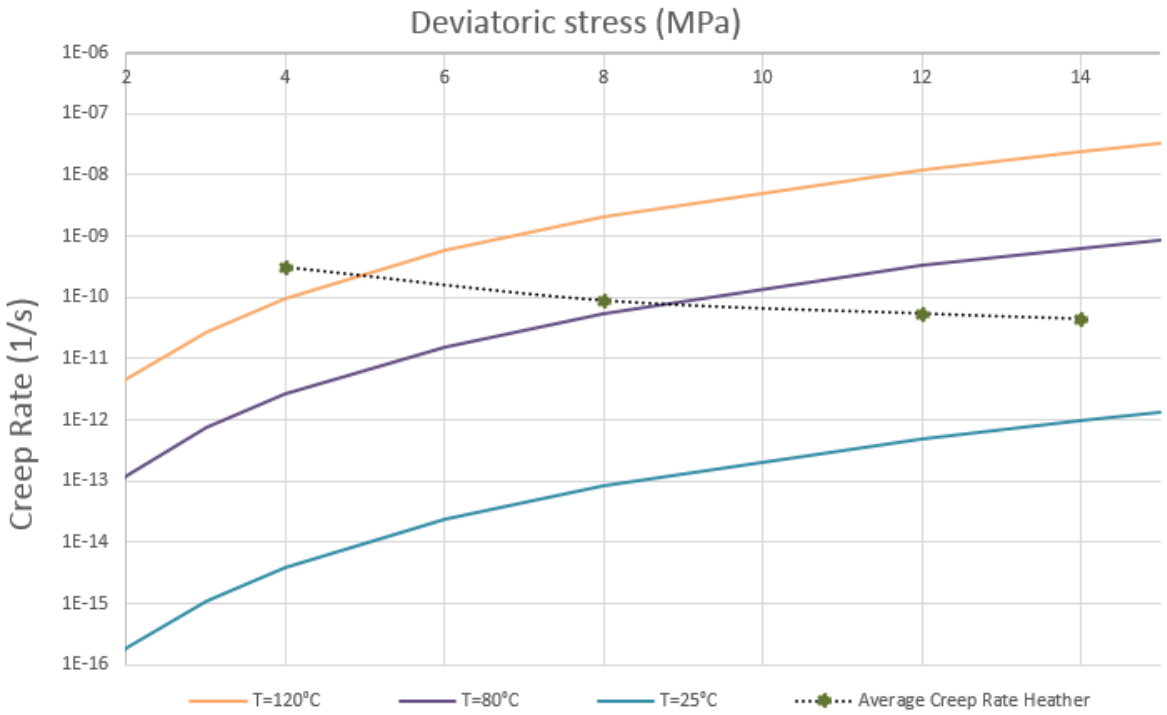

Figure 0.23: Quasi-steady creep rates vs deviatoric stresses for Heather shale sample and equation 0.11 for different temperatures (with parameters given in Table 0.2)

As can be seen from the graph the creep model and creep rates are not matching extremely well. The increase in creep rate as a function of temperature is probably also overestimated, see discussion in section 1.22.3. The difference in temperature from in situ and lab experiment is not great so the effect is probably not going to be large, nevertheless it is something that should be noted. Unfortunately, due to issues in the model and long running times this was not corrected. At the same time, there is large uncertainty associated with the steady-state creep rate determination so what is a proper calibration can be questioned. Nevertheless, the creep rate matches to some degree and, and should prove useful for predicting the general trend to some degree.

1.26 Results

The geometry is fixed in along the borders of x and y and the stress regime is shown in Figure 0.2. Please note that the wellbore was not properly scaled, the radius of the wellbore was set to 8.5”, this is the diameter of the actual wellbore, so 4.25” is the wellbore radius that should have been used.

The results show the development of the in-situ wellbore for 110 days. Three points in the vicinity of the borehole wall are chosen and investigated closer, see Figure 0.24.

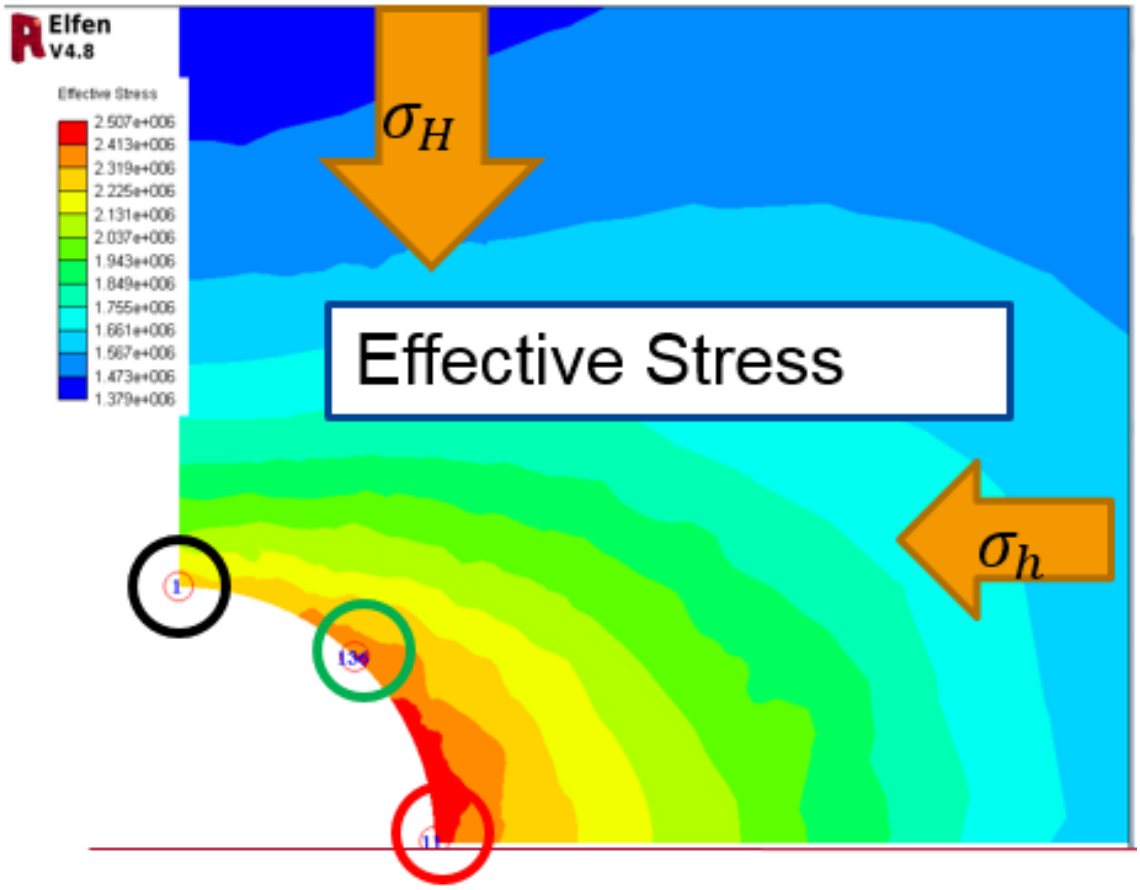

Figure 0.24: Von Mises effective stress (Pa) (as given by equation 0.13) after 110 days. The direction of the minimum (σ_h) and maximum (σ_H) horizontal formation stresses are also included.

The deformation in meters for these three points after 110 days are displayed in Figure 0.25 below. In addition, the deformation has been calculated in the strain convention used in this thesis for comparison reasons. Please note that 1 time unit equals 10 days in graphs below.

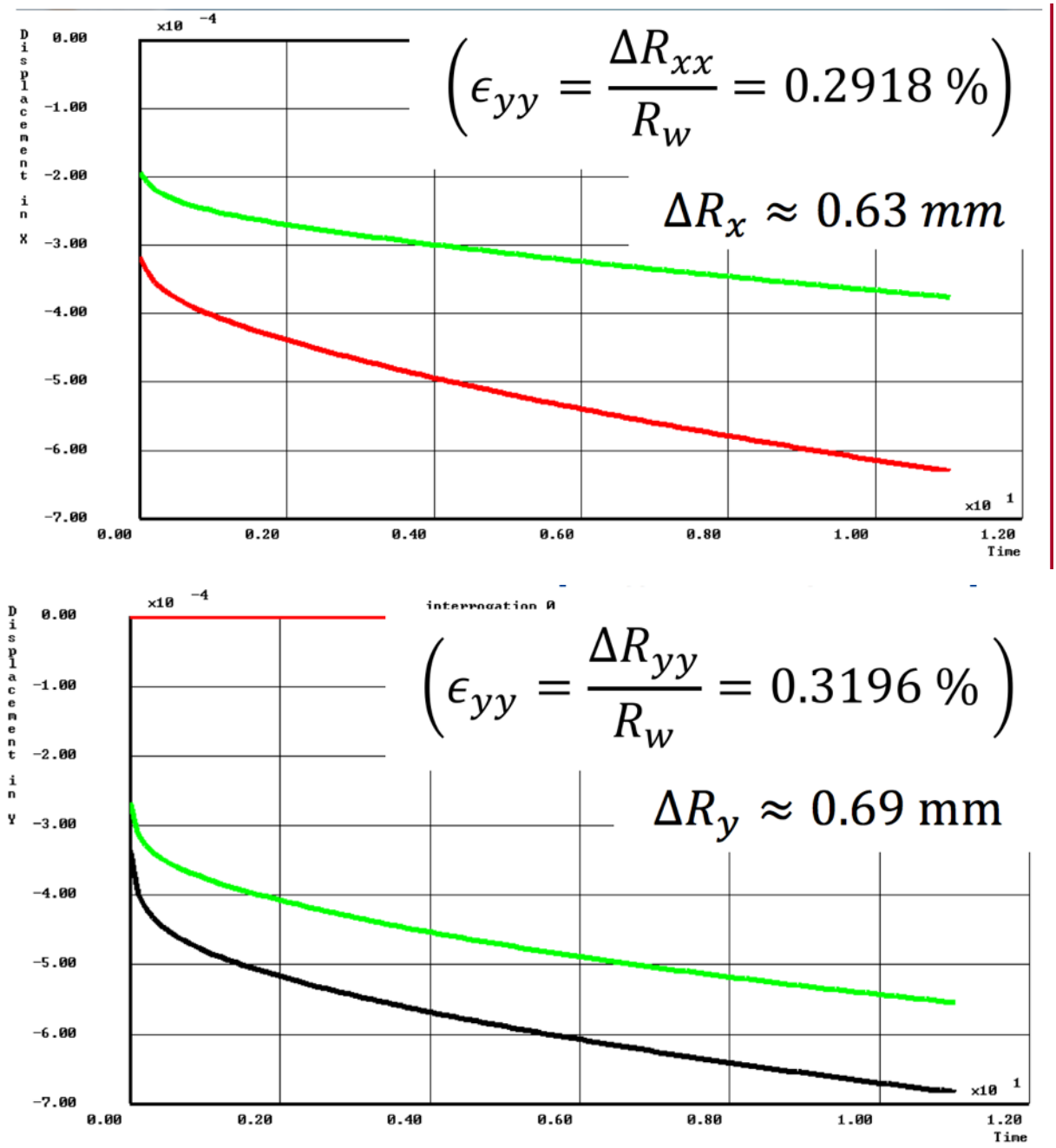

Figure 0.25: deformation in meters as a function of time (1 time unit equals 10 days).

Some other key properties are plotted versus time in the figures below:

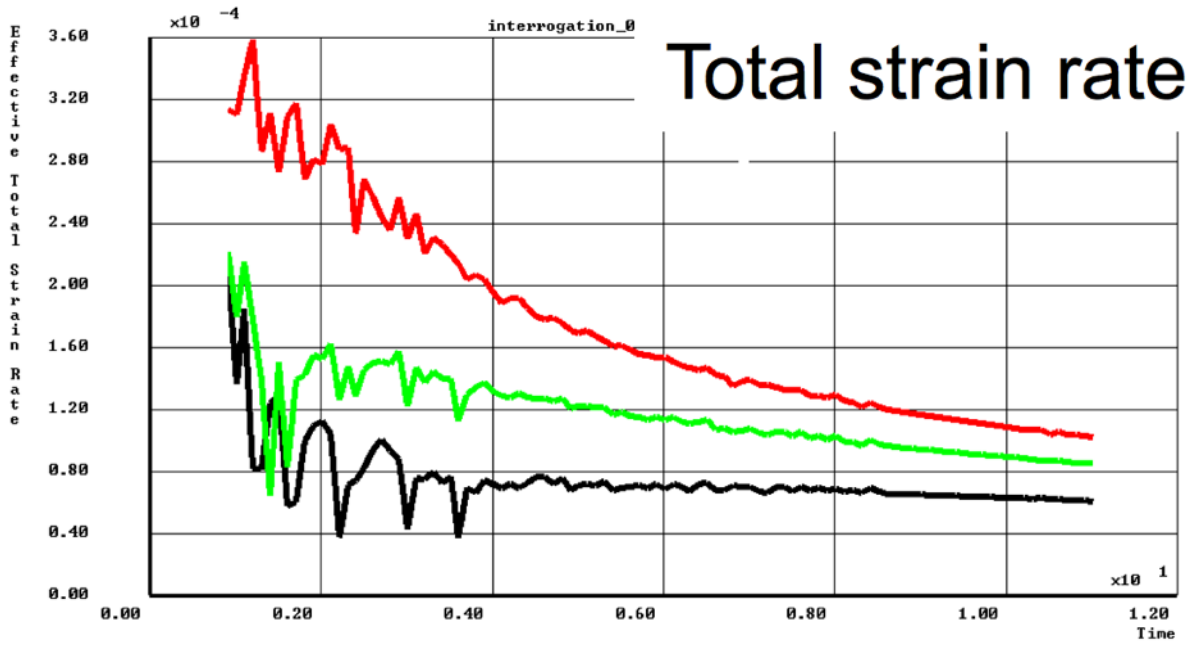

Figure 0.26: Total shear strain rate (contribution of elastic and plastic fraction) as a function of time (m/m*10day)

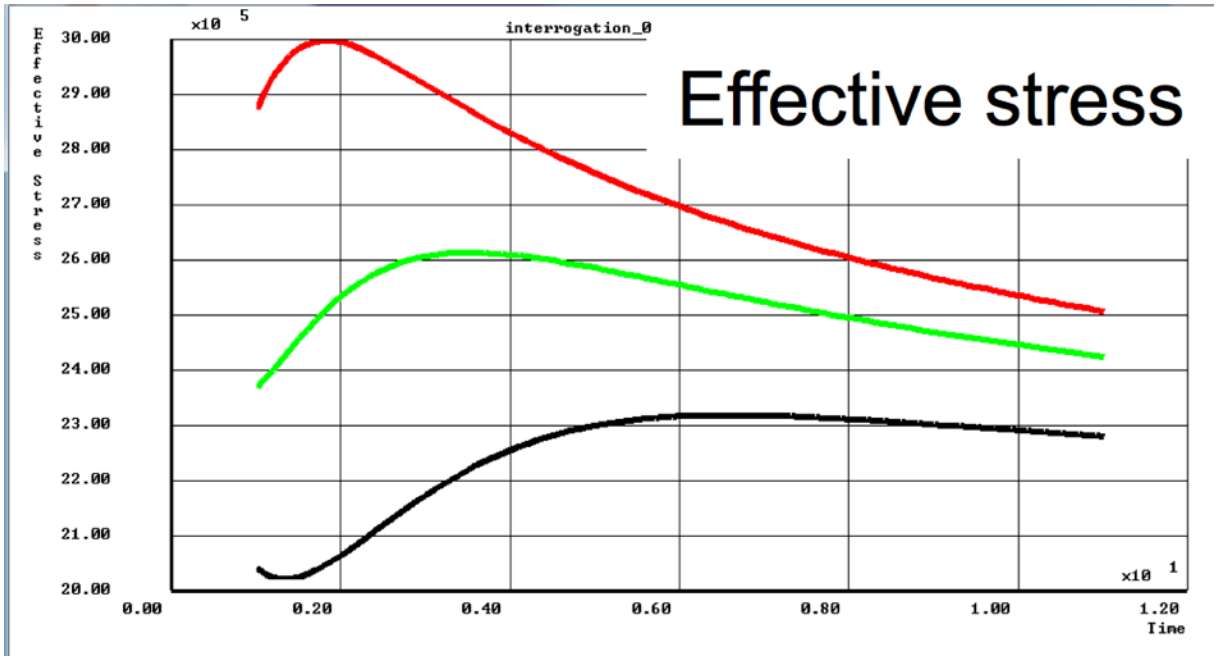

Figure 0.27: Von Mises Effective stress in Pascal (as given by equation 0.13) versus time

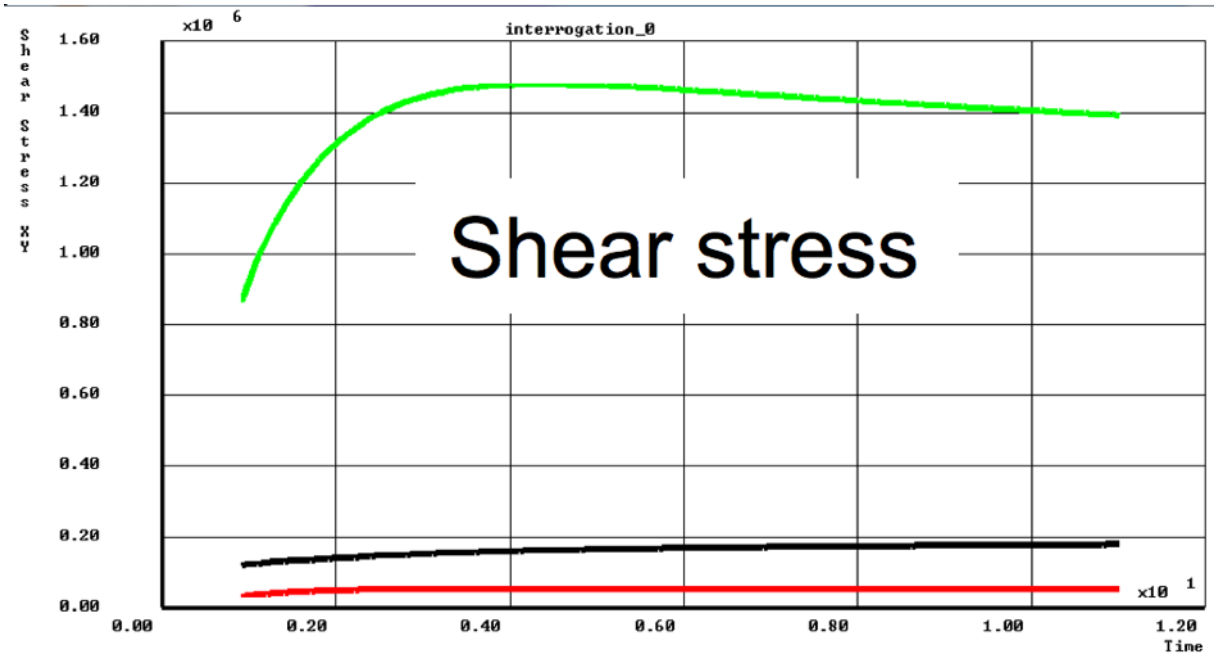

Figure 0.28: Shear stress (Pa) as a function of time

1.27 Discussion of results

The hypothesis: low creep rate and magnitude is expected based on analytical models, creep test and material. Questionable calibration could lead to overestimation of creep rate and magnitude.

During the 110 days, a general trend of stress arching is observed, see Figure 0.27 and Figure 0.28 (decreased shear and effective stress). As a consequence also the creep rate is decreasing, see Figure 0.25 and Figure 0.26, as the stress arching effects are in practice shielding the wellbore from the formations far field stresses. This might be enough to stabilize the formation and terminate the creeping process before a barrier is formed, perhaps even before first contact between formation and casing. There is observed no significant deformation compared to what is needed to form a barrier or impinge the casing, see Figure 0.25. Most shear strain or "total strain" is observed in the part of the hole which is parallel to the direction of the minimum horizontal stress. This is the part of the wellbore where shear failure eventually could occur. This is therefore not a surprising result, and it should not be mixed with or interpreted as wellbore convergence/inward radial displacement. Slightly higher porosity is observed in the near wellbore regions but the change is less than 0.5% (in total porosity) so no severe effects are expected or seen from the damaged zone.

For simplicity casing was not included in this simulation (not of importance as formation is always far from casing), but other simulations (Fjaer, et al., 2016) has indicated that once some part of the formation comes into contact with the casing it will provide support to the formation and significantly decrease creep. The radial convergence observed for this case is pretty similar for the different locations in the borehole, something which can be rationalized by the small difference in horizontal stresses. However as there is observed larger displacement in the Y-direction (parallel to the largest horizontal stress) it is tempting to believe that if contact with the casing happens, it will not be simultaneously for all the circumference. Thus, a similar effect could be observed in this case and further prevent an adequate barrier from forming.

Supported by the other measurements made, the creep rate and magnitude of the Heather shale appears to be limited. And not sufficient for barrier use in P&A. Forming any type of good bond will take significantly longer time than the relevant time window for this case. Some sources of error are mentioned below, but they are not expected to affect results to the degree of where it could change the final conclusion of a very slow borehole convergence and no proximity between formation and casing within the 10+ next years.

Estimation of first impact

In order to give a rough estimate on when the formation could contact the casing it is assumed that the average creep rate observed during the 110 first days remains constant until impact. Based on rough visual inspection the instant elastic contribution to the total displacement in Y-direction is around 0.31 mm, thus the deformation stemming from creep during the 110 days is approximately 0.38 mm. Extrapolating this creep rate gives first impact after ~60.2 years assuming casing radius is 5.5" (same scaling relationship as actual case: $\frac{Wellbore\ radius}{Outer\ casing\ wall\ radius}$).

This is most likely an overestimation of the deformation rate. During the 110 days the general trend shows a decrease in effective stress and shear stress, which will decrease the creep rate and magnitude. It is also a higher creep rate than what was observed in the lab on an already damaged sample. Still, the key observation is that it clearly shows the time before any contact between casing and formation is very long.

Some sources of error

- The wellbore radius in the model is 8.5", this is twice the real wellbore radius 4 ¼". This has been taken into account for all the calculations and predictions. It is hard to say

how much this scaling error affects the result, but the general trend of very slow hole convergence is not expected to be severely affected.

- The anisotropy of the shale characteristics is not captured in this model. This could for example lead to more heterogeneous creep behavior.
- The inclination of the well is not considered.
- Calibration could be done with more accuracy. (Although the creep behavior shown from the creep test does not match well with conventional creep models.)
- The calibration is likely overestimating the temperature effects on creep rate (based on previous observations of increased temperature on consolidated shales)
- The effects stemming from producing the reservoir below are not incorporated in the model due to running time and issues with the model earlier on.
- In this simulation there is no threshold for creep, as the model is based on salt. This might not be replicated in the real Heather shale.

1.28 Reservoir production effects

Long term reservoir depletion can affect the cap rock integrity, and cause shear movement along cap rock bedding planes potentially damaging the casing. It is not unthinkable that such effects could contribute to the closing of the annular gap and a shale barrier forming, and they should therefore be considered. As Martin Linge is produced numerical simulations show that the stress regime will change in the following manner, see Figure 0.29:

Well :	30-4-D-1AH			
Depth	4257.708	MDRT	3693.64074	TVDRT

Bar	Stress XX	YY	ZZ	PP
1/1/2016	765.59	774.06	779.31	715.28
1/1/2020	754.72	769.28	783.26	715.28
1/1/2025	751.78	767.94	780.57	715.28

Source :	3D Geomechanical Model PetrelRGML2013 Case3_36

Figure 0.29: Stress changes as a result of reservoir production

The numerical calculations show that the change in stresses during production stages of the Martin Linge field will have relatively small effects on the overburden stress regime. Unfortunately due to model issues which gave limited time this was not properly investigated in ELFEN. However, given the general trend of the calculations and simulations made, it is

expected to not sufficiently affect the displacement of the cap rock enough to matter for wellbore access or formation barrier in the relevant time window.

1.29 Conclusion on Heather P&A job

In short, despite some conditions traditionally convenient for creeping down in the borehole (high temperature and pore pressure), other observations from the creep test, mineralogy, analytical and numerical calculations all point towards a relatively stable formation which will not come close the completion screens anytime in the next ~20 years.

For barrier purposes the shale will probably not in any relevant time window deform sufficiently to form a 50 m MD long seal around the screenings. In addition the estimated closure of the wellbore is deemed small enough to not considerably alter the wellbore access in the next 10+ years. Thus the time for performing a conventional P&A operation should not be limited by the cap rock shale.

There exists some error and uncertainty related to the calculations made, the results do however very clearly point towards insignificant borehole convergence regarding wellbore access and formation barrier. The errors are also not of the type that would reduce the estimated creep rate e.g. optimistic calibration. For a more precise estimation/prediction additional creep tests should be carried out, such tests are currently ongoing.

Conclusion

Shale can in some cases close the gap between formation and casing wall and establish an annular barrier preventing migration of fluids in the annulus. This could in some cases replace traditional cement barriers and provide a convenient and cost-efficient solution to certain P&A operations.

Calculations show that shale has to undergo plastic deformation in order to displace sufficiently, and in most cases time dependent plastic (viscoplastic) deformation is required. Plasticity and creep in shales and other clay rich rocks is a fluid driven interparticle process depending on several rock parameters. Creep rate and magnitude of a shale depends heavily on both borehole conditions and material parameters. Experiments show that creep is more profound in weak unconsolidated shales, porosity is usually an excellent indicator for degree of compaction. Typically high amounts of clay minerals and small amounts of typical cementing materials like quartz and carbonate appears to enhance creep. Experience show that the clay mineral smectite is of particular importance, high amounts of smectite has a strong correlation with shales forming barriers. It is found that creep generally increases at higher temperature and higher deviatoric stress, and that rocks like shale display a significant amount of anisotropic creep behavior related to bedding planes and load direction.

A semi-analytical elasto-plastic hollow cylinder model for drained conditions has been derived and discussed. The model predicts onset of yield (plasticity) and radial displacement for vertical wells in homogeneous formations with an isotropic in situ stress and pore pressure. It can also be used for lab tests of hollow cylinder cores and shows relatively good accuracy when compared to a collapse test on a synthetic shale sample.

Some petrophysical log measurements can to some degree be linked to the creeping capacity of a formation. High porosity, low sonic velocities and density readings are potential indications to look for, if combined with high pore pressure it could potentially lead to a creeping formation.

Two different shale formations in the North Sea in wells drilled by Total E&P has been analyzed. The shale in the Hordaland group shows high creeping capacity and potential use as barrier, this matches well with trends observed from literature and available industry experience. For a deeper shale, numerical simulations, a creep test, mineralogy and analytical solutions and more show that despite some traditionally good conditions for creep (high temperature and pore pressure) this shale is not likely to creep sufficiently to form a barrier.

Nomenclature

CBL	Cement Bond Log
CEC	Cationic Exchange Capacity
FCP	Fracture Closing Pressure
ID	Inner Diameter
IS	Isolation Scan
LWD	Logging While Drilling
MC	Mohr-Coulomb
MD	Measured Depth
NABM	Non-Aqueous based mud
NCS	Norwegian Continental Shelf
NMR	Nuclear Magnetic Resonance
NP	Neutron Porosity
OBM	Oil Based Mud
OD	Outer Diameter
PAF	Plug and Abandonment Forum
P&A	Plug and Abandonment
PP&A	Permanent Plug and Abandonment
RDM	Radius Dependent Young's Modulus
SG	Specific Gravity
TVD	True Vertical Depth
UCS	Uniaxial Compressive Strength
WBM	Water Based Mud
XRCT	X-Ray Computed Tomography
XRD	X-Ray Diffraction

Bibliography

Al-Bazali, T., Zhang, J., Chenevert, M. E. & Sharma, M. M., 2009. *An Experimental Investigation on the Impact of Capillary Pressure, Diffusion Osmosis, and Chemical Osmosis on the Stability and Reservoir Hydrocarbon Capacity of Shales..* Aberdeen, UK, Society of Petroleum Engineers.

Anon., n.d. s.l.:s.n.

Anon., n.d.

Barker, J. W., Feland, K. W. & Tsao, Y. H., 1994. Drilling Long Salt Sections Along the U.S. Gulf Coast. *SPE Drilling & Completion,* 9(03), pp. 185-188.

Bjorlykke, K., 2013. Relationships between depositional environments, burial history and rock properties. *Sedimentary Geology* .

Carlsen, T., 2015. *Oseberg: Formation as barrier, Presentation for JIP group.* s.l.:s.n.

Carlsen, T., 2017. *Formation as barrier, SINTEF P&A Conference.* Trondheim: s.n.

Chen, X., Tan, C. P. & Haberfield, C. M., 2000. Numerical evaluation of the deformation behaviour of thick-walled hollow cylinders of shale. *International Journal of Rock Mechanics and Mining Sciences ,* 6(37), pp. 947-961.

Chen, X., Tan, C. P. & Haberfield, M., 1999. Solutions for the deformation and stability of elastoplastic hollow cylinders subjected to boundary pressures. *International journal for numerical and analytical methods in geomechanics,* Volume 23, pp. 779-800.

Chen, Z., 2016. *Clay Chemistry and its Application to Drilling Fluids, Course presentation for PTRL5024.* Sydney: University of New South Wales, School of Petroleum Engineering.

Conoco Phillips, 2015. *Creeping shale COP.* Trondheim: Sintef JIP presentation.

Darley, H. & Gray, G. R., 2011. *Composition and Properties of Drilling and Completion Fluids.* 5 ed. s.l.:Elsevier.

Detournay, E. & Cheng, A., 1988. Poroelastic response of a borehole in a non-hydrostatic stress field. *International Journal of Rock Mechanics and Mining Sciences & Geomechanics Abstracts,* 25(3), pp. 171-182.

Drucker, D. C., 1950. Some implifications of work-hardening and ideal plasticity. *Appl. Math.,* Issue 7, pp. 411-8.

Fakcharoenphol, P. et al., 2014. *The Effect of Osmotic Pressure on Improve Oil Recovery from Fractured Shale Formations.* The Woodlands, Texas, Society of Petroleum Engineers.

Fjaer, E., Folstad, J. S. & Li, L., 2016. *How creeping shale may form a sealing barrier around a well.* Houston, Texas, American Rock Mechanics Association.

Fjaer, E. et al., 2008. Petroleum Related Rock Mechanics 2nd edition. In: *Petroleum Related Rock Mechanics 2nd edition.* s.l.:Elsevier.

Giruad, A. & Rousset, G., 1996. Time-dependent behaviour of deep clays. *Engineering Geology 41,* pp. 181-195.

Grim, R. E. & Güven, N., 1978. *Bentonites: Geology, Mineralogy, Properties and Uses, Volume 24.* s.l.:Elsevier Scientific Publishing Company.

Hogg, H. & Davison, M., 2015. *SINTEF Shale Barrier JIP: Industry Experience Presentation - Shell.* s.l.:s.n.

Holt, R. M., 2016. *Borehole stability during drilling (Course Presentation for TPG4185 Formation Mechanics autumn 2016, NTNU).* Trondheim: NTNU.

Horseman, S. T., Higgo, J. J. W., Alexander, J. & Harrington, J. F., 1996. *Water gas and solute movement through argillaceous media,* s.l.: CC-96/1.

Hosford, W. F., 2005. *Mechanical Behaviour of Materials.* Cambridge: Cambridge University Press, The Edinburgh building.

Hoteit, N., Ozaman, O. & Su, K., 2000. *Geological Radioactive Waste Disposal Project in France: Conceptual Model of a Deep Geological Formation and Underground Research Laboratory in Meuse/Haute-Marne Site.* Seattle, Washington, American Rock Mechanics Association, pp. 1257-1264.

Hovda, L. & Holien, B., 2017. *Formation Creep.* Trondheim, Conference on Ocean Offshore & Arctic Engineering.

Inoue, A., Velde, B., Meunier, a. & Touchard, G., 1988. Mechanism of illite formation during smectite-to-illite. *American Mineralogist,* Volume 73, pp. 1325-1334.

Jaeger, J. C., Cook, N. G. & Zimmerman, R. W., 2008. Fundamentals of Rock Mechanics 4th edition. In: *Fundamentals of Rock Mechanics 4th edition.* s.l.:blackwell publishing.

Karpinski, B. & Szkodo, M., 2015. Clay Minerals – Mineralogy and Phenomenon of Clay Swelling in Oil & Gas Industry. *The Journal of Gdansk University of Technolog,* 15(1), pp. 39-55.

Kristiansen, T. G., 2014. *Quick Status Report from Valhall P&A.* Trondheim: SINTEF JIP presentation.

Kristiansen, T. G., 2015. *Why Shale Could be used as a Permanent Well Barrier Element.* Stavanger: P&A Forum.

Lebon, P. & Ghoreychi, M., 2000. French underground research laboratory of Meuse/Haute-Marne: THM aspects of argillite formation. *EUROCK2000,* pp. 27-31.

Liu, X., Birchwood, R. & Hooyman, P. J., 2011. *A new analytical solution for wellbore creep in soft sediments and salt,* s.l.: ARMA, American Rock Mechanics Association.

Li, X., Bernier, F., Vietor, T. & Lebon, P., 2009. *Thermal Impact on the Damaged Zone Around a Radioactive Waste Disposal in Clay Host Rocks.* s.l.:s.n.

Li, Y. & Ghassemi, A., 2012. *Creep Behavior of Barnett, Haynesville, and Marcellus Shale.* Chicago: American Rock Mechanics Association.

Mondol, N. H., Bjorlykke, K. & Jahren, J., 2008. Experimental compaction of clays: relationship between permeability and petrophysical properties. *Petroleum Geoscience,* Volume 14, pp. 319-337.

Munson, D. E., Fossum, A. F. & Senseny, P. E., 1990. Apporach to first principles model prediction of measured WIPP in situ room closure salt*. *Tunnelling and Underground Space Technology,* 5(1-2), pp. 135-139.

Naumann, M., Hunsche, U. & Schulze, O., 2007. Experimental investigations on anisotropy in dilatancy, failure. *Physics and Chemistry of the Earth,* Volume 32, pp. 889-895.

Nes, O.-M. & Fjær, E., 2015. *Time Dependent Borehole Stability: Effect of Static vs. Dynamic Mud Weight.* London, SPE/IADC Drilling Conference and Exhibition.

Norwegian Petroleum Safety Authority, 2013. *Standards Norway. Norsok standard d-010.* s.l.:s.n.

Norwegianpetroleum.no, 2017. *Activity on the Norwegian Shelf.* [Online]
Available at: http://www.norskpetroleum.no/en/developments-and-operations/recent-activity/
[Accessed 13 02 2017].

Pearson, F. et al., 2003. *Mont Terri project - geochemistry of water in the Opalinus clay formation at the Mont Terri project at the Mont Terri rock laboratory,* Bern: s.n.

Petrowiki, n.d. *Petrowiki.* [Online]
Available at: http://petrowiki.org/Lithology_and_rock_type_determination
[Accessed 15 June 2017].

Rao, S. M., Thyagaraj, T. & Rao, R. P., 2013. Crystalline and Osmotic Swelling of an Expansive Clay Inundated with Sodium Chloride Solutions. *Geotechnical and Geological Engineering,* 31(4), pp. 1399-1404.

Rassouli, F. S. & Zoback, M. D., 2017. *Multi-Stage Creep Experiments on the Wolfcamp Shale, Permian Basin, West Texas, USA.* San Francisco, American Rock Mechanics Association .

Risnes, R., Bratli, R. K. & Horsrud, P., 1982. Sand Stresses Around A Wellbore. *Society of Petroleum Engineers Journal,* 22(06), pp. 883-898.

Robertson, E. C., 1964. Viscoelasticity of rocks. In: W. R. Judd, ed. *State of Stress in the Earth's Crust.* New York: Elsevier, pp. 181-233.

Rousset, G., Bazargan-Sabet, B. & Lenain, R., 1989. *Time-Dependent Behaviour Of Rocks' Laboratory Tests On Hollow Cylinder.* s.l., American Rock Mechanics Association.

SINTEF Petroleum Research, 2016. *Shale as a Permanent Barrier after Well Abandonment.* Trondheim: s.n.

Skaug, M., 2016. s.l.:s.n.

Sone, H. & Zoback, M. D., 2013. Mechanical properties of shale-gas reservoir rocks — Part 2: Ductile creep, brittle strength, and their relation to the elastic modulus. *GEOPHYSICS,* 78(5), pp. D393-D402.

Sone, H. & Zoback, M. D., 2014. Time-dependent deformation of shale gas reservoir rocks and its long-term effect on the in situ state of stress. *International Journal of Rock Mechanics & Mining Sciences,* Issue 69, pp. 120-132.

Statoil, 2016. *Plug abandonment - an introduction (presentation).* [Online]
Available at: http://innovate.statoil.com/challenges/Pages/PlugAndAbandonment.aspx
[Accessed 2 October 2016].

Strand, S., 2001. *Øvinger i bore- og brønnvæsker, Øving 1 Leire.* City: University of Stavanger.

Straume, M., 2013. *Plug and Abandonment Forum (PAF).* Stavanger(Rogaland): Norwegian Oil Industry Association (OLF).

Straume, M., 2014. s.l.:Norwegian Oil INdustry Association.

Su, K., 2013. *Wellbore Instability Modes in Unconsolidated Shale (Technical Internal Report),* s.l.: Total E&P Azerbadjan.

Su, K., 2015. *Geomecha-considerations_Creeping.pptx.* s.l.:s.n.

Su, K., n.d. *Internal excel document.* s.l.:s.n.

Talabane, S., Chukwu, G. & Hatzignatiou, D., 1993. *Drilling Successfully Through Deforming Shale Formations: Case Histories.* Denver, Colorado: Society of Petroleum Engineers.

Total, 2016. *Total in Norway.* [Online]
Available at: http://www.total.com/en/norway
[Accessed 13 02 2017].

Truls Carlsen, S., n.d. s.l., s.n.

University College London, n.d. *Clays and Clay Minerals.* [Online]
Available at: https://www.ucl.ac.uk/earth-sciences/impact/geology/london/ucl/materials/clay
[Accessed 6 7 2017].

Williams, S., Carlsen, T., Constable, K. & Guldahl, A., 2009. *Identification and Qualification of Shale Annular Barriers Using Wireline Logs During PLug and Abandonment Operations.* Amsterdam, The Netherlands, SPE/IADC Drilling Conference and Exhibition.

Williams, S. M., Carlsen, T., Constable, K. C. & Guldahl, A. C., 2009. *Identification and Qualification of Shale Annular Barriers Using Wireline Logs During Plug and Abandonment Operations,* Amsterdam, The Netherlands: SPE/IADC Drilling Conference and Exhibition.

WolframAlpha, 2017. *WolframAlpha.* [Online]
Available at: https://www.wolframalpha.com/
[Accessed 18 July 2017].

Wyllie, D. C., 1999. *Foundations on Rock: Engineering Practice.* 2nd ed. s.l.:CRC Press.

You, S. et al., 2010. Medium resolution X-Ray computed tomography of hollow cylindrical samples of Boom Clay. *Rock Mechanis in Civil and Environmental Engineering,* pp. 755-788.

Yu, H. et al., 2015. Creep behaviour of boom clay. *International Journal of Rock Mechanics & Mining Sciences,* pp. 256-264.

Zeelmaekers, E. et al., 2015. Qualitative and quantitative mineralogical composition of the Rupelian Boom Clay in Belgium. *Mineralogical Society of Great Britain and Ireland* .

Zhang, C. & Rothfuchs, T., 2004. Experimental study of the hydro-mechanical behaviour of the Callovo-Oxfordian argillite. *Applied Clay Science 26,* pp. 325-336.

Zhang, C.-L., Rothfuchs, T., Su, K. & Hoteit, N., 2007. Experimental study of the thermo-hydro-mechanical behaviour of indurated clays. *Physics and Chemistry of the Earth,* pp. 957-965.

Zhang, C., Zhao, J., Zhang, Q. & Hu, X., 2012. A new closed-form solution for circular openings modeled by the Unified Strength Theory and radius-dependent Young's modulus. *Computer and Geotechnics,* Volume 42, pp. 118-128.

Appendix A: Clay structure and swelling

Clay minerals are key ingredients in shale composition and have significant influence on the behavior. Some basics about clay minerals as well as the chemical phenomenon of clay swelling which potentially can facilitate shale creeping, will be covered in this section.

Clay

Clays naturally occurs in a flake-like structure where one flake consists of 10-20 very small platelets (also called unit layer) bound together face-to-face by (usually) van der waals forces. A platelet is composed of tetrahedral and octahedral layers, see Figure 0.1 and Figure 0.2.

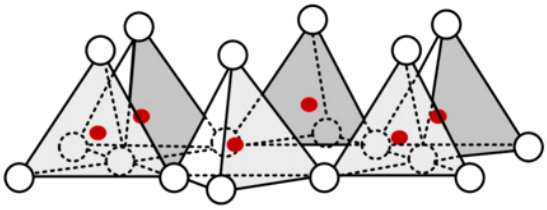

Figure 0.1: "Infinite" numbers of tetrahedra are linked together in a hexagonal base network, and forms a tetrahedral layer (Chen, 2016)

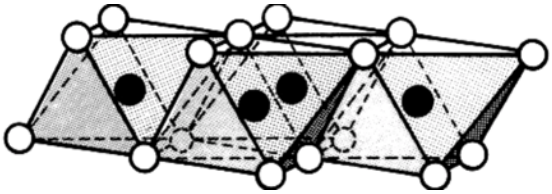

Figure 0.2: The octahedra are combined so that the corner of each octahedron in an octahedral layer is shared by three octahedra (Chen, 2016)

Each clay has a specific arrangement of these octahedral and tetrahedral layers in its platelet, see Figure 0.3. The bonds between the sheets in the unit layer are covalent and are strong and stable. Like mentioned, the bonding between the different unit layers is created by van der waal forces, and are therefore easily broken. Each tetrahedron contains a silicon (Si^{4+}) atom surrounded by four oxygen (O^{2-}) atoms. Each octahedron contains either a magnesium (Mg^{2+}) atom, or an aluminum (Al^{3+}) atom, surrounded by six oxygen (O^{2-}) or hydroxyl (OH^{-}) atoms. Aluminum dominated sheets are called Gibbsiteand and Magnesium dominated – Brucite (Fjaer, et al., 2008).

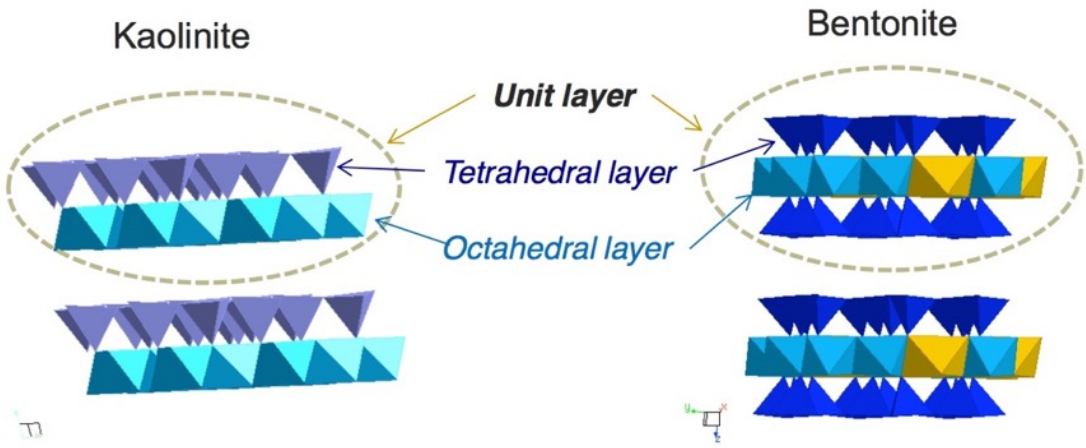

Figure 0.3: Unit layer composition of Kaolinite (1:1 clay) and Bentonite (2:1 clay) (Chen, 2016)

During the formation of clay minerals, some of the dominant atoms can be replaced by other ones, without changing the crystal structure substantially (isomorphic substitution). The type and degree of isomorphic substitution has big impact on the clay characteristics and practically results in an infinite number of groups and subgroups of clay. Common examples are: Si^{4+} atom is replaced by Al^{3+} or Fe^{3+}atoms in the tetrahedral layers, and Al^{3+} atoms in octahedral layers can be replaced by Mg^{2+} atoms (Strand, 2001) (Darley & Gray, 2011). This creates a charge unbalance, resulting in a negative charge on the basal surface. The charge deficiency is compensated by adsorption of cations. In the presence of water these cations can be exchanged with other cations, and are therefore known as exchangeable cations. The total number of cations adsorbed on the clay surface is called cationic exchange capacity (CEC) of the clay mineral and is a function of pH, crystal size and the type of cations (Karpinski & Szkodo, 2015). These atom substitutions lead some interesting effects, one of them is swelling of the clay.

Swelling Clay

Another term used for clay swelling is hydration. It refers to the adsorption of water that leads to an increase in both the surface area and bulk volume of clay. During drilling swelling clay is an unwanted phenomenon, however as mentioned earlier (section 1.12) shales that swell during drilling may be good candidates for forming annular barriers later. It can be intuitive to assume that if a clay is swelling, the way of least resistance is usually radially inwards into the borehole. Moreover, even a small fluid invasion leads to a significant increase in pore pressure in the shale formation around the wellbore. The result is that the shale approaches the failure envelope as illustrated in the shear stress vs principal stress diagram in Figure 0.4, effectively making the shale weaker.

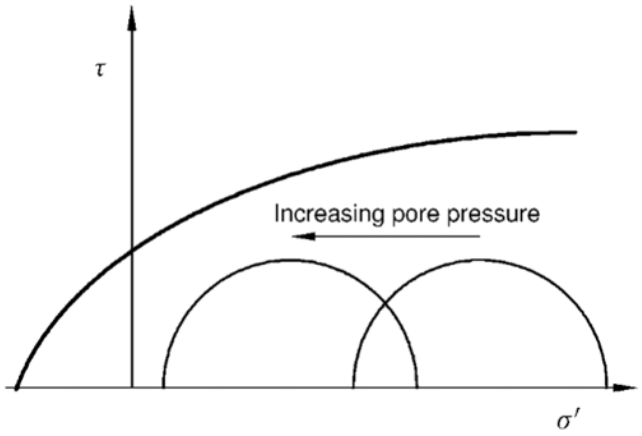

Figure 0.4: The effect of increasing pore pressure displayed in a shear stress (τ) vs principal stress (σ'). The line above the circles is the failure envelope (Fjaer, et al., 2008)

In short, clay swelling depends on (Darley & Gray, 2011):

• Clay structure

• Clay chemical composition

• Amount and type of exchangeable cations on clay particles

Crystalline Swelling

Crystalline swelling (also called surface hydration) occurs because water molecules are polar and therefore attracted to negative charge deficiencies which are often found on surfaces of clay. Water molecules replaces some of the cations and bind themselves to the external clay surface. In the case of expanding clays it can migrate between the unit layers and bind itself to the internal layers also. These clays has what is called expanding lattice. The internal water molecules causes an increase in the c-spacing, see Figure 0.5.

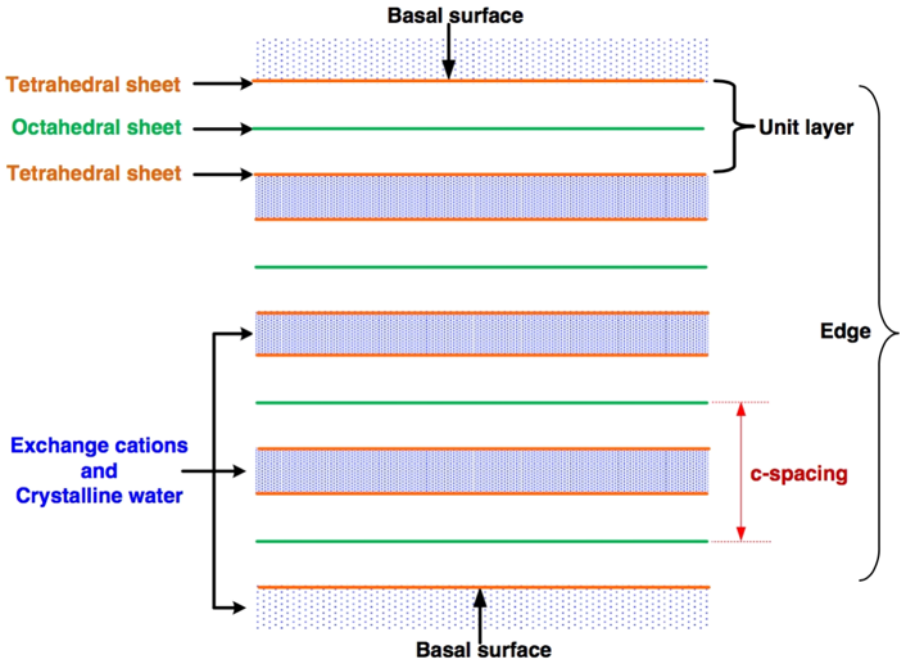

Figure 0.5: Expanding lattice of a smectite clay (montmorillonite) (Chen, 2016)

The type of cations on the basal surface is important because some cations are easier replaced than others. The type of cations also affect the attractive forces between the unit layers. Multivalent cations potentially associates with unit layers on both sides, generating an attractive force between the unit layers, whereas monovalent cations can simply bind itself to a single unit layer (Strand, 2001), see. Crystalline interlayer swelling of expansive clays are the range of 10-22 angstroms (Å) (c-spacing), beyond that it is considered osmotic swelling (Rao, et al., 2013).

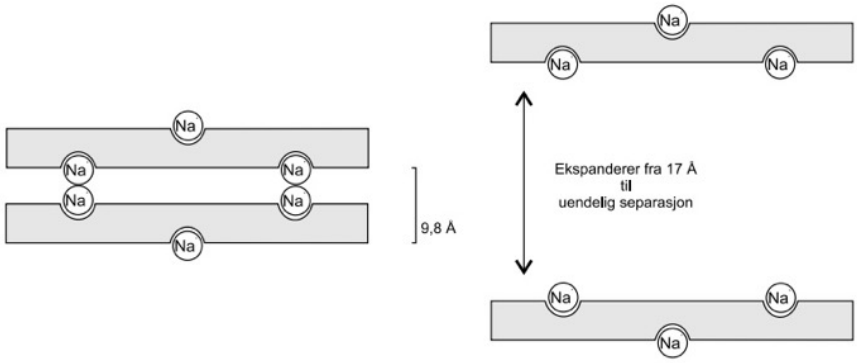

Figure 0.6: Expanding lattice with Sodium (Na^+) as cation (Strand, 2001)

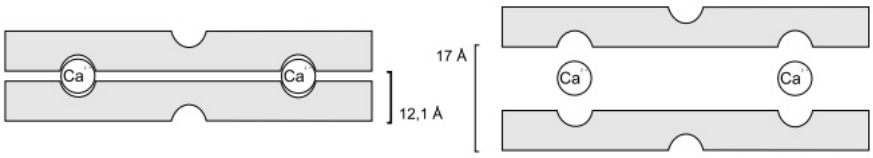

Figur 1.7

Figure 0.7: Expanding lattice with Calcium (Ca^{2+}) as cation (Strand, 2001)

Osmotic Swelling

Osmotic flow is the other main mechanism in clay swelling and can be explained as: migration of water molecules from one aqueous system to another through a semi permeable membrane, driven by the activity differences between the systems. A semi-permeable membrane allows water molecules to pass through, while restricting other molecules. In the case of swelling clays the activity difference is due to greater concentration of cations between the unit layers than in the aqueous solution/drilling fluid. Like mentioned this causes water molecules to migrate in between the layers and thereby increasing the c-spacing. Even though there actually is no perfect semi-permeable membrane involved in the case of clay hydration (some ions will move through the membrane) the mechanism is essentially osmotic, because it is governed by the difference in electrolyte concentration (Fjaer, et al., 2008) (Karpinski & Szkodo, 2015) . It is worth noting that osmotic swelling has a much larger potential to increase the bulk volume than crystalline swelling. However only a few clays, like smectite, expands in this manner.

Osmotic Pressure

Osmotic pressure is an important term when considering the degree of swelling. Given a higher ion concentration (lower activity) in the water between shale layers than in the drilling fluid, osmotic pressure can be described as the minimum overpressure required between shale layers to prevent inwards migration of water molecules from the wellbore fluid through the semi-permeable membrane. In other words, by how much must the "pore pressure" of the shale exceed the wellbore pressure in order to prevent flow of water molecules. An example is shown below in Figure 0.8, where water molecules flows from the low-salinity side of a u-shaped tube to the high-salinity side, through a semi-permeable membrane, in order to equalize the salt concentration. In the case of the u-shape tube this causes a hydrostatic pressure difference equal to the osmotic pressure when in equilibrium (Fakcharoenphol, et al., 2014).

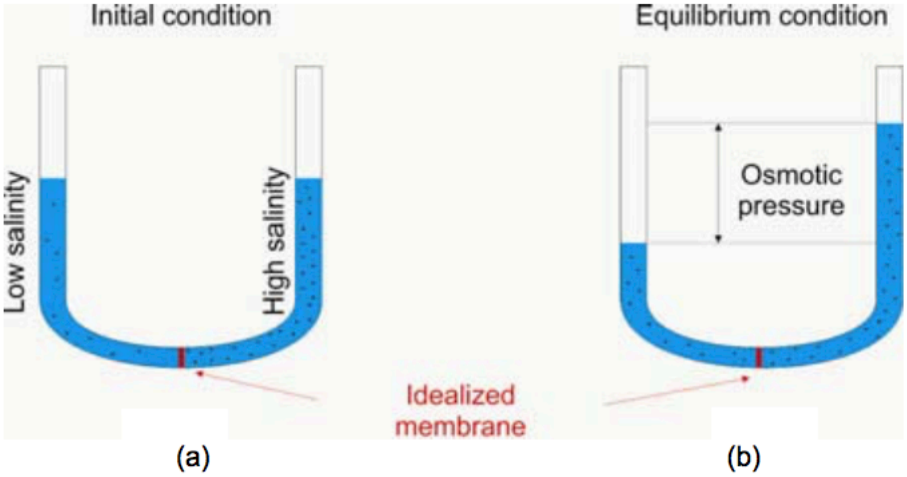

Figure 0.8: Illustration of osmotic pressure, where a shows the initial condition and b shows when equilibrium is reached (Fakcharoenphol, et al., 2014)

Osmotic pressure between drilling fluid and shale can be determined mathematically by the equation (Al-Bazali, et al., 2009):

$$P_\pi = -\alpha_m \frac{RT}{\overline{V_w}} ln\left(\frac{a_{w,shale}}{a_{w,mud}}\right) \quad \textbf{0.1}$$

Where P_π is the osmotic pressure, $\overline{V_w}$ is the molar volume of water and $a_{w,shale}$ and $a_{w,mud}$ are the water activities for shale and mud (drilling fluid) respectively. Note that water activity depends on a number of factors, but the general correlation with salts is that an increase in salt concentration reduces the water activity (flow goes from high to low activity).

Smectite

Smectite is a group of clays of particular interest in this report. A key characteristic of smectite is its expanding lattice. Smectite has a 2:1 structure consisting of two silicon (Si^{4+}) tetrahedral layers and an aluminum (Al^{3+}) octahedral layer in between, see Figure 0.3 and Figure 0.5. Atom substitutions are normal both within the tetrahedral and the octahedral sheet. The unit layers are bound together by van der waals forces, which in general are weak, making it easy for water to enter and increase the c-spacing (Fjaer, et al., 2008). Montmorillonite is the most famous member of the smectite group and isomorphic substitution is a normal occurrence within both the tetrahedral and the octahedral layer. More precisely in the form of Al^{3+} for $Si^{4+}$and Mg^{2+} for Al^{3+}respectively. Sodium montmorillonite can adsorb 0.5 grams of water per gram of dry clay by crystalline swelling. This results in a doubling of the volume. Furthermore, it can adsorb 10 grams of water per gram of dry clay by osmotic swelling, increasing the volume by 20 (Darley & Gray, 2011). This example clearly demonstrates the difference in magnitude between osmotic and crystalline swelling and also the how significant the swelling effect can be.

Stress vs strain values shows that smectite clays generally require more water in order to develop plastic properties, but as mentioned above it can adsorb large quantities of water before reaching the water liquid limit (a state where extremely small values of stress causes deformation). Furthermore, it takes less force to initiate yield and less force to yield continuously (Grim & Güven, 1978) (and sources therein: (Graham and Sullivan, 1939)). Shales containing smectite are susceptible to chemical activity and will creep due to consolidation and deterioration when exposed to different chemical conditions. This includes hydration and swelling triggered stress alterations (Wyllie, 1999). Making smectite rich shale formations excellent candidates for creep as indicated earlier in the report.